NEW SYSTEMS FOR QUANTUM NONLINEAR OPTICS

MARCO TOMMASO MANZONI

PhD Thesis

Thesis supervisor: Prof. Darrick E. Chang

ICFO-The Institute of Photonic Sciences
Universtitat Politècnica de Catalunya

July 2017 – Barcelona

Ai miei genitori

ABSTRACT

Photons travelling through free space do not interact with each other. This characteristic makes them perfect candidates to carry quantum information over long distances. On the other hand, processing the information they encode requires interaction mechanisms. In recent years, there have been growing efforts to realize strong, controlled interactions between photons, and to understand the underlying laws that describe the phenomena that can emerge, thus spawning the new field of "quantum nonlinear optics."

While bulk materials have extremely weak nonlinear coefficients, interactions between photons can be obtained by making them interact with individual atoms, which are intrinsically nonlinear objects, having the capability of absorbing only a single photon at a time. Realizing deterministic interactions between photons and atoms is one of the main challenges of quantum nonlinear optics. To circumvent the limitations due to the small optical cross-section of the atoms and the diffraction limit in free space, different strategies have been pursed, including the use of cavities (CQED), of atomic ensembles, and more recently of dielectric nanostructures able to confine light without defocusing, thus enabling the interaction with atoms trapped in the proximity of the structures. While for the CQED case powerful theoretical tools have been developed to treat the interactions of photons, in the case of atomic ensembles, either in free space or coupled to nanophotonic structures, there is a general lack of theoretical methods beyond the linear regime. This relative lack of understanding also implies that there could be rich new physical phenomena that have thus far not been identified. The overall goal of this thesis is to explore these themes in greater detail.

In Chapter 2 of this thesis we develop a new formalism to calculate the properties of quantum light when interfaced with atomic ensembles. The method consists of using a "spin model" that maps a quasi one-dimensional (1D) light propagation problem to the dynamics of an open 1D interacting spin system, where all of the photon correlations are obtained from those of the spins. The spin dynamics can be numerically solved using the toolbox of matrix product states (MPS), thus providing a technique to study strongly interacting photons in the true many-body limit. In the chapter, we show the power of this new approach first studying the propagation of a weak probe field in a Rydberg-EIT system, and then applying the MPS-based al-

gorithm to investigate light propagation under conditions of vacuum induced transparency, where the velocity of a pulse propagating through an ensemble becomes proportional to its photon number.

In Chapter 3 we investigate the possibility of creating exotic phases of matter using the recently realized photonic crystal waveguide (PCW)-atoms interface. In such a system the band gap modes of the PCW are used to mediate long-range interactions between atoms trapped nearby, making feasible the simulation of condensed matter models. We describe and investigate a realistic configuration in which these interactions couple strongly the motion of the atoms and their internal state ("spins"). This form of coupling raises the intriguing question of whether a novel "quantum crystal" can emerge, in which the spatial order of the atoms is stabilized by spin entanglement. Analysing in detail the Hamiltonian for different coupling strengths and external field magnitudes, we find a rich phase diagram of emergent orders, including spatially dimerized spin-entangled pairs, a fluid of composite particles comprised of joint spin-phonon excitations, phonon-induced Néel ordering, and a fractional magnetization plateau associated with trimer formation.

In Chapter 4 we investigate the possibility of implementing second-order nonlinear quantum optical processes with graphene nanostructures, as a more robust alternative to the use of atomic systems. Graphene is a two-dimensional material discovered in 2004 with peculiar optical and electronic properties. One interesting feature is that graphene can support surface plasmons (SP), collective charge-field oscillations that can be spatially confined several orders of magnitude tighter than free-space photons. We quantify the second-order nonlinear properties, showing that the tight confinement gives rise to extraordinary interaction strengths at the single-photon level. Finally, we predict that opportunely engineered arrays of graphene nanostructures can provide a second harmonic generation efficiency comparable with that of state-of-the-art nonlinear crystals, with the high Ohmic losses of graphene serving as the fundamental limitation for deterministic processes.

In Chapter 5 we investigate how cooperative emission in quantum memories realized with atomic arrays, *i.e.* spatially ordered atomic ensembles, affects their efficiency. After developing a compact formalism for quantifying the retrieval efficiency for an arbitrary detection mode, we study the case of a 2D atomic array where we find a significant improvement in the scaling with the number of atoms with respect to the case of a disordered three-dimensional ensemble. In particular we find

the impressive result that a memory realized with 16 atoms can have the same efficiency of an ensemble of optical depth larger that 100.

RESUMEN

Los fotones que viajan por el espacio libre no interactúan entre sí. Esta característica los hace perfectos candidatos para transportar la información cuántica a largas distancias. Por otro lado, el procesamiento de la información que codifican requiere mecanismos de interacción. En los últimos años se han realizado esfuerzos crecientes para realizar interacciones fuertes y controladas entre los fotones y para comprender las leyes subyacentes que describen los fenómenos que pueden surgir, generando así el nuevo campo de la “óptica cuántica no lineal".

Mientras que los materiales tridimensionales tienen coeficientes no lineales extremadamente débiles, se pueden obtener interacciones entre los fotones haciéndolos interactuar con átomos individuales, que son objetos intrínsecamente no lineales, teniendo la capacidad de absorber únicamente un solo fotón a la vez. La realización de interacciones determinísticas entre fotones y átomos es uno de los principales retos de la óptica cuántica no lineal. Para eludir las limitaciones debidas a la pequeña sección eficaz óptica de los átomos y el límite de difracción en el espacio libre, se han aplicado diferentes estrategias, entre ellas el uso de cavidades (CQED), de colectividades atómicas y, más recientemente, de nanoestructuras dieléctricas capaces de confinar la luz sin desenfocarse, permitiendo así la interacción con átomos atrapados en la proximidad de esas estructuras. Mientras que para el caso de la CQED se han desarrollado potentes herramientas teóricas para tratar las interacciones de los fotones, en el caso de colectividades atómicas, ya sea en el espacio libre o acopladas a estructuras nanofotónicas, hay una falta general de métodos teóricos más allá del régimen lineal. Esta relativa falta de comprensión también implica que podría haber nuevos fenómenos físicos interesantes que hasta ahora no se han identificado. El objetivo general de esta tesis es explorar estos temas con mayor detalle.

En el capítulo 2 de esta tesis desarrollamos un nuevo formalismo para calcular las propiedades de la luz cuántica cuando interactúa con sistemas atómicos. El método consiste en utilizar un “modelo de espines"que mapea un problema de propagación de luz cuasi unidimensional (1D) a la dinámica de un sistema abierto unidimensional de espines que interactúan entre sí, donde todas las correlaciones de fotones se obtienen a partir

de las de los espines. La dinámica de los espines se puede resolver numéricamente utilizando la caja de herramientas de los estados producto de matrices (MPS), proporcionando así una técnica para estudiar los fotones que interactúan fuertemente en el regimen de la física de muchos cuerpos. En el capítulo mostramos el poder de este nuevo enfoque estudiando primero la propagación de un campo débil en un sistema Rydberg-EIT, y luego aplicando el algoritmo basado en los MPS para investigar la propagación de luz bajo condiciones de transparencia inducida por vacío (VIT), donde la velocidad de un impulso que se propaga a través de una colectividad atómica se vuelve proporcional a su número de fotones.

En el capítulo 3 se investiga la posibilidad de crear fases exóticas de la materia utilizando la interfaz entre guía de ondas de cristales fotónicos (PCW) y átomos recientemente realizada experimentalmente. En un sistema de este tipo, los modos de la banda de frecuencias prohibidas de la PCW se utilizan para mediar las interacciones de largo alcance entre los átomos atrapados cerca de la guía de ondas, haciendo posible la simulación de modelos de materia condensada. Describimos e investigamos una configuración realista en la que estas interacciones unen fuertemente el movimiento de los átomos y su estado interno (“espín"). Esta forma de acoplamiento plantea la intrigante cuestión de si un nuevo cristal cuántico puede surgir, en el cual el orden espacial de los átomos se estabiliza por entrelazamiento de los espines. Analizando en detalle el Hamiltoniano para diferentes fuerzas de acoplamiento y magnitudes del campo externo, encontramos un rico diagrama de fases de órdenes emergentes, incluyendo pares espín-entrelazados espacialmente dimerizados, un fluido de partículas que corresponden a una excitación híbrida de espín y fonón, orden de Néel inducido por fonones, y un plateau de magnetización fraccionaria asociada a la formación de trímeros.

En el capítulo 4 se investiga la posibilidad de implementar procesos ópticos cuánticos no lineales de segundo orden con nano-estructuras de grafeno, como una alternativa más robusta al uso de sistemas atómicos. El grafeno es un material bidimensional descubierto en 2004 con peculiares propiedades ópticas y electrónicas. Una característica interesante es que el grafeno puede acomodar plasmones superficiales (SP), oscilaciones colectivas de campo de carga que pueden ser confinadas en regiones del espacio real varios órdenes de magnitud más pequeñas que en el caso de fotones en el vacío. Cuantificamos las propiedades no lineales de segundo orden, mostrando que el estrecho confinamiento da lugar a extraordinarias fuerzas de interacción a nivel de un solo fotón. Finalmente, se predice que

un diseño apropiado de las nano-estructuras del grafeno permitiría generar el segundo armónico con una eficiencia comparable a la de los cristales no lineales de última generación, siendo las grandes pérdidas óhmicas del grafeno la única limitación fundamental para obtener procesos determinísticos.

En el capítulo 5, investigamos cómo la emisión cooperativa en memorias cuánticas realizadas con reticulos atómicos, es decir, colectividades espacialmente ordenadas, afecta su eficiencia. Después de desarrollar un formalismo compacto para cuantificar la eficiencia de recuperación del fotón en un modo de detección arbitrario, estudiamos el caso de un reticulo atómico 2D donde encontramos una mejora significativa en la manera en la cual la eficiencia depende del número de átomos con respecto al caso de un gas atómico desordenado. En particular encontramos el impresionante resultado de que una memoria realizada con 16 átomos puede tener la misma eficiencia que un gas cuántico atómico de profundidad óptica mayor que 100.

PUBLICATIONS

1. Manzoni, M. T., Silveiro, I., García de Abajo, F. J. & Chang, D. E. Second-order quantum nonlinear optical processes in single graphene nanostructures and arrays, *New J. Phys.* **17**, 083031 (2015).

2. Caneva, T., Manzoni, M. T., Shi, T., Douglas, J. S., Cirac, J. I. & Chang, D. E. Quantum dynamics of propagating photons with strong interactions: a generalized input-output formalism, *New J. Phys.* **17**, 113001 (2015).

3. Manzoni, M. T., Mathey, L. & Chang, D. E. Designing exotic many-body states of atomic spin and motion in photonic crystals, *Nat. Commun.* **8**, 14696 (2017).

4. Manzoni, M. T., Chang, D. E. & Douglas, J. S. Simulating quantum light propagation through atomic ensembles using matrix product states, preprint at arXiv:1702.05954 (2017).

The results of the second and of the fourth publication are included in Chapter 2, those of the third and of the first publication are included in Chapter 3 and 4, respectively. Chapter 5 contains unpublished work.

ACKNOWLEDGMENTS

First and foremost, I would like to thank my thesis advisor and mentor Prof. Darrick Chang. Thanks for your constant guidance and support in this four years-long adventure, for having your door always opened to students and for showing me what it means dedication to science. It has been a great honour to be your first student.

In two of the research projects I have pursued during the PhD I have had the pleasure to collaborate with Prof. Ludwig Mathey, who hosted me for a month at the University of Hamburg, and with Prof. F. Javier García de Abajo. I would like to thank them both for sharing their knowledge of unfamiliar physics fields with me. Thanks also to Ivan Silveiro, my first collaborator at ICFO. I would like to thank Prof. Jeff Kimble, for motivating me in many occasions, for the several discussions and for hosting me at Caltech three times.

During the PhD I have received fundamental support from my group colleagues. Above all, I would like to thank James, who has been a constant reference since the day of my interview. Too many times I have asked him for help and assistance during these years. His contributions to this thesis go far beyond the project in which we formally collaborate. Thanks to Tommaso, for having taught me much during the first years of the PhD. Thanks to Ana, mate of many oversea travels, for providing fun and support. Thanks to Andreas, for being a not-so-bad office mate (despite his attempts to kill me with the AC), and to Mariona, always kind and ready to help. Thanks to all the others colleagues, Marinko, Christine, Lukas, Hessam, Marcos, David, Loïc, Stefano, with whom I have enjoyed many discussions and lunches, I have learnt from all of you.

I would like to thank the “la Caixa" foundation for its generous support through the four-years scholarship “la Caixa-Severo Ochoa" I benefit from. Fundamental support to the group research has come from the late Dr. Pere Mir i Puig and from the European Union.

My PhD studies would have not been the same without the presence of many ICFOnians colleagues and friends. Thanks to Ale, for being a great friend and for his contagious never-ending happiness, to Emanuele (and his bibliometric obsessions), to Sergio, Nicola el guapo and Nicola el non guapo, Jil, Alex, Alessio, Marco, Ivan, Martina and many others.

Thanks to all the friends with whom I have shared moments, even just a summer, during these wonderful time in Barcelona:

among them Federica, Mario, Alessio, Chris, Verdiana, Yulia, Michaela, Giulia, Gianmarco, etc. Thanks to Michela for being a great and supportive flatmate and friend, to Dani and Maria. Thanks to Pradeep, for being my farest friend and a great inspiration to me. Grazie ai miei amici brianzoli Bova, Capra, Skilly, Alice, Mastro, Elisa, Ottavia, Jack, Chiara & Cerry, per farmi sentire a casa ogni volta che torno.

Grazie alla mia famiglia, ai miei genitori, a cui devo tutto e a cui è dedicata questa tesi, a mia nonna, che ha sofferto più di tutti la mia lontananza, e a mio fratello (che sicuramente ne ha sofferto meno). Grazie per il vostro sostegno e la vostra pazienza.

Last but not least, gracias a Alicia por todo el amor y el cariño, gracias por soportarme y animarme siempre con tu entusiamo durante estos años. Que empieze pronto una nueva aventura juntos.

CONTENTS

Part I

INTRODUCTION

1 INTRODUCTION

1.1 QUANTUM NONLINEAR OPTICS (QNLO)

The optical properties of vacuum and most materials are intensity-independent, *i.e.* not sensitive to the number of photons which are propagating through them. Light propagation in these media is represented schematically in Fig. 1.1a, where photons behave as non interacting particles. This is the realm of linear optics, where the dynamics of light is simply described by a complex number, called the index of refraction of the medium, which contains all the information about the phase modification (dispersion) and the loss of energy (absorption) of the light during propagation [1]. In terms of applications, if on one hand their non interacting behaviour makes photons perfect carriers of information over long distances, on the other hand the need of processing the information encoded in light makes it desirable to have a mechanism whereby photons can interact.

Shortly after the invention of the laser, a source of coherent high-intensity light, it was realized that at large light intensities some materials also present weak intensity-dependent optical properties [2]. This important discovery signalled the birth of classical nonlinear optics. Since then, one of the major goals of this field has been to create the conditions for which optical nonlinearities could be observed at progressively lower intensity, ideally down to the limiting case of quantum nonlinear optics (QNLO) [3], where few photons, or even a single one, can change the optical properties of a medium, as represented in Fig. 1.1b. Reaching this ideal limit would open the door to the realization of both classical devices, such as optical transistors and switches, operating at their ultimate limit, and devices to generate and manipulate non-classical states of light, such as for quantum information processing [4].

However, conventional bulk materials have nonlinear coefficients which are too small, orders of magnitude far away from the QNLO regime [3]. The fundamental constituent of matter, the individual atom, on the contrary is an extremely nonlinear object, as a consequence of the anharmonicity of the atomic spectrum resulting from the Coulomb potential. For this reason, when light is nearly monochromatic and close to resonance with a given atomic transition, the atom is often described as a

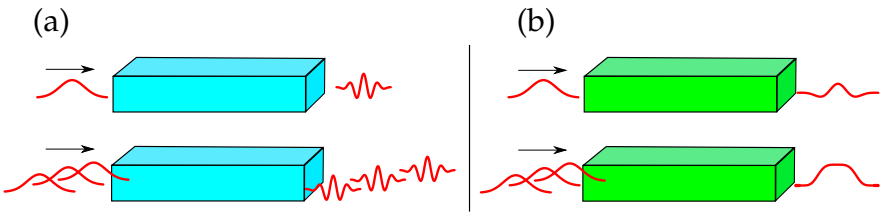

Figure 1.1: Linear optics vs. quantum nonlinear optics (QNLO). (a) When propagating through a linear medium photons experience dispersion and absorption, but these effects are independent of the number of photons propagating inside the medium. (b) On the contrary, in a nonlinear medium light propagation is affected by the number of photons entering the medium.

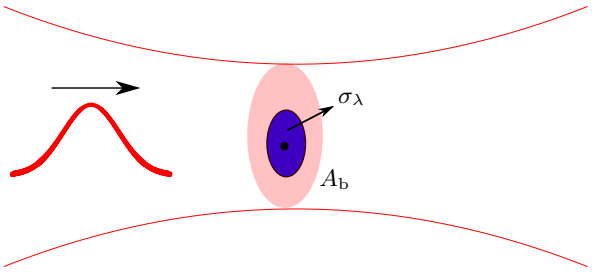

Figure 1.2: Schematic representation of a Gaussian beam focused onto a single atom. The probability of interacting with the atom for a (resonant) photon in the beam mode is given by $P \sim \sigma_\lambda / A_b$, where $\sigma_\lambda \sim \lambda^2$ is the atomic optical cross section and A_b is the beam cross-sectional area at the atomic position.

two-level system, an object which is thus capable of absorbing and emitting only one photon at time.

At the same time, the daily-life experience of the transparency of gaseous media such as air indicates that light interacts only very weakly with atoms. If we imagine the atom as a solid disk, it would have an area $\sigma_\lambda \sim \lambda^2$ as far as how it interacts with light (the optical cross section), where λ is the resonant wavelength squared. The probability P to interact with a resonant photon in a laser beam is then equal to σ_λ / A_b (see Fig. 1.2), where A_b is the cross-sectional area of the beam [5]. σ_λ is many orders of magnitude larger than the physical dimension of the atom but nevertheless, because of the diffraction limit which prevents focusing of light down to areas smaller than λ^2, achieving $P \sim 1$ is extremely challenging. Up to now, experimental efforts to couple individual emitters to strongly focused beams have led to record values of $P \sim 0.05$ for neutral atoms [6, 7], ~ 0.01 for ions [8], and ~ 0.1 for molecules confined in a surface [9].

Different and more sophisticated schemes have been explored to increase the interaction probability P. In the following we briefly review the main approaches: cavity quantum electrodynamics and atomic ensembles. The basic concepts underlying these approaches will serve as a point of comparison later, when we introduce new paradigms for atom-light interactions and theoretical techniques to solve for the dynamics of strongly interacting photons.

1.1.1 *Cavity quantum electrodynamics (CQED)*

One way to increase P consists of making the photon pass through the atom more than once. In this way naively P gets multiplied by the number of passages N (when $NP \ll 1$). The strategy adopted to achieve these multiple passages is to trap the atom between two mirrors separated by a certain distance L, a system known as an optical cavity (see Fig. 1.3a) [10, 11]. In such a system, heuristically the photon bounces back and forth between the mirrors until it exits the cavity by tunnelling through one of the mirrors, or being absorbed or scattered by mirror imperfections. Intuitively, N is given by the ratio between the average time the photon spends in the cavity, equal to $1/\kappa$, with κ being the decay rate of the cavity mode, and the time spent to go from a mirror to the another one, equal to $L/c = 2\pi L/(\lambda\omega_c)$, with ω_c being the cavity frequency. The ratio ω_c/κ is called the quality factor of the cavity in the jargon of cavity quantum electrodynamics (CQED), and is denoted by Q.

We then have that the probability of interaction in the CQED approach is $P \sim Q\lambda^3/V_c \equiv C$, where $V_c = A_c L$ is the cavity effective mode volume. The factor C is called "cooperativity" and is a figure of merit for how well the atom and photons in the cavity mode interact. While the meaning of cooperativity as probability holds strictly only for $P \lesssim 1$, the significance of the cooperativity goes beyond that limit, as we will see later in the discussion of CQED systems.

By quantizing the cavity mode one can obtain a Hamiltonian for the atom-cavity system, which is known as the Jaynes-Cummings (JC) model [12]:

$$H_{JC} = \hbar\delta_{JC}\sigma^{ee} + \hbar g_{JC}(\mathbf{r})(\sigma^{eg}a + \sigma^{ge}a^\dagger), \tag{1.1}$$

in a frame rotating at the cavity frequency. Here $\delta_{JC} = \omega_{eg} - \omega_c$ is the atomic resonance-cavity resonance detuning, $g_{JC}(\mathbf{r})$ is the position-dependent atom-cavity field coupling ($g_{JC}(\mathbf{r}) \approx g_0 \cos kx$ along the cavity axis, reflecting the standing wave structure), $\sigma^{ge} = |g\rangle\langle e|$ is the atomic lowering operator and a is the annihilation operator of the cavity mode. The first term in

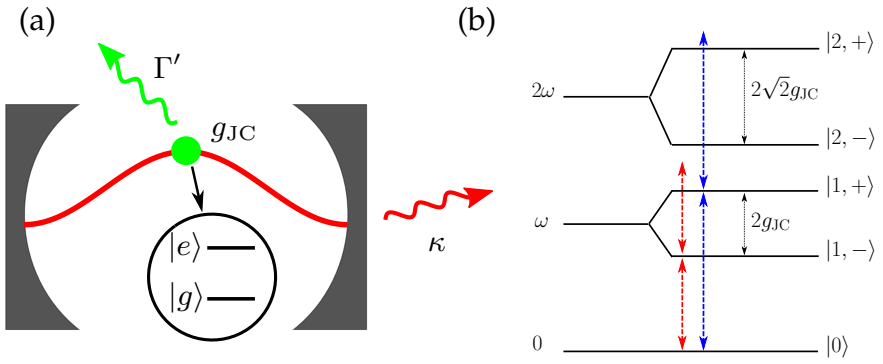

Figure 1.3: (a) Schematic representation of a cavity QED system. A two-level atom is coupled to a mode of the cavity with coupling strength g_{JC}. The atom can also decay outside of the cavity at a rate Γ'. κ is the cavity decay rate, due to imperfect mirrors. (b) Spectrum of the Jaynes-Cummings model for zero, one and two excitations. Red and blue arrows are represented to show the anharmonicity of the spectrum. In particular, the frequency needed to produce a resonant transition from zero to either one of the single-excitation eigenstates is then non-resonant when going from the single- to two-excitation manifold.

the Hamiltonian corresponds to the detuning of the atomic transition from the cavity frequency, while the second term, arising from the dipole interaction of the atom with the cavity mode, describes the coherent exchange of excitations from the atomic excited state to the cavity mode and vice versa. The coupling strength $g_{JC} \sim \wp\sqrt{\omega_c/\epsilon_0\hbar V_{eff}}$ is proportional to the atom dipole matrix element $\wp = \langle e|\,\mathbf{d}\,|g\rangle$ and inversely proportional to the square root of the cavity effective volume.

The total number of excitations $\hat{N} = \sigma^{ee} + a^\dagger a$ is a conserved quantity, since it commutes with Hamiltonian (1.1), which can thus be block-diagonalized. Each block, denoted by the number of total excitations n, has dimension two and is spanned by the basis $\{|g,n\rangle, |e,n-1\rangle\}$, a notation indicating the atomic state and the number of photons in the cavity mode. The eigenvectors $|n,\pm\rangle$ of each block are a superposition of these two states and have eigenenergies $E_{n,\pm} = \hbar(n\omega_c + \delta_{JC} \pm (1/2)\sqrt{\delta_{JC}^2 + 4g_{JC}^2 n})$. The lowest states of this spectrum are shown in Fig. 1.3b (for $\delta_{JC} = 0$). One can immediately notice that the dependence on $\sqrt{n}$ of the separation between each pair of eigenvalues makes the spectrum highly nonlinear. This fact is represented by the blue and red arrows in the figure, which show that when a photon is resonant with an eigenstate of the system, a second photon with the same frequency in general is not. The transmission properties of a CQED system are thus expected to be pho-

ton number-dependent [13], as for the ideal nonlinear medium of Fig. 1.1.

In the introduction and short discussion of the JC model we have ignored the fact that the system is in general not closed, since excitations can be lost through the non-perfect reflectance of the mirrors and through atomic spontaneous emission into free space (with this latter decay characterized by the decay rate Γ'). To account properly for these dissipative mechanisms one has to adopt the open system formalism, where the state of the system is described by a density matrix, whose dynamics satisfies a master equation [14]. One can account for the losses by introducing imaginary terms in the Hamiltonian. In this way the spectrum becomes complex, and the energy levels (the lines in Fig. 1.3b) acquire a width equal to the imaginary part of their eigenvalues. The practical consequence of this fact is that the nonlinearity of the spectrum will only have significant observable consequences if the magnitude of that nonlinearity exceeds the linewidths of the involved states.

The JC model is a powerful tool to describe the dynamics of the atom-cavity system at a given number of excitations, but not sufficient to describe how the system connects with the outside world, and the quantum properties of the light exiting the cavity. The necessary bridge between the internal and the external dynamics is provided by a tool of quantum optics called the "input-output formalism" [15]. Within this formalism the external light is modelled as a one-dimensional continuum of modes, described by the Hamiltonian $H_{ext} = \sum_k \omega_k b_k^\dagger b_k$, with $\omega_k = c|k|$. The interaction between these external modes and the cavity mode is assumed to be linear, and described by $H_{e-c} = \eta \sum_k (a^\dagger b_k + H.c.)$, with the coupling constant assumed to be frequency-independent (at least over the range of frequencies of interest).

From $H = H_{JC} + H_{ext} + H_{e-c}$ one can then obtain the equations of motion of the external and cavity mode operators. The equations for the external field can be formally integrated in time, yielding

$$b_k(t) = e^{-i\omega_k(t-t_i)} b_k(t_i) + \eta \int_{t_i}^{t} dt'\, e^{-i\omega_k(t-t')} a(t'), \qquad (1.2)$$

where the first term on the r.h.s. is the initial boundary condition at an initial time t_i, physically corresponding to the free propagating field before the interaction with the cavity. The second term consists instead of the field emitted by the cavity mode into the external continuum. An equivalent formal integration can be done in terms of the boundary condition at a final time t_f. In this case the first term on the r.h.s. will corre-

spond to the free propagating field after the interaction with the cavity. A natural step is then to define an input mode operator

$$b_{in} = \frac{1}{\sqrt{2\pi}} \int dk e^{-i\omega_k(t-t_i)} b_k(t_i), \tag{1.3}$$

and, in a similar way, but involving $b_k(t_f)$, an output mode operator. Finally, if $1/\omega_k$ is much shorter than the time over which the cavity mode operator $a(t)$ changes significantly, one can perform the so-called *Markov approximation* and replace $a(t')$ with $a(t)$ in Eq. (1.2). Combining these ingredients one gets a fundamental relation between the input and output modes:

$$b_{out}(t) = b_{in}(t) + \sqrt{\kappa} a(t), \tag{1.4}$$

with $\kappa = 2\pi\eta^2$. Eq. (1.4) is called the "input-output" equation of the system, and shows that the quantum field leaving the cavity is a sum of that which enters, and part of the cavity field leaking out. This equation enables the properties of the field exiting the system to be calculated, given knowledge of the input field and system dynamics. Its importance cannot be underestimated; in fact equations of this form will be recurrent in this thesis.

Applying the same mathematical manipulations to the equation of motion of the cavity mode operator, one finds that this equation assumes the form of an Heisenberg-Langevin equation:

$$\dot{a} = \frac{i}{\hbar}[H_{JC}, a] - \frac{\kappa}{2} a - \sqrt{\kappa} b_{in}(t), \tag{1.5}$$

which is the equation of motion of an effective Hamiltonian containing only the system degrees of freedom and the input mode:

$$H_{JC,open} = H_{JC} - i\frac{\kappa}{2} a^\dagger a - i\sqrt{\kappa}(a^\dagger b_{in}(t) + H.c). \tag{1.6}$$

This result is extremely important since it shows that we can couple a CQED system with a continuum of external modes without having to deal with these modes explicitly. It is indeed enough to add an imaginary term to the energy of the cavity photons accounting for the decay of cavity excitations, as mentioned above, and to drive the cavity mode with a single input mode.

After having presented all the tools required to study the optics of a CQED system, we consider briefly the case in which more than one atom is trapped inside the cavity, a situation which is interesting because the cavity mode can facilitate the exchange of excitations between the atoms, thus realizing an effective atom-atom interaction. A particularly relevant case is

when the detuning $|\delta_{JC}| \gg g_{JC}$. In this regime one of the single-excitation eigenstates consists of an excited atom weakly dressed by a cavity photon. For multiple atoms this virtual photon generates an effective exchange interaction between the atoms of the form [16]

$$H_{int} = \frac{\hbar}{\delta_{JC}} \sum_{jl} g_{JC}(\mathbf{r}_j) g_{JC}(\mathbf{r}_l) \sigma_j^{eg} \sigma_l^{ge}. \tag{1.7}$$

This effective Hamiltonian, which can be obtained rigorously by integrating out the photonic degrees of freedom, describes the process whereby one atom loses an excitation (σ_j^{ge}) and another gains it (σ_l^{eg}), mediated by a virtual photon. It is worth to note that, since the virtual photon occupies all the cavity, the coupling constant for a given pair of atoms depends only on the positions of the atoms with respect to the cavity mode, and not on the relative positions. In other words we can say that this cavity-mediated effective interaction is infinite-range.

If one considers Eq. (1.7) with just two atoms and equal coupling, it is possible to calculate the error probability in the exchange of an excitation, *i.e.* the probability that the photon gets lost during the transfer process instead of being absorbed by the second atom. The exchange time is simply given by $\tau \sim \delta_{JC}/g_{JC}^2$. The loss rate is given by the sum of the spontaneous emission into free space and of the cavity decay (weighted by the populations in each degree of freedom), and is equal to $\Gamma_{tot} \approx \Gamma' + \kappa(\delta_{JC}/g_{JC})^2$, where $(\delta_{JC}/g_{JC})^2$ is the cavity mode occupation. The total error probability is thus $\mathcal{E} = \tau\Gamma_{tot}$. It can be minimized with respect to the detuning obtaining a lower bound for the error equal to $\mathcal{E}_{min} = 1/\sqrt{C}$, where C is the single atom cooperativity introduced previously. We thus see again that the cooperativity is an important figure of merit in CQED.

1.1.2 *Atomic ensembles*

A second way to enhance the atom-light interaction consists of using an atomic ensemble [17], as schematically represented in Fig. 1.4a. The obvious effect is to multiply the single-atom interaction probability $P \sim \sigma_\lambda/A_b$ by a factor proportional to the number of atoms in the ensemble N_a. Here the figure of merit is thus given by the factor $OD = N_a\sigma_\lambda/A_b$, called the "optical depth" of the system [17]. This quantity enters, for instance, in Beer's law, which describes the exponential attenuation of the intensity of a beam when crossing a gas of two-level atoms, *i.e.* $I = I_0 \exp(-OD)$.

Historically, the propagation of a field through an atomic ensemble that it interacts with is modelled using the Maxwell-Bloch equations [18, 19]. First, the propagation equation for the quantum electric field E, taken to be one-dimensional for simplicity, is coupled to a smoothed-out atomic polarization density (*i.e.* the granular nature of atoms or density fluctuations are ignored),

$$(\partial_t + c\partial_z)E = igN_z P_{ge} \tag{1.8}$$

where $P_{ge} = 1/N_z \sum_i \sigma_i^{ge}$ are atomic operators averaged over all the atoms with the same z coordinate (the dependence on z and t of E and P is implied), and g is the field-atom coupling strength.

Here, we have assumed two-level atoms, but the equations can be suitably generalized to multi-level structure. The atomic polarization density, on the other hand, is driven by the field, and obeys an optical Bloch equation

$$\partial_t P_{ge} = -i(\Delta - i\Gamma/2)P_{ge} - igE(P_{ee} - P_{gg}) + F, \tag{1.9}$$

where $\Delta = \omega_{eg} - \omega_p$ is the detuning of the probe field, Γ is the free-space decay rate of the atoms and F is a noise term.

In general, the equations above represent an open interacting quantum field theory, which is in general unknown how to solve for exactly. The complexity can be reduced by noting that typically, the level of nonlinearities in atomic ensembles is quite weak, since the number of atoms is typically larger than the number of photons absorbed. Thus, one common approximation is to treat the electric field at a mean-field level. For weak light intensities, the linearized Maxwell-Bloch equations can be solved, obtaining the above mentioned Beer's law. For larger intensities, this gives rise to a classical nonlinear propagation problem. This limit, for example, can be used to describe the phenomenon of self-induced transparency [19]. Alternatively, one can linearize the atomic system, such that the resulting joint quantum state of matter and light is Gaussian [17]. This regime itself covers important applications such as quantum memories for light [20–23] or spin squeezing [24].

In recent years, a remarkable approach has been developed that enables single-photon-level nonlinearities in atomic ensembles. Qualitatively, the idea is that with large optical depth, an incident photon can be efficiently absorbed and converted to an atomic excited state. In turn, if these atomic excited states can be made to interact strongly, such as in Rydberg states, this atomic interaction effectively manifests itself as a photon-photon interaction as photons exit the medium. Here we review briefly the most successful approach in this direction, the EIT-Rydberg scheme [25–28].

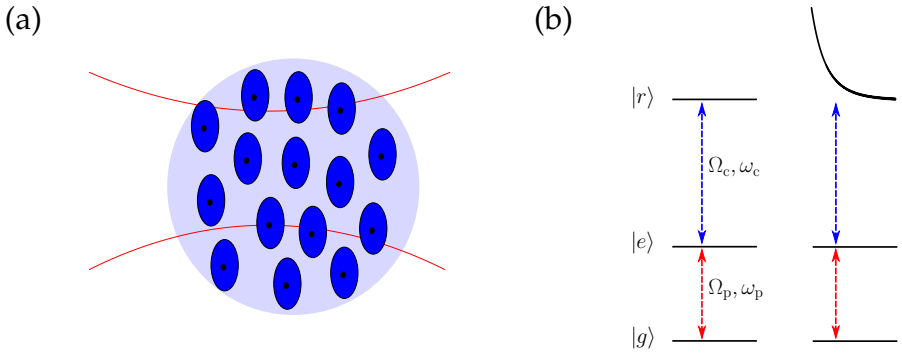

Figure 1.4: (a) Schematic representation of an atomic ensemble interacting with a laser beam. (b) Representation of the Rydberg-EIT scheme. The red and blue arrow are the probe and control field, here taken to be perfectly resonant with the $|g\rangle - |e\rangle$ and $|e\rangle - |r\rangle$ transitions, respectively. On the right, the energy of the Rydberg state is modified by the dipole-dipole interaction, with consequent destruction of the EIT resonant condition.

The key ideas of this scheme are represented in Fig. 1.4. First of all, three-level atoms are used, with the probe field resonant with the transition $|g\rangle - |e\rangle$, and the transition $|e\rangle - |r\rangle$ driven by the classical control field Ω_c. In this way, when the sum of the probe and control frequency is resonant with ω_{rg}, the "electromagnetically induced transparency" (EIT) scheme is realized [29]. In EIT (a topic which will be treated in greater detail in Chapter 2) the linear response of the atomic ensemble changes from absorptive to dispersive as a consequence of interference between the probe and the control field, which suppresses the excited state $|e\rangle$ population, while mapping the probe photons into $|r\rangle$ state excitations that are assumed to be long-lived.

The second ingredient of the scheme, as anticipated, is that $|r\rangle$ is a Rydberg state, *i.e.* a state with a high principal number $n \approx 100$ [28], and thus very large lifetime and dipole moment. Such a large dipole moment results in strong van der Waals interactions when two atoms are both in a Rydberg state. In particular, once a single photon is converted into an atomic excited state $|r\rangle$ via EIT, this atom shifts the energy of Rydberg levels of nearby atoms by a large amount (see Fig. 1.4b). This destroys the two-photon resonance condition for EIT within a certain distance r_b, called the Rydberg radius, and leads to strong multi-photon absorption. It has been observed that this nonlinearity is strong enough to preclude the existence of two overlapping photons upon exit from the medium, resulting in a significant non-classical "anti-bunching" signature [30–32]. Such schemes can also be modified to produce dispersive nonlinearities [33].

The Maxwell-Bloch equations can be easily modified to describe three-level atoms. However, the fact that these experiments can produce strongly non-classical states of light clearly indicates that the typical approximations made to solve the Maxwell-Bloch equations are no longer applicable. Solving the Maxwell-Bloch equations with this added complexity is a highly non trivial task but of fundamental importance to understand whether interesting many-body states of light, which can have applications in quantum computing and metrology, can be generated by atomic ensembles. This problem will be dealt with in Chapter 2 of the thesis.

1.2 ATOMS AND NANOPHOTONICS

In the previous section we have introduced the concept of quantum nonlinear optics, observing that while an individual atom looks like a highly nonlinear system, making single photons interact with them is in general very challenging. We have then reviewed the two main approaches adopted to increase the atom-light interaction probability: CQED and atomic ensembles. These schemes have the common characteristic to be free space approaches, in the sense that the atoms, cooled and trapped, interact with certain free space modes of the electromagnetic field.

In this section we describe the advantages that can be obtained by confining instead the light in dielectric structures, giving an overview of such systems. We will see that atoms coupled to these nanophotonic structures do not obviously fall into the previous categories of cavity QED or atomic ensembles. An interesting question is how to theoretically model such systems, and what similar or different paradigms for light-matter interactions are possible. This question will be addressed further in later sections of the thesis.

We have seen in Sec. 1.1 that the strong focusing of laser beams permits one to reach atom-photon interaction probabilities up to 10%. Such high values cannot be extended to atomic ensembles, because strongly focused beams diverge quickly along the propagation direction. The optical depth per atom in atomic ensemble is indeed much lower, with typical ensembles containing $10^5 - 10^7$ atoms and having an optical depth smaller than 100 [17]. A way to circumvent the problem of defocusing and thus to keep constant the single atom-single photon interaction probability over a long propagation distance is to confine light in guided modes of nanophotonic structures, such as nanofibers and photonic crystal waveguides.

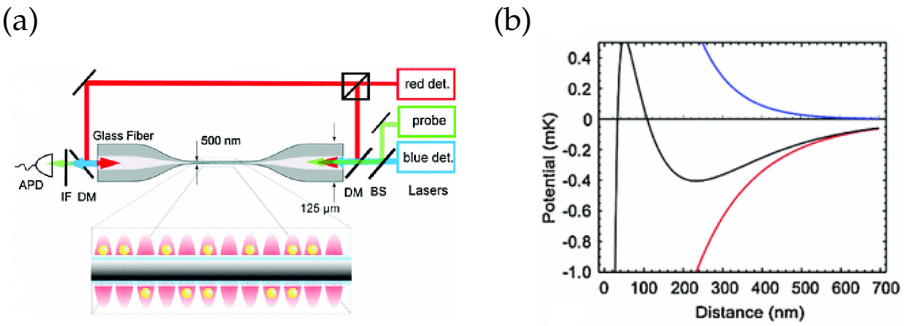

Figure 1.5: (a) Schematic representation of experimental setup of Ref. [34]. The inset shows the nanofiber with atoms periodically trapped in its proximity. The diameter of the fiber is 500 nm, while the atoms are trapped at approximately 200 nm from the surface. Red- and blue-detuned optical fields guided by the nanofiber create the potentials plotted in (b), where the black line is the overall potential felt by the atoms in the transversal direction. The red-detuned field is sent from both directions in order to create a longitudinal periodic potential.

1.2.1 *Optical nanofibers*

The simplest dielectric structure able to confine propagating light in one dimension is the optical nanofiber. It typically consists of a high refractive index core surrounded by a lower index cladding, or vacuum in our case of interest. In the ray optics picture one can say that total internal reflection prevents the light to leak out of the fiber, confining its propagation in the longitudinal direction. More generally, a fiber mode must satisfy the relation $(\omega/c)^2 = k_{\parallel}^2 + k_{\perp}^2$, where $k_{\parallel}$ is the component of wavevector parallel to the structure, $k_{\perp}^2$ the component orthogonal to it, and ω is the mode frequency. Since the index of refraction of the fiber is larger than 1, one can have $k_{\parallel}^2 > (\omega/c)^2$. Then, to satisfy the previous relation, the corresponding value of $k_{\perp}$ is forced to be imaginary. Physically this means that the field is evanescent in the transversal direction, *i.e.* it decays exponentially with distance from the surface of the fiber, while propagating along the fiber. For this reason such modes are called “guided modes". For a sufficiently small radius, the fiber becomes single-mode, in that only a single transverse mode shape is allowed at a given frequency. The evanescent tail of a guided mode can extend for some wavelengths out of the core, enabling an interaction between guided light and atoms located nearby the nanofiber.

The first experiments with atoms and fibers were realized with atomic clouds surrounding the fiber [35]. Later on, it was

realized that a trapping potential in the transversal direction could be realized by sending in the fiber a combination of red- and blue-detuned fields with respect to the atomic resonant frequency [34] (see Fig. 1.5a). Indeed, the dipole force associated with the red-detuned light, as well as van der Waals forces, attract the atoms to the fiber surface; vice versa the blue-detuned light pushes the atoms away from the fiber. Because of the different transverse extent of the two fields, the combination of the two potentials creates a minimum at a fixed distance from the surface (see Fig. 1.5b). A counter-propagating red-detuned field is also used to create a standing wave which serves as a trapping potential in the longitudinal direction.

In such waveguide-atom systems the interaction probability of a single atom with a photon propagating in the guided mode is related to the ratio between the decay rate into the fiber Γ_{1D} and the decay rate in free space Γ', as $P \approx 2\Gamma_{1D}/\Gamma'$. This formula is strictly valid only for $\Gamma_{1D} \ll \Gamma'$, a condition that is always satisfied for the case of optical nanofibers coupled to real atoms, but that can be violated in other systems. Initial proof-of-principle experiments have reported optical depths per atom of 0.0064 [34] and 0.08 [36] with about 4000 and 800 atoms respectively.

1.2.2 *Photonic crystal waveguides (PCW)*

Nanophotonic devices are not useful only for confining light and guiding it, but also because they can modify its dispersion relation. In the case of the nanofiber described above, the dispersion relation is approximately linear over very large bandwidths, *i.e.* $\omega(k) \approx (c/n_f)k$ with n_f being the index of refraction of the fiber core. However, a periodic modulation of the dielectric properties of the fiber can change qualitatively the form of the dispersion relation. If a single defect in the fiber simply generates back-scattering and emission out of the guided mode, a periodic array of defects open gaps in the dispersion relation with the formation of photonic bands, realizing what is called a photonic crystal waveguide (PCW) [37] (see Fig. 1.6). The origin of the band gaps lies in the multiple scattering due to the modulation, which creates destructive interference at certain frequencies and thus prevents light propagation. The physics is analogous to that of electrons in metals, where the periodic potential due to the ions produces energy bands. Similarly, in a PCW light is subjected to a periodic potential and thus Bloch's theorem applies for photonic modes. The theorem states that normal modes must have electric fields of the form $E_{n,k}(x) = e^{ikx}u_{n,k}(x)$, where u is a periodic function with a pe-

(a)

(b)

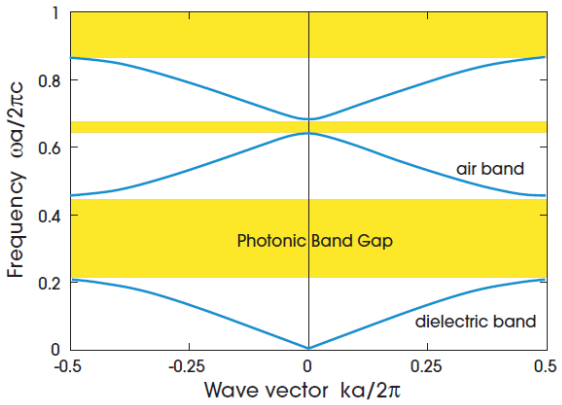

Figure 1.6: (a) Cartoon picture of a PCW with holes inserted periodically in a dielectric waveguide. (b) Typical band structure, of guided mode frequency ω versus Bloch wavevector k (both rescaled by the lattice constant a), in a 1D PCW. In yellow are represented frequency regions corresponding to band gaps [37]. "Dielectric" and "air" bands refer to where the electric field intensity is concentrated for each of these modes.

riodicity given by the lattice constant of the structure, and k is the Bloch momentum along the direction of propagation x.

As one might expect, the most interesting effects for light propagating in a PCW are realized in proximity of the band edges, where the PCW dispersion relation differs most from the fiber one. At the band edges indeed the slope of the dispersion relation decreases to zero. This corresponds to a great reduction of the group velocity of light $v_g(k) = \partial\omega/\partial k$ [39]. This slowdown of the group velocity increases the time of interaction of the atom and photon by a factor of $n_g = c/v_g$, so that the atom-photon interaction probability P gets an enhancement of the same factor [40]. Such enhancement can permit one to go beyond the regime in which $\Gamma' \gg \Gamma_{1D}$ of a nanofiber, where emission out of the guided mode dominates.

The first experimental demonstration of the interaction between light propagating in a PCW and quantum systems has been realized with quantum dots by the authors of Ref. [41], which reported a value of about 0.9 for the ratio Γ_{1D}/Γ_{tot}, where $\Gamma_{tot} = \Gamma_{1D} + \Gamma'$ is the total decay rate of the atoms. Implementations with real atoms are much more recent. A Caltech group has demonstrated atom-light coupling using a so-called "alligator" photonic crystal waveguide (APCW) [38, 42–44]. This device, schematically pictured in Fig. 1.7, consists of a pair

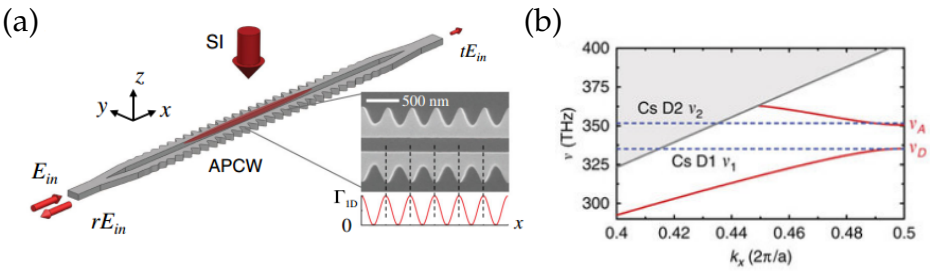

Figure 1.7: (a) The “alligator" PCW. Side illumination (SI) is used to trap the atoms in the red area between the waveguides [38]. Inset: SEM image of the APCW and corresponding single-atom coupling rate Γ_{1D} along the x axis at the center of the gap ($y = 0$). (b) The APCW dispersion relation. The structure is designed in such a way that the D1 and D2 transition frequencies of Caesium, the atomic species used in the experiments, align closely with the band edges.

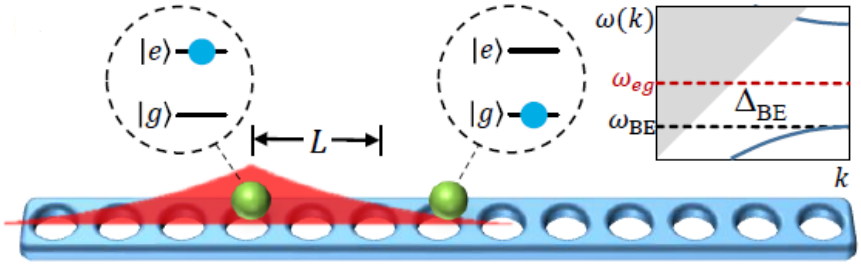

Figure 1.8: Band gap-mediated interaction between two atoms. When ω_{eg} is inside a band gap, as shown in the inset, an excited atom dresses itself with a photonic cloud that decays exponentially from the atomic position (red shade). This virtual photon can facilitate an exchange of spin excitation with a second atom.

of parallel dielectric waveguides whose modes hybridize. The alternation between dielectric and air is obtained by shaping these waveguides in a sinusoidal form. Atoms can be trapped between the two rails by using the reflected field from side illumination, which creates a potential minimum above the plane of the guides, or using far-detuned fields in another guided band, analogously to the fiber case. In the experiment described in Ref. [38], where up to three atoms are trapped and superradiant emission is observed, a value of $\Gamma_{1D}/\Gamma' \approx 1$ is reported.

The potential of PCW's goes beyond the enhancement of atom-photon interactions due to the confinement and slowdown of light. They also permit one to obtain finite-range interactions between atoms using the evanescent modes associated with band gaps, as discussed in greater detail in Chapter 3. When the transition frequency of the atoms lies in a band gap of the

PCW the excited state cannot decay by emitting a propagating photon. Instead, similarly to what happens in CQED, the atom dresses itself with a photon cloud, as illustrated in Fig. 1.8. The main difference from the CQED case is that there the photon component is occupying all the cavity, while here it decays exponentially with the distance from the atom, since it is associated with the evanescent band gap modes [45]. For this reason, it can also be said that an atom-photon "bound state" forms [45, 46]. As it is natural to expect, the spatial extent L of the bound photon depends on the detuning between the band edge and the atomic frequency: the deeper inside the band gap is ω_{eg}, the shorter is L. Similarly to the far-detuned regime of CQED described in the previous section, where virtual cavity photons mediate the interaction between atoms described by Eq. (1.6), here virtual band gap photons create the effective interaction [45–48]

$$H_{bg} = \hbar f_{bg}(x_1, x_2)\left(\sigma_1^{eg}\sigma_2^{ge} + \text{H.c.}\right), \tag{1.10}$$

where $f_{bg}(x_1, x_2) = J_{bg}\exp(-|x_1 - x_2|/L)\, u_k(x_1)u_k(x_2)$. Here J_{bg} is a coupling constant depending on the atomic and photonic crystal properties, while u_k is the Bloch function of the band edge mode [46]. The fundamental difference between the effective atom-atom interaction mediated by the cavity mode, described by Eq. (1.6), and that one mediated by the PCW band gap modes, described by Eq. (1.10), is that the latter has a finite range (see Fig. 1.8). Long-but finite-range spin interactions have begun to attract interest recently, for example, in the context of the propagation of correlations through the system [49–51].

Similarly to the case of CQED, there are two main mechanisms of dissipation which affect the coherent exchange of excitations between atoms in the band gap regime. The first source of dissipation comes from the possibility of losing a band gap mode photon due to imperfections of the PCW. This dissipation mechanism is characterized by the decay rate κ_c. The second source of dissipation comes from the decay rate Γ' of the atoms in non guided modes. In Ref. [46] it is shown rigorously that the minimum error in exchanging an excitation between two atoms under (1.10) scales as $1/\sqrt{C_c}$, where $C_c = g_c^2/\kappa_c\Gamma'$ is an effective cooperativity factor of the PCW. Here, g_c is equal to the strength of interaction that an atom would have with a real cavity of the same size. Recalling that in cavity QED, $C_c \propto \lambda^3 Q/V_{eff}$, one sees that the combination of strong transverse confinement of photons in PCW's and the high achievable quality factors (of up to $Q \sim 10^7$ [52]) enables highly coherent interactions to be realized.

A first experimental observation of this atom-atom interaction using the APCW in the band gap regime is reported in

Ref. [44], where the authors observed a maximum ratio between the coherent coupling J_{bg} and the dissipation rate associated with guided modes Γ_{bg} of 20.

1.3 OVERVIEW OF THE THESIS RESULTS

In the first two sections of this chapter we have reviewed the fields of quantum nonlinear optics using atoms and of nanophotonic systems interfaced with atoms. Here we present an overview of the contributions of the thesis to these fields, introducing its main results.

1.3.1 *Propagating light interacting with atomic ensembles: a new formalism*

In discussing the different approaches for making photons to interact with individual atoms we have seen that in CQED there is a well established input-output formalism [15], which permits one to calculate the quantum properties of the field leaving the cavity, in terms of the input field and the intra-cavity dynamics. This formalism provides two tools: 1) the effective Hamiltonian (1.6) which extends the Jaynes-Cummings model to the case of an open system, *i.e.* a cavity with driving and dissipation, and 2) the input-output relation (1.4), which connects the state of the system, governed by the effective Hamiltonian, and the initial and final states of the external electromagnetic field, which are expressed through the input and output modes.

On the contrary, such an elegant formalism previously had not existed for the case of light interacting with atomic ensembles, neither for free space ensembles, where one has to describe the propagation of light using the Maxwell-Bloch equations under strict approximations, nor for atoms coupled to nanophotonic structures, where a theoretical model was largely missing altogether. Given already the experimental observation of strong photon interactions in Rydberg ensembles, and rapid progress in atom-nanophotonics interfaces, it is highly desirable and important to develop a suitable formalism.

As discussed in Sec. 1.1.2, the problem of atoms interacting with a continuum of propagating field modes constitutes an open, interacting quantum field theory, which is generally difficult to solve. In Chapter 2 of this thesis, we provide a novel approach to this problem. In particular, we show that the field is not an independent degree of freedom and in fact can be integrated out. Thus, analogous to cavity QED, an input-output formalism encodes the correlations of the outgoing propagating field in terms of the incoming field and correlations between

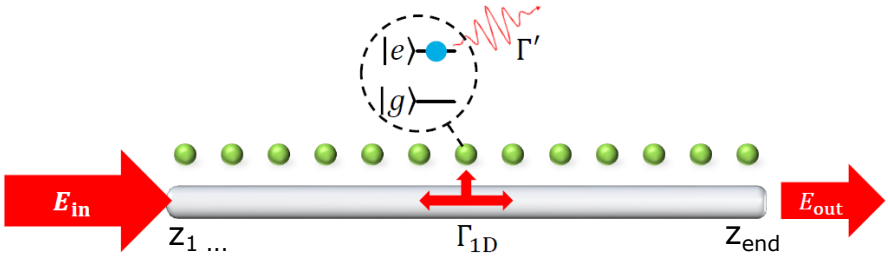

Figure 1.9: Schematic representation of an array of atoms interacting with a 1D waveguide. The atoms emit in the guided mode at a rate Γ_{1D} and into free space modes at a rate Γ'.

the atoms. The atomic dynamics, in turn, reduce to an effective spin model, where “spins" representing the atomic ground and excited states interact through an effective Hamiltonian that physically describes photon-mediated exchange. The reduction to a spin model is appealing, as it potentially enables a variety of condensed matter techniques to be applied, such as a matrix product state ansatz that we explore in detail.

The simplest system where this idea can be applied is the nanofiber with atoms coupled at a fixed distance from its surface, described in Sec. 1.2.1 (see Fig. 1.5a). In such a system atoms interact with a continuum of guided modes, denoted by their wavevector and direction of propagation. The photons in these modes can excite the atoms, and vice versa excited atoms can decay into these modes. Thus the atom-photon interaction Hamiltonian of the system is very similar to Eq. (1.1), summed over the continuum of modes and over all the atoms. The linearity of the atom-guided mode coupling permits one to integrate out the guided modes degrees of freedom, obtaining an input-output relation of the form

$$E_{out}(t) = E_{in}(z_{end}, t) - i\sqrt{\Gamma_{1D}/2}\sum_{j}^{N} e^{ik_0(z_{end}-z_j)}\sigma_j^{ge}, \quad (1.11)$$

which is the analogy of Eq. (1.4) for the waveguide-atom system. As in CQED, absent any atoms the quantum output field after some propagation distance directly corresponds to the field sent into the system. With atoms, the output field also acquires a component emitted from these atoms, which can interfere with the incoming field. Intuitively, the strength of the emitted field should depend on the emission rate into the guided modes Γ_{1D} (see Fig. 1.9), while the term $e^{ik_0(z_{end}-z_j)}$ denotes the propagation phase that the emitted field from atom j picks up as it propagates to the end point of observation.

In order to use the input-output equation, one then needs to understand how the atoms evolve. Indeed, the dynamics of the

atoms are driven by the fields, but according to Eq. (1.11) these in turn just depend on the input field and on the other atoms. One thus finds an effective Hamiltonian of the form

$$H_{\text{eff}} = H_{\text{at}} - i\frac{\Gamma_{1D}}{2}\sum_{j,l=1}^{N} \exp(ik_0|z_j - z_l|)\sigma_j^{eg}\sigma_l^{ge} - \sqrt{\frac{\Gamma_{1D}}{2}}\sum_{j}^{N}\left(E_{\text{in}}(t)e^{ik_0 z_j}\sigma_j^{eg} + \text{H.c.}\right), \quad (1.12)$$

where $H_{\text{at}} = \sum_j(\omega_{eg} - i\Gamma'/2)\sigma_j^{ee}$ for the case of two-level atoms (see Fig. 1.9). H_{at} generally describes all atomic processes except those mediated by the waveguide (in the two-level case, Γ' captures the decay rate of atoms into non-guided modes). The second term of H_{eff} consists of a long-range spin flip interaction between the atoms. It describes the coherent and incoherent exchange of excitation between two atoms mediated by a photon, with the prefactor $\exp(ik_0|z_j - z_l|)$ being the phase acquired by the photon in travelling between the two atoms. Finally the last term describes the driving of the atoms by the input field (similarly to the term describing the driving of the cavity mode in Eq. (1.6)).

While the case of two-level atoms is intuitive, the model can be easily generalized to multi-level structure and extra types of interactions (*e.g.* Rydberg systems). Furthermore, although derived literally for a 1D system, under certain conditions (such as choice of atomic positions) the dynamics ruled by (1.12) can match well the continuum Maxwell-Bloch equations, and thus the 1D effective model can be employed to describe light propagation in 3D ensembles.

This generalization of the input-output formalism of CQED to systems where many atoms interact with propagating light provides an extremely useful theoretical tool for quantum optics. Indeed, the apparently "hard" problem of solving an out-of-equilibrium, open field theory contained in the Maxwell-Bloch equations is now reduced to solving the spin dynamics problem of Eq. (1.12). The field propagation is no longer treated as an independent equation as in Eq. (1.8), but all of its properties are encoded in the input and spins through Eq. (1.11). It is worth to remark the fact that the formalism keeps the same structure as the elegant input-output equations for cavity QED introduced in Sec. 1.1.1.

The Hilbert space associated with the spins has dimension d^N, where d is the local dimension of the atoms. The exponential growth of the Hilbert space with the number of atoms, characteristic of quantum many-body systems, prevents the exact diagonalization of (1.12) for $N \gtrsim 20$. Nevertheless, it is

possible to study the quantum nonlinear dynamics of photons using a weak pulse and limiting the Hilbert space to the subspaces with at most two or three excitations, whose dimensions scale quadratically and cubically with the number of atoms. In Chapter 2 we will apply this formalism to the case of the 1D EIT-Rydberg system discussed in Sec. 1.1.2, recovering the expected results for the transmission of single- and two-photon pulses.

Another important result of the thesis is the formulation of an algorithm to simulate numerically the dynamics generated by (1.12) beyond the weak pulse regime which makes use of the matrix product states (MPS) ansatz, widely used for one-dimensional problems in condensed matter. The MPS ansatz takes advantage of the fact that the dynamics of a typical system might only explore a limited part of the Hilbert space, and adapts to find such a space, making feasible numerical time evolution. This simulation technique thus constitutes the first within quantum optics that can deal exactly with fully quantum light-matter interactions in ensembles, beyond previously explored techniques for two photons [31–33]. The importance of this result is to open the possibility of simulating the many-body regime of quantum nonlinear optics, where phenomena such as quantum phase transitions of light [53–55] or photon crystallization [56, 57] have been speculated to occur, but where the physics still remains very poorly understood. To show the effectiveness of the algorithm developed, we simulate the propagation of a pulse under conditions of vacuum induced transparency (VIT) [58, 59], a nonlinear variation of EIT, whose physics is qualitatively understood and can thus serve to benchmark our method. In particular, one of the spectacular predictions of the theory of VIT, which we can analyze in quantitative detail, is the emergence of a photon number-dependent group velocity. Such an effect is interesting, for example, as it enables photon number-resolving detection, simply based upon the propagation delay time.

1.3.2 *Exotic many-body states of spin and motion in atoms coupled to PCW*

In Sec. 1.2.2 we have described photonic crystal waveguides, nanophotonic structures where the periodic modulation of the dielectric properties can make the propagation of light differ significantly with respect to uniform media. In particular, PCW's enable band gaps, frequency regions where light cannot propagate. We showed that when atoms are coupled to PCW's with

transition frequencies situated within photonic band gaps, strong coherent atomic interactions of tunable range can emerge, Eq. (1.10).

A possibility offered by this platform of atoms coupled to a PCW is that one of simulating long-range interacting spin models [46]. Many atoms interacting with the spin flip interaction $\sigma_j^+\sigma_l^-$ naturally realize an important model of quantum magnetism, the isotropic XY (or XX) spin chain (where the name comes from the form $\sigma_j^x\sigma_l^x + \sigma_j^y\sigma_l^y$ that the spin flip interaction assumes in the Cartesian basis of the Pauli operators). Using more complex schemes, Ising interactions of the form $\sigma_j^z\sigma_l^z$ can also be engineered [46].

While long-range spin models are generally considered interesting [49–51, 60, 61], in Chapter 3 we go a step further and investigate the possibility offered by Hamiltonian (1.10) when the positions of the atoms themselves are treated as dynamical degrees of freedom. The Hamiltonian should then be regarded as a spin-dependent potential, with the atoms feeling forces that depend on the spin correlations with nearby atoms. Note that these forces originate from photons confined to the nanoscale and can thus have a magnitude much larger than that associated to conventional optical trapping. The study of atomic motion driven by spin interactions is inspired by previous investigations into classical self-organization of atoms in cavities or coupled to waveguides, where the atoms have been treated as classical dipoles, with no internal degrees of freedom [62–67]. Here, our goal will be to investigate whether such a system is capable of producing strongly correlated many-body states of atomic spin and motion, where, for example, the spin correlations are crucial to the emergent spatial order. Or more roughly speaking, we are inspired by the question of whether one can create a "quantum crystal," where spin entanglement is responsible for holding the material together.

The PCW-atoms interface enables the realization of many different Hamiltonians, depending on the form of the spin-spin interaction, on the length of the interactions compared with the average atomic distance and on the presence or not of a longitudinal trapping potential. To show the potential of the platform we have focused our investigation on one particular model where atoms are weakly trapped in separated wells, whose potential minima align with nodes of the band gap interaction (see Fig. 1.10). Absent the spin-motion coupling induced by the PCW, clearly the global ground state consists of the atoms being in their individual spin ground states, while the motional states are in the ground states of their respective trapping sites and thus centred at the bottom of each well (see Fig. 1.10a). Our goal is then to investigate the many-body

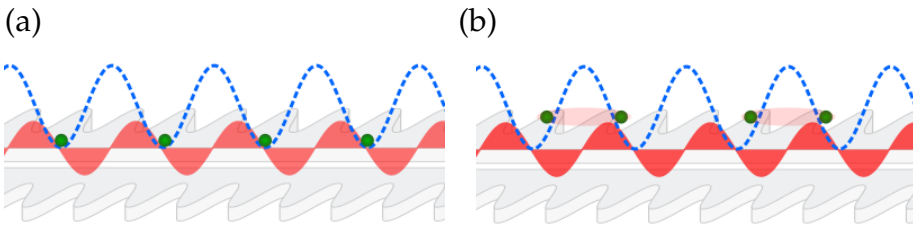

Figure 1.10: Atoms coupled to an APCW. The red shaded curve represents the modulation of the band gap atom-atom interaction, while the blue dashed line is a longitudinal trapping potential. In (a) the spin-spin coupling is too weak and the atoms remain at the bottom of the trapping potential in an uncorrelated state. On the contrary, in (b) the spin-spin interaction overcomes the trapping potential, so that the atoms dimerize, moving from the trap bottom and creating entangled spin correlations (red ellipses).

ground state of spin and motion in the presence of the band gap-mediated interaction. For our specific choice of Hamiltonian (detailed in Chapter 3), we find that one of the non-trivial emergent states resembles a spin-Peierls transition [68–71]. In particular, the spin-spin interaction leads to a spatial dimerization of the atoms in the lattice, causing them to displace *away* from the bottom of each external well, due to the spin entanglement between the atoms in each pair (see Fig. 1.10b). A variety of other exotic phases are possible as well, such as a fluid of composite particles comprised of joint spin-phonon excitations, phonon-induced Néel ordering, and a fractional magnetization plateau associated with trimer formation.

1.3.3 *Graphene as a platform for QNLO*

We have seen at the beginning of this chapter that bulk materials have nonlinear coefficients which are by far too small to realize nonlinear optical processes at the level of single photons. Efforts to implement quantum optical nonlinearities have thus focused on the use of individual atoms, seen as the natural platform for QNLO. Here, we explore the question of whether it is possible for a robust “real-life" material to attain nonlinearities at the single-photon level. Intuitively, one expects that the requirement would be that photons live for a long enough time to accumulate interactions (*i.e.* high Q in a cavity), small mode volume (so that photons are forced to see each other), and some unique mechanism for interaction (beyond a simple saturation effect). Here we argue that graphene favorably satisfies the last two requirements.

Graphene is two-dimensional material, consisting of a honeycomb lattice of carbon atoms, with peculiar electronic, optical and mechanical properties [72]. Its band structure consists of two cones (Dirac cones) touching at their vertexes, with the Fermi energy E_F lying at the contact point, such that the lower band is fully occupied and the upper band empty. Peculiarly, the Fermi level can be shifted electrostatically (doped) from that position, transforming graphene from a zero-gap semiconductor into a metal [72]. For sufficiently high doping $E_F \gtrsim \omega$ graphene has the capability of supporting surface plasmons (SP's) [73–76]. These are electromagnetic waves coupled to charge excitations at the surface of a metal. Compared to conventional plasmonic materials such as noble metals, graphene SP's are much more strongly spatially confined [73]. The ratio between their wavelength and the wavelength of light with the same frequency propagating in free space is $\lambda_{sp}/\lambda_0 \approx 2\alpha E_F/(\hbar\omega)$, where $\alpha \approx 1/137$ is the fine structure constant. In the out-of-plane direction the electric field associated with the plasmon decays exponentially as $E \sim e^{-k_{sp}|z|}$ (with $k_{sp} = 2\pi/\lambda_{sp}$), so that the ratio between the volume of a photon at the diffraction limit and that one of a standing wave plasmon with the same energy on a graphene nanostructure is $(\lambda_0/\lambda_{sp})^3$, a factor which can be as large as 10^6. On the other hand graphene SP's have lifetimes which are comparable with those of noble metals (nanostructures with quality factors of 10-100 have been observed experimentally [77]).

Since the carriers in a SP feel the electromagnetic potential created by the plasmon itself, nonlinear interactions between SP's can be relevant for large enough plasmonic oscillations. Thus one can in principle obtain a nonlinearity where the propagation properties of the light, in this case in the form of SP's, depends on its intensity. This is a very similar to the nonlinearity produced by atoms that we have encountered previously in this chapter and takes the name of third-order nonlinearity. Another kind of nonlinearity, of second-order, describes the mixing of two waves in a medium to produce a third wave whose frequency is a sum or difference of the first two. A simple symmetry argument (explained in detail in Chapter 4) restricts the possibility to have second-order nonlinearities only to materials which are non-centrosymmetric, *i.e.* which have a lattice structure that is non-symmetric under spatial inversion.

We find that graphene, despite being a centro-symmetric material, exhibits second-order nonlinearities. The violation of the no-go theorem is a consequence of the nonlocal character of the interactions between SP's. Indeed, the range of interaction is proportional to the average separation between carriers, given

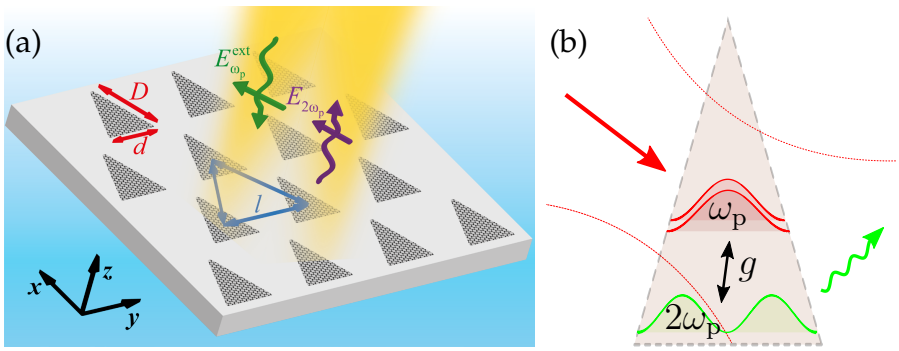

Figure 1.11: (a) An array of triangular graphene nanoislands of the kind described in the text is illuminated with light at frequency ω_p. The nonlinear dynamics of the SP modes in the structures generate emission of light at frequency $2\omega_p$. (b) Schematic representation of the second harmonic generation of (a). The two plasmonic modes are coupled at a rate g. When the first resonance is driven, the nonlinear interaction between the two modes enables the conversion of two quantized plasmons in the first mode to a single plasmon of frequency $2\omega_p$ in the second mode. Radiative emission from this mode realizes SHG.

roughly by the Fermi wavelength λ_F. In noble metals this separation is on the order of an angstrom (0.1 nm), and thus the plasmon-plasmon interaction is local. On the contrary, in graphene the possibility to tune E_F makes it possible to have a density of carriers so low that the interaction range is comparable to λ_{sp}. The resulting nonlocality of the plasmon-plasmon interaction enables second-order nonlinearities.

Having described how graphene exhibits some desirable characteristics to possibly reach the single-photon limit, we then quantitatively analyze the efficiency of down conversion of a single photon into a frequency entangled photon pair (or conversely, second harmonic generation involving just two incident photons). This analysis consists of two separate parts, (i) the strengths of the same processes involving plasmons, and (ii) an analysis of techniques via which plasmons and propagating photons can be reversibly converted.

We identify a simple design for a graphene nanostructure (a triangle with a certain aspect ratio) supporting two plasmonic modes at frequencies ω_p and $2\omega_p$, coupled by the second-order nonlinear interaction between plasmons. We find that, apart from a coefficient depending only on the geometry of the two modes, the rate g at which two quantized plasmons in the lower-order mode and one quantized plasmon in the higher-order mode convert between each other scales as $(g/\omega_p) \sim$

$(\lambda_F/\lambda_{pl})^{7/4}$, verifying the importance of the plasmon wavelength vs. scale of nonlocality.

The strong nonlinearities at the level of plasmons do not convert directly into optical nonlinearities. Indeed, the short lifetime of plasmons causes them to decay through dissipative channels before they can be emitted radiatively as photons. For the modes described above the radiative decay rate κ associated the dipole moment of the modes is of the order of $10^{-7}\omega_p$, with the non-radiative decay Γ' being at least five orders of magnitude larger. A convenient way to increase the coupling of SP's to radiation is to use an array of identical nanostructures. In this way the probability of light-plasmon interaction gets multiplied by the number of structures (for $N\kappa \ll \Gamma'$), as represented in Fig. 1.11a. It is then possible to realize a scheme where incoming light resonant with the fundamental plasmonic resonance produces the emission of light at frequency $2\omega_p$, via the intermediate processes of plasmon excitation, conversion, and re-emission (see Fig. 1.11b). A detailed calculation of the efficiency of this second harmonic generation (SHG) scheme is presented in Chapter 4, where it is shown that a two-photon conversion efficiency of the order of 10^{-8}, comparable to state-of-the-art experiments with crystals [78], can be achieved. In the same Chapter the efficiencies of other processes are also considered for classical and quantum input light.

1.3.4 *Quantum memories with atomic arrays*

In Sec. 1.1.2 we have discussed the possibility of employing atomic ensembles as a tool to create optical quantum nonlinearities, that serve to process the quantum information encoded into photons [20, 22, 79, 80]. Atomic ensembles find a natural application also as quantum memories, systems in which quantum states can be "stored" and then retrieved on demand.

Quantum memories with atomic ensembles are typically realized using three-level atoms [29, 81, 82], where a classical control field maps photonic excitations, resonant on the $|g\rangle - |e\rangle$ transition onto a metastable state $|s\rangle$. The same control field can then be applied to retrieve the stored excitation. The naturally arising figure of merit for the storage process is then the storage efficiency, defined as the ratio between the incoming energy and stored energy. Similarly one can define the retrieval efficiency as the ratio between the energy emitted into the desirable detection channel, *i.e.* a given mode of the electromagnetic field, and the energy that must be emitted during the process. A time reversal symmetry argument shows that these efficiencies share the same upper bound.

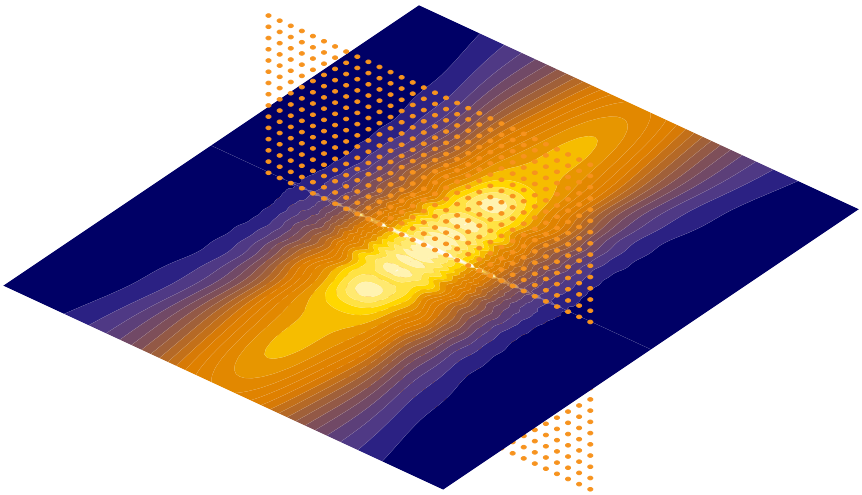

Figure 1.12: The field emitted by a 30×30 atomic array in the $x-y$ plane, when a stored excitation is retrieved. The figure shows a cut of the field in the $y = 0$ plane. (Figure courtesy of Mariona Moreno-Cardoner.)

A systematic study of this bound has lead to the conclusion that the minimum error, *i.e.* the difference between one and the maximum efficiency, scales as the inverse of the ensemble optical depth OD [83] (see Sec. 1.1.2 for its definition). This analysis is however built on the assumption that the emission into modes other than the detection mode is independent of the atomic correlations (independent emission model). This assumption is generally valid for the case of disordered three-dimensional ensembles but breaks down for the case of ordered atomic arrays, *i.e.* systems in which the atoms are regularly positioned [84, 85] (see Fig. 1.12), when the distances between neighbouring atoms are comparable to the resonant wavelength [86].

In Chapter 5 we use the spin model formalism for light propagation in atomic ensembles developed in Chapter 2 to calculate the retrieval efficiency of an atomic array taking into account the exact positions and emissions pattern of all the atoms. We find an elegant expression for the efficiency, where the optimal configuration for the initial distribution of the stored excitation is given by an eigenvalue problem on an $N_a \times N_a$ matrix.

Applying this result to the case of a two-dimensional array with a (non paraxial) Gaussian-like detection mode, we find that the minimum error for optimized initial conditions and value of the mode waist scales as $\epsilon_{opt} \sim (\log \sqrt{N_a})^2/N_a^2$, with proportionality constant of about one. This result reveals the enormous potential of ordered arrays of atoms as a platform for quantum memories. An array with as few as 4×4 atoms is predicted to have the same efficiency of a disordered ensem-

ble having optical depth OD > 100. In the chapter we also study the effect of the presence of imperfections, such as missing atoms or classical disorder in the positions of the atoms, on the efficiency of the memory.

Part II

RESULTS

2

QUANTUM DYNAMICS OF PROPAGATING PHOTONS WITH STRONG INTERACTIONS

2.1 INTRODUCTION

In the first chapter of the thesis we have reviewed how the nonlinearity associated with the anharmonicity of the atomic spectrum can be exploited to create interactions between photons, a crucial ingredient for quantum information processesing and the creation of quantum networks [4]. Different approaches are adopted to make the photons interact strongly with the atoms. In free space one can place the atom between two mirrors, making the photon to bounce back and forth between them and thus increasing the interaction probability with the atom (cavity QED, see Sec. 1.1.1). Alternatively, one can use an atomic ensemble to increase the interaction probability (see Sec. 1.1.2). The use of nanophotonic systems opens new possibilities. For instance, one can confine photons into a one-dimensional dielectric medium, such as a nanofiber with atoms trapped nearby, and take advantage of both the confinement of the light to a small cross-sectional area and of the possibility to couple the optical modes with a large number of atoms at a constant coupling strength (see Sec. 1.2).

We have also seen that to describe the dynamics of photons interacting with a CQED system one has at disposal a powerful theoretical tool, the “input-output" formalism [15]. Within this formalism the continuum of modes of the light degrees of freedom external to the cavity is integrated out. By consequence the internal dynamics is governed by an effective Hamiltonian of the form of Eq. (1.6), where the external field enters only as a single mode, the “input mode", which contains all the information on the free-propagating field before the interaction with the cavity. The field leaving the cavity, the “output mode", can then be expressed through Eq. (1.4) as a sum of the input field and of the cavity field leaking out.

On the contrary, such a simple and elegant tool to describe the dynamics of photons propagating in free space or in a dielectric of reduced dimensionality and interacting with an ensemble of atoms has not existed. For the case of free space atomic ensembles a set of coupled field equations for the (continuous) atomic and field degrees of freedom, the Maxwell-Bloch equations (1.8)-(1.9) [18, 19], is widely used to describe

the light propagation. Unfortunately such equations can only be solved analytically or numerically in a very limited number of cases, typically when the probe field is weak and the atoms respond linearly. The more interesting situations in which non-linearities produce non-classical states of light, such as in the Rydberg-EIT scheme reviewed in Sec. 1.1.2, lie out of the range of validity of the approximations which make Maxwell-Bloch equations exactly solvable.

In the present chapter we show that the input-output formalism of CQED can be readily generalized to the case of atomic ensembles for both light in free-space and guided light. As compared to the Maxwell-Bloch equations, the main advantage provided by the formalism consists of the full elimination of the continuous degrees of freedom associated with the field. Using this method one can reconstruct the dynamics of the photons by solving a driven-dissipative model for the atoms, the "spin model", followed by using a generalized input-output equation to connect the output field with the state of the atomic ensemble.

In Sec. 2.2 we first introduce the generalized input-output formalism for a one-dimensional waveguide coupled with an array of atoms, and then we argue that the simpler 1D waveguide model can be used to describe most of the experiments with three-dimensional ensembles in free space provided that the optical depths of the two systems are matched. In Sec. 2.3 we present the connection between the generalized input-output formalism and the S-matrix formalism for photonic Fock states. In Sec. 2.4 we apply the introduced formalism to a Rydberg-EIT system, studying the transmission properties for a weak probe. Here, the low number of excited atoms enables a truncation of the Hilbert space that makes numerical computation feasible.

In the second part of the chapter we deal with the problem of having high intensity input fields, in which case the number of excitations poses strong limitations to the number of atoms that can be simulated numerically with the spin model. In Sec. 2.5 we show that this limitation can be circumvented by adopting the matrix product state (MPS) ansatz. In particular, this ansatz is based upon the observation that physical systems might only explore a small part of the exponentially large Hilbert space. A time evolution algorithm based upon MPS enables this reduced space to be found in an adaptive way. We test the power of our algorithm in Sec. 2.6, where we simulate the propagation of light in a vacuum induced transparency (VIT) medium.

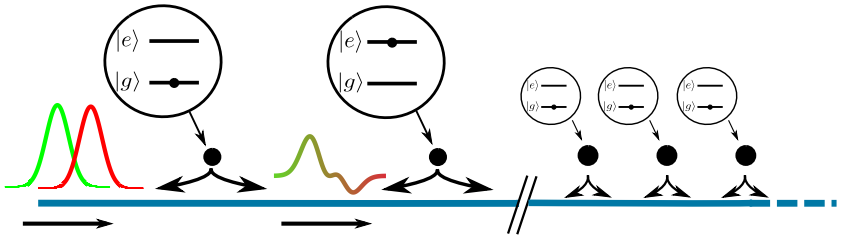

Figure 2.1: Schematic representation of a system of many atoms coupled to a common waveguide. The nonlinearity of an atom enables the generation of a continuum of new frequencies upon scattering of an incoming state. This property, combined with multiple scattering from other atoms, appears to make this system more complicated than the cavity QED case.

2.2 GENERALIZED INPUT-OUTPUT FORMALISM

2.2.1 *Light propagation in a one-dimensional waveguide*

The problem of the propagation of light in a waveguide coupled with an array of atoms, the system introduced in Sec. 1.2.1, has been the subject of intense investigation. In the weak excitation limit, atoms can be treated as linear scatterers and the powerful transfer matrix method of linear optics can be employed to solve the problem exactly [87, 88]. The full quantum case on the other hand has been solved exactly in a limited number of situations in which nonlinear systems are coupled to 1D waveguides [89–99]. The challenge compared to the cavity case arises from the fact that a two-level system is a nonlinear frequency mixer, which is capable of generating a continuum of new frequencies from an initial pulse [100], as schematically depicted in Fig. 2.1. A priori, keeping track of this continuum as it propagates and re-scatters from other emitters appears to be a difficult task. Here we show that the elegant input-output formalism of CQED can be generalized and applied successfully to describe light propagation in the atom-waveguide case.

We consider a generic system composed of many atoms located at positions z_j along a bidirectional waveguide. We assume that there is an optical transition between ground and excited-state levels $|g\rangle$ and $|e\rangle$ to which the waveguide couples, but otherwise we leave unspecified the atomic internal structure and the possible interactions between them (*e.g.*, Rydberg interactions), as such terms do not affect the derivation presented here. The bare Hamiltonian of the system is composed of a term describing the energy levels of the atoms H_{at}, and

a waveguide part $H_{ph} = \sum_{\nu=\pm} \int dk\, \omega_k b^\dagger_{\nu,k} b_{\nu,k}$, where k is the wavevector and $\nu = \pm$ is an index for the direction of propagation, with the plus (minus) denoting propagation towards the right (left) direction. We assume that within the bandwidth of modes to which the atoms significantly couple, the dispersion relation for the guided modes can be linearized as $\omega_k = c|k|$. The interaction between atoms and photons is given in the rotating wave approximation (RWA) by

$$H_{int} = g \sum_{\nu=\pm} \sum_{j=1}^{N} \int dk \left(b_{\nu,k} \sigma_j^{eg} e^{i\nu k z_j} + \text{h.c.} \right), \tag{2.1}$$

which describes the process where excited atoms can emit photons into the waveguide, or ground-state atoms can become excited by absorbing a photon. The coupling amplitude g is assumed to be identical for all atoms, while the coupling phase depends on the atomic position ($e^{i\nu k z_j}$). Here, we will explicitly treat the more complicated bidirectional case, although all of the results readily generalize to the case of a single direction of propagation (chiral waveguide).

In analogy with the input-output formalism of cavity QED [15], we will eliminate the photonic degrees of freedom by formal integration, obtaining that the output field exiting the collection of atoms is completely describable in terms of the input field and atomic properties alone. This formal integration also provides a set of generalized Heisenberg-Langevin equations that governs the atomic evolution. We will then introduce an effective Hamiltonian from which these equations can be derived directly.

The Heisenberg equations of motion for σ_j^{ge} and $b_{\nu,k}$ can be readily obtained by calculating the commutators with H:

$$\dot{b}_{\nu,k} = -i\omega_k b_{\nu,k} - ig \sum_j \sigma_j^{ge} e^{-i\nu k z_j}, \tag{2.2}$$

$$\dot{\sigma}_j^{ge} = i[H_{at}, \sigma_j^{ge}] + ig(\sigma_j^{ee} - \sigma_j^{gg}) \sum_{\nu=\pm} \int dk\, b_{\nu,k} e^{i\nu k z_j}. \tag{2.3}$$

Eq. (2.2) can be formally integrated and Fourier transformed to the field in real space $E_\nu(z,t) \equiv (1/\sqrt{2\pi}) \int dk e^{ikz} b_k$, to obtain the real-space wave equation

$$E_\nu(z,t) = E_{\nu,in}(t - \nu z/c) - \frac{i\sqrt{2\pi} g}{c} \sum_{j=1}^{N} \theta\big(\nu(z - z_j)\big) \sigma_j^{ge}(t - \nu(z - z_j)/c). \tag{2.4}$$

Here we have introduced the input mode $E_{\nu,in}$, mathematically corresponding to the homogeneous solution and physically to

the freely propagating field in the waveguide. The second term on the right consists of the part of the field emitted by the atoms. Inserting Eq. (2.4) into Eq. (2.3), we obtain

$$\dot{\sigma}_j^{ge} = i[H_{at}, \sigma_j^{ge}] + i\sqrt{2\pi}g(\sigma_j^{ee} - \sigma_j^{gg}) \sum_{\nu=\pm} E_{\nu,in}(t - \nu z_j/c) + \frac{2\pi g^2}{c}(\sigma_j^{ee} - \sigma_j^{gg}) \sum_{l=1}^{N} \sigma_l^{ge}(t - |z_j - z_l|/c)). \quad (2.5)$$

Importantly, in realistic systems time retardation can be neglected, resulting in the Markov approximation $E_{\nu,in}(t-\nu z_j/c) \approx E_{\nu,in}(t)e^{i\nu k_0 z_j}$ and $\sigma_l^{ge}(t - |z_j - z_l|/c) \approx \sigma_l^{ge}(t)e^{ik_0|z_j - z_l|}$. Here, $k_0 = \omega_0/c$ is the wavevector corresponding to the central frequency around which the atomic dynamics is centered (typically the atomic resonance frequency ω_{eg}). This approximation is valid when the difference in free-space propagation phases $\Delta\omega L/c \ll 1$ is small across the characteristic system size L and over the bandwidth of photons $\Delta\omega$ involved in the dynamics. As a simple example, the characteristic bandwidth of an atomic system is given by its spontaneous emission rate, corresponding to a few MHz, which results in a significant free-space phase difference only over lengths $L \gtrsim 1$ m much longer than realistic atomic ensembles. A complementary viewpoint of the Markov approximation is that the dispersion of fields in the empty waveguide is negligible compared to the large dispersion introduced by atoms driven near resonance.

We have thus obtained the generalized Heisenberg-Langevin equation

$$\dot{\sigma}_j^{ge} = i[H_{at}, \sigma_j^{ge}] + i\sqrt{\frac{c\,\Gamma_{1D}}{2}}(\sigma_j^{ee} - \sigma_j^{gg}) \sum_{\nu=\pm} E_{\nu,in}(t)e^{i\nu k_0 z_j} + \frac{\Gamma_{1D}}{2}(\sigma_j^{ee} - \sigma_j^{gg}) \sum_{l=1}^{N} \sigma_l^{ge} \exp(ik_0|z_j - z_l|), \quad (2.6)$$

where we have identified $\Gamma_{1D} = 4\pi g^2/c$ as the single-atom spontaneous emission rate into the waveguide modes. If we keep separated the terms proportional to σ_l^{ge} coming from the right and left-going photonic fields, we can find easily that the Lindblad jump operators corresponding to the decay of the atoms into the waveguide are $O_\pm = \sqrt{\Gamma_{1D}/4}\sum_j \sigma_j^{ge} e^{\mp ik_0 z_j}$, in terms of which we can write the master equation for the atomic density matrix $\dot{\rho} = \mathcal{L}[\rho] \equiv -i[H_{at}, \rho] + \sum_{\nu=\pm} 2O_\nu \rho O_\nu^\dagger - O_\nu^\dagger O_\nu \rho - \rho O_\nu^\dagger O_\nu$. We also see that we can derive Eq. (2.6) from a non-Hermitian effective Hamiltonian $H_{sm} = H_{at} + H_{dd,eff} + H_{drive}$, where

$$H_{dd,eff} = -\frac{i\Gamma_{1D}}{2} \sum_{j,l=1}^{N} \sigma_j^{eg}\sigma_l^{ge}\, e^{ik_0|z_j - z_l|}, \quad (2.7)$$

and

$$H_{\text{drive}} = -\sqrt{\frac{c\Gamma_{1D}}{2}} \sum_{\nu=\pm} \sum_{j}^{N} \left(E_{\nu,\text{in}}(t) e^{i\nu k_0 z_j} \sigma_j^{eg} + \text{H.c.} \right). \quad (2.8)$$

In particular, in the following sections we will be concerned with coherent state driving from a single direction ($\nu = +$), in which case $E_{-,\text{in}} = 0$ and $E_{+,\text{in}} \equiv \mathcal{E}_{\text{in}}$ is the incoming coherent state amplitude. The resulting infinite-range interaction between a pair of atoms j,l in (2.7) intuitively results from the propagation of a mediating photon between that pair, with a phase factor proportional to the separation distance. In the following we will refer to the effective Hamiltonian H_{sm}, and the corresponding jumps $O_{\pm}$ associated with dissipation, as the "1D spin model".

Within the same approximations employed above to derive the Heisenberg-Langevin equations we can obtain a generalized input-output relation

$$E_{\nu,\text{out}}(z,t) = E_{\nu,\text{in}}(t) e^{i\nu k_0 z} - i\sqrt{\Gamma_{1D}/(2c)} \sum_{j=1}^{N} \sigma_j^{ge}(t)\, e^{i\nu k_0 (z - z_j)}, \quad (2.9)$$

where the output field is defined for $z > z_R \equiv \max[z_j]$ ($z < z_L \equiv \min[z_j]$) for right(left)-going fields. However, since the right-going output field propagates freely after z_R, it is convenient to simply define $E_{+,\text{out}}(t) = E_{+,\text{out}}(z_R + \epsilon, t)$ as the field immediately past the right-most atom (where ϵ is an infinitesimal positive number), and similarly for the left-going output. The derived relation shows that the out-going field properties are obtainable from those of the atoms alone.

The emergence of infinite-range interactions between emitters mediated by guided photons, and input-output relationships between these emitters and the outgoing field, have been discussed before in a number of contexts [88, 90, 101], but the idea that such concepts could be used to study quantum interactions of photons in extended systems has not been fully appreciated. In Secs. 2.4 and 2.6, we will give concrete examples of the effectiveness of this approach to quantum nonlinear optics. In particular, the infinite-dimensional continuum of the photons is effectively reduced to a Hilbert space of dimension $\dim[\mathcal{H}] = \sum_{j=0}^{n} \binom{N}{j}$ where n is the maximum number of atomic excitations (for $n = N$ we have $\dim[\mathcal{H}] = 2^N$). The atomic dynamics, on the other hand, having been reduced to standard Heisenberg-Langevin equations, quantum jump, or master equations, are solvable by conventional prescriptions [14]. More generally, the statement that quantum optics with atoms

apparently reduces to a spin model (something much more commonly seen in condensed matter) is quite intriguing, and its consequences will be explored from multiple viewpoints throughout this thesis.

In the derivation of the 1D spin model we have thus far ignored the possibility of atomic decay with the emission of a photon into a non-guided mode, *i.e.* into free space. We can account for this decay mechanism by adding a phenomenological independent decay rate Γ' for the excited atoms. This is described by the locally acting Lindblad operator

$$\mathcal{L}_{\text{spont}}[\rho] = -\frac{\Gamma'}{2}\sum_{j=1}^{N}(2\sigma^j_{ge}\rho\sigma^j_{eg} - \sigma^j_{eg}\sigma^j_{ge}\rho - \rho\sigma^j_{eg}\sigma^j_{ge}). \quad (2.10)$$

Our 1D model quantitatively captures the microscopic details of experiments where atoms or other quantum emitters are coupled to 1D channels. This includes atoms coupled to nano-fibers ($\Gamma_{1D}/\Gamma' \sim 0.05$) [34] or photonic crystals ($\Gamma_{1D}/\Gamma' \sim 1$) [38], or "artificial" atoms such as superconducting qubits or quantum dots coupled to waveguides ($\Gamma_{1D}/\Gamma' \gg 1$) [102–105].

2.2.2 *The 1D spin model for 3D atomic ensembles*

The descriptive power of the 1D spin model extends beyond purely one-dimensional systems; in fact, here we will discuss how it can be used to reproduce the macroscopic observables of light propagation in a conventional atomic ensemble. While there are some phenomena in atomic ensembles that are truly three-dimensional, such as radiation trapping [106] and collective emission at high densities [107–109], within the context of generating many-body states of light, the problems of interest largely involve quasi one-dimensional propagation [57, 110–115]. Indeed a typical experimental design is to input light in a single transverse mode and detect the light in the same mode after it traverses the ensemble (see Fig. 2.2).

The standard approach to describe light propagation in such a system is to use Maxwell-Bloch equations [18, 19] in their one-dimensional, paraxial form [17, 31, 33, 83, 110, 116, 117], introduced in Sec. 1.1.2, and that we report here in a slightly different form:

$$(c^{-1}\partial_t \pm \partial_z)E_\pm(z,t) = i\sqrt{\frac{\Gamma_{1D}}{2}}P_{ge}(z,t), \quad (2.11)$$

and

$$\partial_t P_{ge}(z,t) = -i(\omega_{eg} - i\Gamma'/2)P_{ge}(z,t) + i\sqrt{\frac{\Gamma_{1D}}{2}}\left[P_{gg}(z,t) - P_{ee}(z,t)\right]E(z,t) + F(t). \quad (2.12)$$

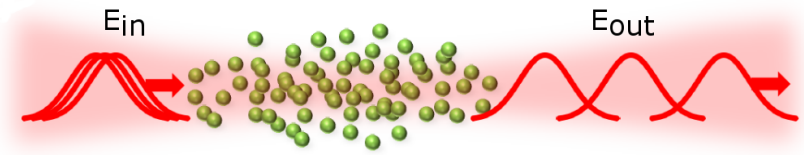

Figure 2.2: Schematic representation of a quantum optics experiment with a three-dimensional atomic ensemble trapped in free space. Both the input and output modes consist of the same transverse Gaussian mode.

Again, here P_{ge} denotes a continuous atomic polarization density operator, where the discreteness of atoms has been smoothed out. The difference with respect to the equations presented in the first chapter is that here we have introduced the coupling rate Γ_{1D} of an individual atom to the one-dimensional input mode. In principle, this rate can vary with z depending on the details of this mode, but for notational simplicity we assume here that it is constant. In this standard formulation of the Maxwell-Bloch equations, it should be noted that the interaction of the atoms with the remaining continuum of three-dimensional modes is reduced to an independent emission rate Γ', meant to approximately capture scattering of photons out of the transverse mode of interest. The question of when this approximation breaks down is quite complicated and rich [86, 110, 118] and will not be discussed here; in any case, Eqs. (2.11)-(2.12) are widely accepted as the standard model for quasi-1D light propagation through atomic ensembles [17].

It should be noted that Eqs. (2.11) and (2.12) have nearly the same form as the Heisenberg equations of motion of the 1D waveguide, Eqs. (2.2) and (2.3). The independent emission Γ' is also captured by the phenomenological Lindblad term added to the 1D evolution, Eq. (2.10). It can be seen that the only difference between the Maxwell-Bloch equations and the 1D model is that in the latter, the discreteness of the atoms is explicitly retained through their positions z_j. These can in fact be chosen in a way to reproduce phenomena associated with free-space ensembles. In particular, as we discuss below, our numerical calculations are facilitated by choosing ratios of $\Gamma_{1D}/\Gamma' \sim 1$. It is known that for a weak resonant input field, a single two-level atom in a waveguide can produce an appreciable reflectance of $\Gamma_{1D}^2/(\Gamma_{1D}+\Gamma')^2$ [119, 120]. The reflectance can be further enhanced if multiple atoms are placed on a lattice with lattice constant defined by $k_0 a = \pi$, in which case the reflectance from

individual atoms constructively interferes [88, 121, 122]. While it is possible to observe similar effects in atomic ensembles [123, 124], this situation is atypical and will not be discussed further here. To reproduce the typical case in atomic ensembles where reflection is negligible, we thus always choose a spacing $k_0 a = \pi/2$, in which reflection from different atoms in the lattice destructively interferes.

In this configuration, the 1D waveguide model reproduces one of the key features of an atomic ensemble, that of decay of the transmitted field with increasing optical depth. If we consider the transmittance $T = \langle E_{out}^\dagger E_{out} \rangle / |\mathcal{E}_{in}|^2$, then for a resonant weak coherent state input we find in the 1D waveguide model $T = \exp(-OD)$, where the optical depth is $OD = 2N\Gamma_{1D}/\Gamma'$ for $\Gamma_{1D} \lesssim \Gamma'$[125]. Since $OD \lesssim 10^2$ in realistic atomic ensembles, by artificially choosing $\Gamma_{1D} \sim \Gamma$, the same optical depth is achieved with just tens or hundreds of atoms. This exponential decay of a resonant incoming field in a two-level atomic gas takes the name of Beer's law and is the solution of the Maxwell-Bloch equations in the linear regime given a resonant input field.

One can get an intuition of how Beer's law can be obtained from the spin-model by considering a single atom coupled to the waveguide. For a weak probe one can ignore saturation, obtaining a steady-state atomic coherence of

$$\langle \sigma^{ge} \rangle = \frac{\mathcal{E}_{in}\sqrt{c\Gamma_{1D}/2}}{\delta + i(\Gamma_{1D} + \Gamma')/2}, \tag{2.13}$$

where $\delta = \omega - \omega_{eg}$ is the detuning of the input field frequency from the atomic resonance. Using this result in the input-output relation (2.9) one can get the output state and the single atom transmittance

$$T_1(\delta) = \left| \frac{\delta + i\Gamma'/2}{\delta + i(\Gamma_{1D} + \Gamma')/2} \right|^2. \tag{2.14}$$

For $\Gamma_{1D} \ll \Gamma'$ and on resonance one can expand the transmittance as $T_1(0) \approx 1 - 2\Gamma_{1D}/\Gamma'$. For N atoms in the spatial configuration $k_0 a = \pi/2$ where atomic reflection destructively interferes, the linear response is then approximately given by the product of the single-atom transmittance. Then $T_N \approx \exp(-2N\Gamma_{1D}/\Gamma')$, from which we get the expression for the optical depth reported above. More rigorously one can solve the spin model for N atoms under weak driving and use the input-output equation to reconstruct the output field and the transmittance. In Fig. 2.3 we plot the transmittance spectrum obtained in this way for different values of the ratio Γ_{1D}/Γ and of the number of atoms N

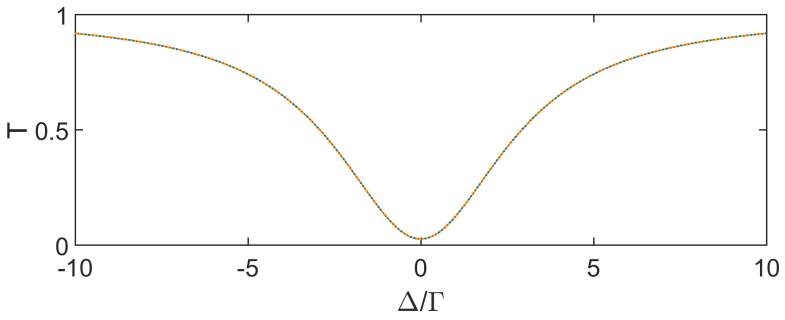

Figure 2.3: Transmittance spectrum obtained by solving the spin model with a constant optical depth OD = 5 but different values for the number of atoms N and the waveguide decay rate Γ_{1D}. The three (undistinguishable) lines corresponds to $N = 50$, $\Gamma_{1D} = 0.1\Gamma'$ (continuous blue line), $N = 20$, $\Gamma_{1D} = 0.25\Gamma'$ (red dashed line) and $N = 10$, $\Gamma_{1D} = 0.5\Gamma'$ (yellow dotted line).

but having the same optical depth $OD = 2N\Gamma_{1D}/\Gamma$. One can appreciate from the figure that, as anticipated, the transmittance depends only on the optical depth.

2.3 RELATION TO S-MATRIX ELEMENTS

In the previous section we have presented an extended input-output formalism to describe light propagation in one-dimensional systems. We have seen that the formalism can be readily used to calculate the transmitted and reflected fields when the input field is a coherent state, by solving for the dynamics of a particular driven spin Hamiltonian and constructing the output field in terms of the atomic solution by means of an input-output relation. The dynamics of few-photon states can also be approached from the point of view of scattering theory. Within this formalism the dynamics of photons is provided by the scattering matrix (S-matrix). Physically, the S-matrix provides, for a given input field consisting of a number of monochromatic (plane-wave) photons, the output field decomposed as a sum of monochromatic photon states. As the set of plane waves forms a complete basis, the full S-matrix associated with a given system enables the problem of photon propagation to be completely solved.

The connection between the S-matrix formalism and the standard input-output formalism of quantum optics has been first presented in Ref. [90], where the asymptotic incoming and outgoing photonic states, which provide the basis over which the S-matrix is defined, have been associated with the Fock states

created by the (Fourier transformed) input and output field operators. This connection for an n-photon process takes the form

$$\begin{aligned} S^{(n)}_{\mathbf{p};\mathbf{k}} &= \langle \mathbf{p} | \, S \, | \mathbf{k} \rangle \\ &= \langle 0 | \, b_{out}(p_1)..b_{out}(p_n) b^{\dagger}_{in}(k_1)..b^{\dagger}_{in}(k_n) \, | 0 \rangle \\ &= \mathcal{FT}^{(2n)} \, \langle 0 | \, b_{out}(t_1)..b_{out}(t_n) b^{\dagger}_{in}(t'_1)..b^{\dagger}_{in}(t'_n) \, | 0 \rangle \, , \end{aligned} \tag{2.15}$$

where the input and output creation operators respectively create freely propagating incoming and outgoing photonic states. The n-dimensional vectors $\mathbf{p}$ and $\mathbf{k}$ denote the outgoing and incoming frequencies of the n photons. The input and output operators can be any combination of + and - propagation directions (we have omitted this index here for simplicity). In the last line we have used a global Fourier transformation $\mathcal{FT}^{(2n)} = (2\pi)^{-n} \int \prod_{i=1}^{n} \, dt_i dt'_i \, e^{i(t_i p_i - t'_i k_i)}$, to express the S-matrix in terms of time correlations of the input and output fields. In Eq. (2.15) we have assumed implicitly that the number of photons is conserved for simplicity but the theory can be easily extended to the more general case of non-conservation of the number of excitations (we will give examples in Chapter 4 in the context of second harmonic generation). While Eq. (2.15) has been used to calculate the S-matrix elements in a limited number of cases in Ref. [90], here we go a step further showing that the input-output relation can be used to express all the matrix elements in terms of atomic operators only. A similar conclusion has been derived simultaneously and independently in Ref. [126].

For notational simplicity, we give here a derivation for a single spin and a monodirectional waveguide, but its generalization to the bidirectional waveguide and many atoms is straightforward. For our purpose it is enough to have an input-output relation of the form

$$b_{out} = b_{in} - i\sqrt{\gamma}\sigma^{ge}. \tag{2.16}$$

We begin by noting that Eq. (2.16) enables one to replace output operators by a combination of system and input operators, or input operators by system and output operators. Selectively using these substitutions, one can exploit favorable properties of either the input or output field, in order to gradually time order all of the system operators (where operators at later times appear to the left of those at earlier times), while removing input and output operators from the correlation.

Since the output operators commute between themselves because of the indistinguishability of photons, they can be freely ordered by decreasing times. Introducing the time ordering op-

erator T and also using Eq. (2.16), the operators in Eq. (2.15) can be written as

$$T\left[\left(b_{in}(t_1)-i\sqrt{\gamma}\sigma^{ge}(t_1)\right)..\left(b_{in}(t_n)-i\sqrt{\gamma}\sigma^{ge}(t_n)\right)\right] b^{\dagger}_{in}(t'_1)..b^{\dagger}_{in}(t'_n). \tag{2.17}$$

This expression can be expanded as a sum and each of its terms can be labelled by the number m of system operators σ^{ge} present. Also, thanks to the fact that $[\sigma^{ge}(t), b_{in}(t')] = 0$ for $t' > t$, all the input operators can be moved to the right of the spin operators in each term. Thus, the generic term of order m will be of the form

$$\langle 0|\, T\left[\sigma^{ge}(t_1)..\sigma^{ge}(t_m)\right] b_{in}(t_{m+1})..b_{in}(t_n)b^{\dagger}_{in}(t'_1)..b^{\dagger}_{in}(t'_n)\,|0\rangle\,, \tag{2.18}$$

which can be immediately simplified using the commutation relations between input operators $[b_{in}(t), b^{\dagger}_{in}(t')] = \delta(t-t')$. This manipulation results in a sum of $(n!)^2/(m!)^2(n-m)!$ terms for each original term of order m. Each term of the sum consists of $n-m$ delta functions multiplied by a correlation function of the form

$$\langle 0|\, T\left[\sigma^{ge}(t_1)..\sigma^{ge}(t_m)\right] b^{\dagger}_{in}(t'_1)..b^{\dagger}_{in}(t'_m)\,|0\rangle\,. \tag{2.19}$$

Since the σ^{ge} operators commute with the $b^{\dagger}_{in}$ operators at later times, the time ordering operator can be extended to all the operators in the correlation function. Using again Eq. (2.16) to express the input operators one gets

$$\begin{aligned}&\langle 0|\, T\left[\sigma^{ge}(t_1)..\sigma^{ge}(t_m)\times\right.\\ &\left.\times\left(b^{\dagger}_{out}(t'_1)-i\sqrt{\gamma}\sigma^{eg}(t'_1)\right)..\left(b^{\dagger}_{out}(t'_m)-i\sqrt{\gamma}\sigma^{eg}(t'_m)\right)\right]|0\rangle\,.\end{aligned} \tag{2.20}$$

However, since the operators $b^{\dagger}_{out}$ commute with all the operators σ^{ge} on the left, only

$$\langle 0|\, T\left[\sigma^{ge}(t_1)..\sigma^{ge}(t_m)\sigma^{eg}(t'_1)..\sigma^{eg}(t'_m)\right]|0\rangle \tag{2.21}$$

remains, which proves that the S-matrix elements can be expressed as a sum of (time-ordered) atomic correlation functions. Note that in Eq. (2.21) the operators are in the Heisenberg picture, *i.e.* $\sigma^{ge}(t) = e^{iHt}\sigma^{ge}e^{-iHt}$, where H is the Hamiltonian of the whole system without the driving field, and the vacuum state $|0\rangle$ stands for $|0\rangle_b\,|g\rangle^{\otimes N}$, *i.e.* the vacuum state of field modes and the ground state of all the atoms.

Moreover, using the general expression for the Heisenberg-Langevin equation and the quantum regression theorem, it can

be proven that when any auxiliary fields driving the system do not generate waveguide photons, the correlation function of Eq. (2.21) can be evaluated by evolving $\sigma^{ge}(t)$ as $e^{iH_{eff}t}\,\sigma^{ge}\,e^{-iH_{eff}t}$ where $H_{eff} = H_{at} + H_{dd,eff}$ is the effective Hamiltonian of the atom, with $H_{dd,eff}$ described in the previous section. Although such a form for $\sigma^{ge}(t)$ is not true in general due to quantum noise, these noise terms have no influence on the correlation. We can prove this statement by taking the term with $t_1 > t_2 ... > t_m > t'_1 > t'_2 ... > t'_m$ as an example (our argument holds for any time ordering). The quantum regression theorem is applied here to eliminate the bath or photonic degrees of freedom, and results in

$$\begin{aligned}\langle 0|_b \langle 0|\, \sigma^{ge}(t_1)...\sigma^{ge}(t_m)\sigma^{eg}(t'_1)..\sigma^{eg}(t'_m)\, |0\rangle_b |0\rangle = \\ \mathrm{Tr}[\sigma^{ge}e^{\mathcal{L}(t_1-t_2)}\sigma^{ge}...\sigma^{eg}e^{\mathcal{L}(t_{m-1}-t_m)}\sigma^{eg}\rho(0)],\end{aligned} \quad (2.22)$$

where $\rho(0) = |g\rangle\langle g| \otimes |0\rangle_b \langle 0|$ and $\mathcal{L}$ is the Lindblad superoperator corresponding to the effective spin model. $\mathcal{L}$ contains a deterministic part, which generates an evolution driven by H_{eff} and which conserves the number of excitations, and a jump part, which reduces the number of atomic excitations. Because of the form of the correlators, which contain an equal number of atomic creation and annihilation operators, the jump part of the evolution of the operators gives a vanishing contribution to the correlation function, proving what was stated above.

While the discussion has thus far been completely general, the case of S-matrix elements involving only one or two photons can be formally reduced to particularly simple expressions. For example, it can be shown easily that the weak probe transmission coefficient $T(k)$ for the many-atom, bi-directional waveguide case introduced in the previous section is related to the S-matrix by $S^{(1)}_{p+;k+} \equiv \langle 0|\, b_{+,out}(p) b^\dagger_{+,in}(k)\, |0\rangle \equiv T(k)\delta(p-k)$. Furthermore, it can be expressed in terms of a known $\sim N \times N$ matrix corresponding to the single-excitation Green's function G_0 (whose form varies depending on the system details),

$$T(k) = 1 - \frac{i\Gamma_{1D}}{2}\sum_{ij}\left[G_0(k)\right]_{ij} e^{-ik_{in}(z_i - z_j)}. \quad (2.23)$$

Similarly, the two-photon S-matrix in transmission is generally given by

$$\begin{aligned}S^{(2)}_{p_1+,p_2+;k_1+,k_2+} &= T_{k_1}T_{k_2}\delta_{p_1k_1}\delta_{p_2k_2} \\ &- i\frac{\Gamma_{1D}^2}{8\pi}\delta_{p_1+p_2,k_1+k_2}\sum_{iji'j'} W_{ij}T_{ij;i'j'}W_{i'j'} + (p_1 \leftrightarrow p_2),\end{aligned} \quad (2.24)$$

where the first and second terms on the right describe the linear and nonlinear contributions, respectively. The latter term

can be expressed in terms of matrices W related to the single-excitation Green's function, and a known $\sim N^2 \times N^2$ matrix T characterizing atomic nonlinearities and interactions.

2.4 LIGHT PROPAGATION IN A RYDBERG-EIT MEDIUM

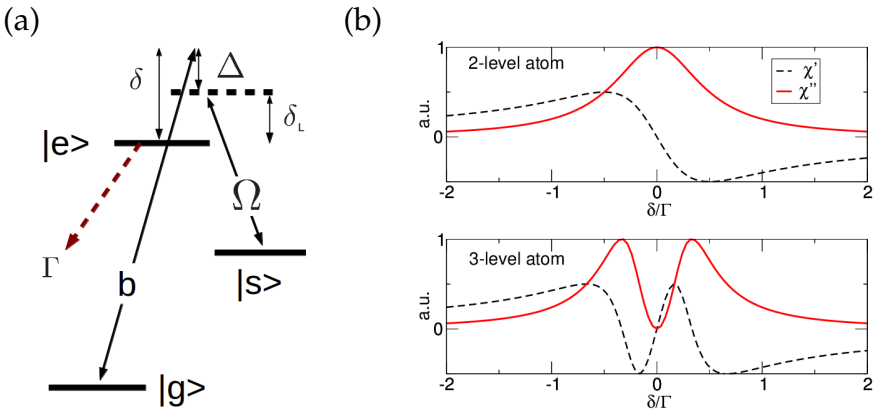

Figure 2.4: (a) EIT level scheme. The atomic ground ($|g\rangle$) and excited states ($|e\rangle$) interact with the quantum propagating field b of the waveguide. An additional classical field with Rabi frequency Ω couples state $|e\rangle$ to a metastable state $|s\rangle$. The total single-atom linewidth of the excited state is given by Γ. (b) The real (χ') and imaginary (χ'') parts of the linear susceptibility for a two-level atom (upper panel) and three-level atom (lower panel), as a function of the dimensionless detuning δ/Γ of the field b from the resonance frequency of the $|g\rangle$-$|e\rangle$ transition. For the three-level atom, the parameters used are $\delta_L = 0$ and $\Omega/\Gamma = 1/3$.

In this section, we apply the formalism presented in Sec. 2.2 to a specific example involving three-level atoms under conditions of electromagnetically induced transparency (EIT) and with Rydberg-like interactions between atoms [28, 31–33, 127]. This scheme was briefly introduced in Sec. 1.1.2, and we review it in greater detail here. The linear susceptibility for a two-level atom with states $|g\rangle$ and $|e\rangle$, in response to a weak probe field with detuning $\delta = \omega_p - \omega_{eg}$ from the atomic resonance, is shown in Fig. 2.4b. It can be seen that the response on resonance is primarily absorptive, as characterized by the imaginary part of the susceptibility (χ'', red curve). In contrast, the response can become primarily dispersive near resonance if a third level $|s\rangle$ is added, and if the transition $|e\rangle - |s\rangle$ is driven by a control field (characterized by Rabi frequency Ω and single photon detuning $\delta_L = \omega_L - \omega_{es}$). Specifically, via interference between the probe and control fields, the medium can become transparent to the probe field ($\chi'' = 0$) when two-photon resonance is achieved, $\delta - \delta_L = 0$, realizing EIT [21,

29]. In this process, the incoming probe field strongly mixes with spin wave excitations σ^{sg} to create "dark-state polaritons". The medium remains highly transparent within a characteristic bandwidth Δ_{EIT} around the two-photon resonance, which reduces to $\Delta_{EIT} \sim 2\Omega^2/(\Gamma\sqrt{OD})$, when $\delta_L = 0$. Here $\Gamma = \Gamma' + \Gamma_{1D}$ is the total single-atom linewidth, and OD is the optical depth of the atomic ensemble. These polaritons propagate at a strongly reduced group velocity $v_g \ll c$, as indicated by the steep slope of the real part of the susceptibility χ' in Fig. 2.4b, which is proportional to the control field intensity [21, 29].

Taking σ_j^{se} to be the lowering operator from $|e_j\rangle$ to $|s_j\rangle$, EIT is described within our spin model by the effective spin Hamiltonian

$$H_{EIT} = -\left(\delta_L + i\frac{\Gamma'}{2}\right)\sum_j \sigma_j^{ee} - \Omega\sum_j(\sigma_j^{es} + \sigma_j^{se}) - i\frac{\Gamma_{1D}}{2}\sum_{j,l} e^{ik_{in}|z_j - z_l|}\sigma_j^{eg}\sigma_l^{ge}, \quad (2.25)$$

where the first line represents the explicit form of H_{at} for the EIT three-level atomic structure. In addition to waveguide coupling, here we have added an independent atomic decay rate Γ' into other channels (*e.g.*, unguided modes), yielding a total single-atom linewidth of $\Gamma = \Gamma' + \Gamma_{1D}$.

The spin model of EIT, *i.e.* Eq. (2.25), can be exactly solved in the linear regime using the transfer matrix formalism [88], which correctly reproduces the free-space result and dependence on optical depth of the group velocity $v_g = 2\Omega^2 n/\Gamma_{1D}$ and transparency window Δ_{EIT}, where n is the (linear) atomic density. The corresponding minimum spatial extent of a pulse that can propagate inside the medium with high transparency is given by $\sigma_{EIT} = v_g/\Delta_{EIT}$.

A single photon propagating inside an ensemble of atoms under EIT conditions is coherently mapped onto a single dark polariton, corresponding to a delocalized spin wave populating the single excitation subspace of the atomic ensemble. The polariton dynamics can be therefore visualized directly by monitoring the excitation probability $\langle\sigma_j^{ss}\rangle$ of the atoms in the ensemble. In Fig. 2.5, we initialize a single polariton inside the medium with an atomic wave function of the form $|\psi\rangle = \sum_j f_j\sigma_j^{sg}|g\rangle^{\otimes N}$, and we determine numerically the time evolution under H_{EIT} in Eq. 2.25 up to a final time t_f. Choosing an initially Gaussian spin wave, $f_j = \exp(ik_{in}dj)\exp(-(jd-\mu)^2/4\sigma_p^2)/(2\pi\sigma_p^2)^{1/4}$, with spatial extent σ_p (blue line), one sees that the wavepacket propagates a distance $v_g t_f$, and with little loss provided that $\sigma_p > \sigma_{EIT}$. Numerics (green line) show perfect agreement with

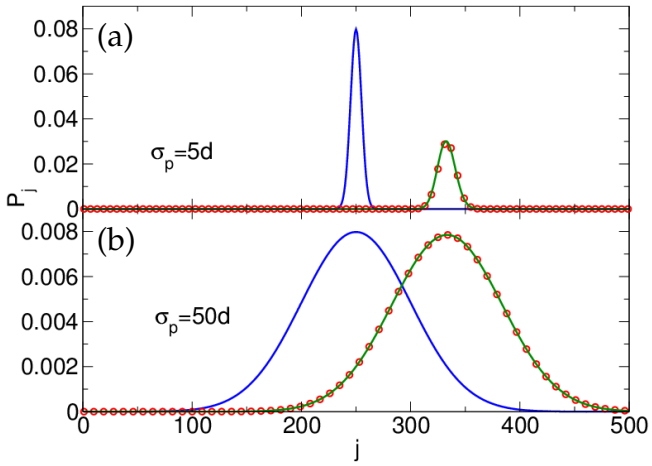

Figure 2.5: EIT: single polariton propagation for $\sigma_p < \sigma_{EIT}$ (a) and $\sigma_p > \sigma_{EIT}$ (b). Plotted is the population $P_j = \langle \sigma_j^{ss} \rangle$ of atom j in the state $|s\rangle$. The blue line corresponds to the initial state, the green line to the state numerically evolved over a time t_f, and the red dots to the theoretically predicted evolution. Other parameters: $t_f v_g = Nd/6$, $\Gamma' = 5$, $\Gamma_{1D} = 10$, $\Omega = 1$, $N = 500$ and $\sigma_{EIT} \sim 22d$, where d is the lattice constant.

theoretical predictions (red lines) obtained via the transfer matrix formalism [88].

The spin model formalism can be easily extended to include arbitrary atomic interactions, providing a powerful tool to study quantum nonlinear optical effects. As a concrete example, we consider a system in which atoms can interact directly over a long range, such as via Rydberg states [57, 111, 128] or photonic crystal bandgaps [46]. The total Hamiltonian is given by

$$H_{EIT-Ryd} = H_{EIT} + \frac{1}{2} \sum_{j,l} U_{jl} \sigma_j^{ss} \sigma_l^{ss} + H_{drive}, \tag{2.26}$$

in which U_{jl} represents a dispersive interaction between atoms j and l when they are simultaneously in state $|s\rangle$. As we are primarily interested in demonstrating the use of our technique, we take here a "toy model" where atoms experience a constant infinite-range interaction, $U_{jl}/2 \equiv C$. Such a case enables the numerical results to be intuitively understood, although we note that other choices of U_{jl} do not increase the numerical complexity. In particular we are interested in studying the propagation of a constant weak coherent input field through the atomic ensemble. The corresponding driving then is given by $H_{drive} = \mathcal{E} \sum_j (\sigma_j^{eg} e^{ik_{in} z_j} e^{-i\Delta t} + \sigma_j^{ge} e^{-ik_{in} z_j} e^{i\Delta t})$, where $\mathcal{E} \ll \Gamma$ is the amplitude of the constant driving field, $\Delta = \delta - \delta_L$ the detuning from two photon resonance condition, and the initial state is given by the global atomic ground state $|\psi_i\rangle = |g\rangle^{\otimes N}$ [119, 129]. With infinite-range interaction, one spin flip to state $|s\rangle_{\tilde{j}}$ shifts the

energies of all other states $|s\rangle_j$ by an amount C. A second photon should then be able to propagate with perfect transparency, provided it has a detuning compensating for the energy shift C, thus ensuring the two-photon resonance condition is satisfied. As we result, we expect to see a transparency window for two photons, whose central frequency shifts linearly with C.

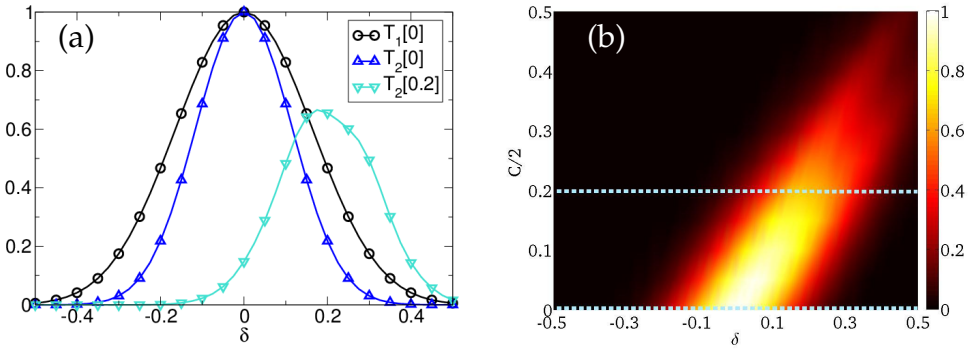

Figure 2.6: (a) Single-photon (circles) and two-photon (triangles) transmission spectrum for a weak probe field, for selected values $C/2 = 0$ and $C/2 = 0.2$ of the infinite-range interaction strength. The linear transmission is independent of C, while the two-photon spectrum exhibits a shift in the maximum transmission by an amount $C/2$. Other parameters: $N = 200$, $\Gamma_{1D} = 1, \Gamma' = 3$, $\Omega = 2$, $\delta_L = 0$, $\mathcal{E} = 10^{-6}$. (b) Contour plot of the two-photon transmission spectrum $T_2 = \langle E^\dagger_{+,out}(t)E^\dagger_{+,out}(t)E_{+,out}(t)E_{+,out}(t)\rangle/\mathcal{E}^4$, as functions of interaction strength $C/2$ and two photon detuning $\Delta = \delta$ ($\delta_L = 0$). Cuts of the contour plot (illustrated by the dashed lines) are plotted in (a).

This predicted behavior can be confirmed by plotting the transmitted intensity fraction

$$T_1 = I/I_{in} = \langle E^\dagger_{+,out}(t)E_{+,out}(t)\rangle/\mathcal{E}^2, \tag{2.27}$$

and also the second-order correlation function

$$T_2 = \langle E^\dagger_{+,out}(t)E^\dagger_{+,out}(t)E_{+,out}(t)E_{+,out}(t)\rangle/\mathcal{E}^4, \tag{2.28}$$

which corresponds roughly to the two-photon transmission. Fig. 2.6 shows the single-photon transmission T_1 and two-photon transmission T_2 as a function of the interaction strength C and detuning from two photon resonance Δ. To generate these plots, we have taken a weak coherent state input, and truncated the Hilbert space to two maximum atomic excitations (such that the Hilbert space size is proportional to N^2), which makes a numerical solution tractable even for relatively large numbers of atoms ($N = 200$ for Fig. 2.6). As expected, T_1 shows a peak at $\Delta = 0$ independently of the interaction intensity C; instead

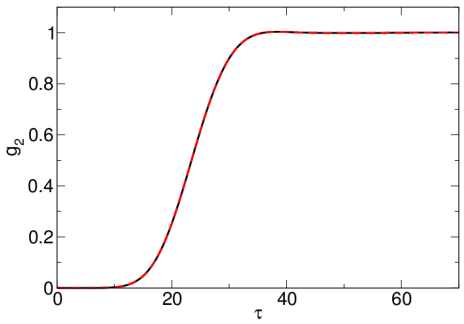

Figure 2.7: Comparison of $g^{(2)}(\tau)$ evaluated by numerical simulations (red dashed line) and S-matrix theory (black line). For constant infinite range interactions $C = 1$ and $\Delta = 0$, the interactions induce photon antibunching. Other parameters: $N = 20$, $\Gamma_{1D} = 2, \Gamma' = 2$, $\Omega = 1$, $\delta_L = 0$, $\mathcal{E} = 10^{-6}$.

the peak in T_2 shifts towards $\Delta = C/2$ with increasing C. The decay of T_2 for increasing C can be intuitively understood by noting that we have a constant coherent state input, in which photons are randomly spaced, causing two photons to enter the medium at different times. Thus, until the second photon enters, the first photon propagates as a single polariton detuned by Δ from the single-photon transparency condition, getting partially absorbed in the process. By increasing the interaction we increase the detuning for this single polariton and consequently its absorption, explaining the trend observed for T_2 in Fig. 2.6b.

Field correlation functions like intensity $I = \langle E^\dagger_{+,out}(t)E_{+,out}(t)\rangle$ or $g_2(\tau) = \langle E^\dagger_{+,out}(t)E^\dagger_{+,out}(t+\tau)E_{+,out}(t+\tau)E_{+,out}(t)\rangle/I^2$ can be computed according to the following strategy. First we switch from Heisenberg representation to Schrödinger representation, so that for the intensity we get

$$I = \langle E^\dagger_{+,out}(t)E_{+,out}(t)\rangle = \langle\psi(t)|E^\dagger_{+,out}E_{+,out}|\psi(t)\rangle. \qquad (2.29)$$

The time evolved wave function, $|\psi(t)\rangle$, is determined by numerically evolving the initial spin state $|\psi_i\rangle$ under H for a time t. Then, the state immediately after detection of one photon, $E_{+,out}|\psi(t)\rangle = |\phi\rangle$, is evaluated by expressing $b_{+,out}$ in terms of spin operators using the input-output formalism: $E_{+,out} = \mathcal{E}e^{ik_{in}z_R} - i\Gamma_{1D}/2\sum_j \sigma_{ge}e^{ik_{in}(z_R-z_j)}$. Finally we obtain the intensity by computing the probability of the one-photon detected state, $I = \langle\phi|\phi\rangle$. For $g_2(\tau)$ an extra step is needed. Its numerator describes the process of detecting two photons, the first at time t and the second at time $t+\tau$: $f(t+\tau) = \langle E^\dagger_{+,out}(t)E^\dagger_{+,out}(t+\tau)E_{+,out}(t+\tau)E_{+,out}(t)\rangle$. As before we can switch to the Schrödinger picture, $f(t+\tau) = \langle\psi(t)|E^\dagger_{+,out}e^{iH\tau}E^\dagger_{+,out}E_{+,out}e^{-iH\tau}E_{+,out}|\psi(t)\rangle$, and evaluate the state after dectection of the first photon, $E_{+,out}|\psi(t)\rangle =$

$|\phi\rangle$. Then detection of a second photon after a time τ entails performing an extra evolution under H and annihilating a photon, that is: $E_{+,out}e^{-iH\tau}|\phi\rangle = E_{+,out}|\phi(\tau)\rangle$. Finally, we evaluate the quantity $f(t+\tau) = \langle\phi(\tau)|E^{\dagger}_{+,out}E_{+,out}|\phi(\tau)\rangle$, by again expressing $E_{+,out}$ in terms of spin operators. In Fig. 2.7, we plot the numerically obtained result for $g^{(2)}(\tau)$, for the case where infinite-range interactions are turned on ($C = 1$) and for a weak coherent input state with detuning $\Delta = 0$. In such a situation, one expects for the single-photon component of the coherent state to transmit perfectly, while the two-photon component is detuned from its transparency window and becomes absorbed. This nonlinear absorption intuitively yields the strong anti-bunching dip $g^{(2)}(\tau = 0) < 1$. We also evaluate this second-order correlation function using the analytical result for the two-photon S-matrix in Eq. (2.24), which shows perfect agreement as expected.

2.5 HIGH INTENSITY INPUT FIELD: SIMULATING THE SPIN MODEL WITH MATRIX PRODUCT STATES

In the first part of this chapter we have seen that using the 1D spin model significantly reduces the size of the Hilbert space required to simulate the light propagation problem, but the dimension still grows exponentially with atom number. This growth can be avoided in the case where the input field is sufficiently weak that the Hilbert space can be truncated to a maximum number of total excitations likely to be found in the system [125], as we have seen in Sec. 2.4 where we applied the spin model formalism to the case of a Rydberg-EIT system under weak driving. In the more general case, where many-photon effects are important, the full Hilbert space may be treated numerically for around 10 to 20 atoms depending on the size of the single-atom Hilbert space dimension d. Going beyond this requires some reduction of the Hilbert space and here we choose to use matrix product states (MPS), which have been successfully used in condensed matter to model a wide variety of 1D interacting spin systems [130, 131] (see Appendix A.1 for a more detailed introduction).

The key idea behind MPS is to write the quantum state of the spin chain in a local representation where only a tractable number of basis states from the full Hilbert space is retained. In the case of time evolution, these basis states are updated dynamically in order to have optimum overlap with the true state wave function. In particular, the wave function of a many-body system $|\psi\rangle = \psi_{\sigma_1,\sigma_2,\ldots,\sigma_N}|\sigma_1,\sigma_2,\ldots,\sigma_N\rangle$ can be represented by

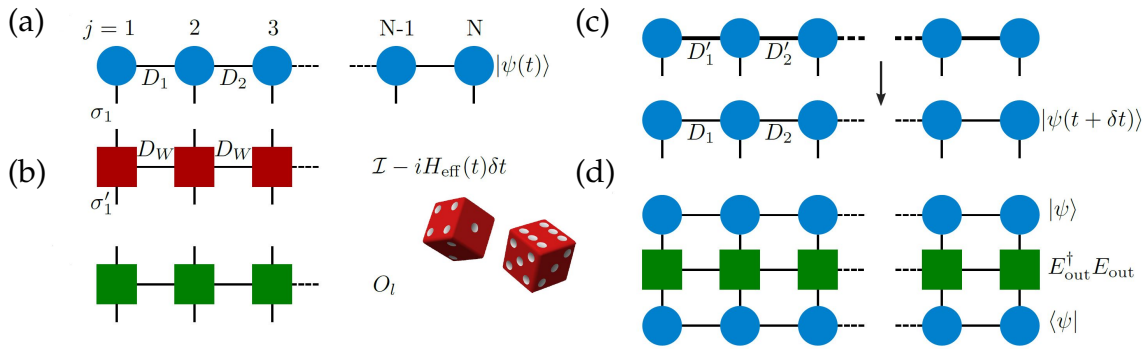

Figure 2.8: Schematic of MPS operations. (a) Deterministic time evolution of MPS. The initial state $|\psi(t)\rangle$ in MPS form is presented pictorially as a tensor network, where the circles represent the set of local matrices A^{σ_j} on each site j. The lines or bonds joining the circles represent the contraction of these local tensors to give the state $|\psi(t)\rangle$, where the bonds have dimension D_j. The open ended lines correspond to the local d-dimensional Hilbert space of the atoms σ_j. The deterministic evolution is then found by contracting these open connectors with those of the MPO representing $e^{-iH_{\text{eff}}\delta t} \approx 1 - iH_{\text{eff}}\delta t$, shown as a tensor network of red squares. (b) Quantum jumps. After each deterministic evolution a random number generator is used to decide whether quantum jumps should be applied to the wave function. This is achieved by applying the MPO corresponding to a quantum jump O_l, shown as a tensor network of green squares. (c) After the application of the time evolution or jump MPOs the resulting MPS has larger bond dimension, *e.g.*, $D_1' = D_W \times D_1$, and is compressed, typically back to the original bond dimension, although this can be increased if the compression produces a large error. (d) Measurement of observables. At any time we may measure an observable by sandwiching the corresponding MPO, here for example $E_{\text{out}}^\dagger E_{\text{out}}$, between the MPS representing $|\psi\rangle$ and $\langle\psi|$, so that the corresponding tensor contraction yields $\langle\psi| E_{\text{out}}^\dagger E_{\text{out}} |\psi\rangle$.

reshaping the N-dimensional tensor $\psi_{\sigma_1,\sigma_2,\ldots,\sigma_N}$ into a matrix product state of the form

$$|\psi\rangle_{\mathrm{MPS}} = \sum_{\sigma_1,\ldots,\sigma_N} A^{\sigma_1} A^{\sigma_2} \ldots A^{\sigma_N} |\sigma_1, \sigma_2, \ldots, \sigma_N\rangle , \qquad (2.30)$$

where σ_j represent the local d-dimensional Hilbert space of the atoms, *e.g.*, $\sigma_j \in \{|e\rangle, |g\rangle\}$ for two-level atoms. Each site j in the spin chain has a corresponding set of d matrices, A^{σ_j}, and by taking the product of these matrices for some combination of σ_j's we then recover the coefficient $\psi_{\sigma_1,\sigma_2,\ldots,\sigma_N}$. The matrices have dimensions $D_{j-1} \times D_j$ for the jth site ($D_0 = D_{N+1} = 1$), which are referred to as the bond dimensions of each matrix. We also define $D = \max_j D_j$ as the maximum bond dimension of the state $|\psi\rangle_{\mathrm{MPS}}$. This representation is completely general, and as such the bond dimensions grow exponentially in size for arbitrary quantum states. In certain circumstances, however, the bond dimension D needed to approximate a state well might grow more slowly with N due to limited entanglement entropy, which enables MPS to serve as an efficient representation.

For example, this forms the underlying reason for the efficiency of density-matrix renormalization group algorithms for computing ground states of 1D systems with short-range interactions [132]. A priori, for our system involving the dynamics of an open system with long-range interactions, we know of no previous work that makes definitive statements about the scaling of D. We can provide some intuitive arguments, however, that MPS should work well (at least without additional interactions added to the system). First, we note that although the dipole-dipole interaction term in Eq. (2.7) appears peculiar, being infinite-range and non-uniform, it conserves excitation number. For a single excitation, it simply encodes a (well-behaved) linear optical dispersion relation that propagates a pulse from one end of the atomic system to the other [125], and thus does not add entanglement to the system. While the spin nature in principle makes the atoms nonlinear, thus far in atomic ensemble experiments the strength of nonlinearity arising purely from atomic saturation remains very small at the level of single photons, and thus one can hypothesize that only a small portion of the Hilbert space is explored. Once extra interactions are added, at the moment the scaling of D must be investigated on a case-by-case basis. However, generically one expects that the system has a memory time corresponding roughly to the propagation time of a pulse through the length of the system. Thus, if the system is driven continuously, it should generally reach a steady state over this time and there will not be an indefinite growth of entanglement in time.

In our MPS treatment of the spin model we adopt a quantum jump approach to model the time dynamics of the master equation [133], which has been successfully applied to many-body dissipative systems [134, 135]. We write the master equation for our 1D spin model in the form $\dot{\rho} = -i(H_{\text{eff}}\rho - \rho H_{\text{eff}}^{\dagger}) + \sum_l O_l \rho O_l^{\dagger}$, where O_l are the "jump" operators associated with the dissipation resulting from emission into the waveguide and into free space, and H_{eff} is a non-Hermitian effective Hamiltonian. This division of the master equation into jump terms and an effective Hamiltonian H_{eff} is not unique and we attempt to do so here in a way that the jump operators have a physical significance. In particular, the emission of a photon into the foward going mode of the waveguide may interfere with the input light that is also travelling in the positive z direction (see Eq. (2.9)), an interference that would be present in real detection of photons output from the waveguide. This interference can be taken into account in our jump operator, and as such we take the forward going jump operator to be $O_+ = \mathcal{E}_{\text{in}}(t) - i\sqrt{\Gamma_{1D}/2}\sum_j e^{-ik_0 z_j}\sigma_j^{ge}$ (in contrast with $O_+ = \sqrt{\Gamma_{1D}/2}\sum_j e^{-ik_0 z_j}\sigma_j^{ge}$ as in Sec. 2.2.1). The backward going jump operator is simpler given the lack of input field in that mode, $O_- = \sqrt{\Gamma_{1D}/2}\sum_j e^{ik_0 z_j}\sigma_j^{ge}$. In addition, we have N local jump operators $O_j = \sqrt{\Gamma'}\sigma_j^{ge}$ corresponding to the free space decay, giving a set of possible jumps $O_l \in \{O_+, O_-, O_1, \ldots, O_N\}$.

With the jumps formulated in this way the effective Hamiltonian becomes

$$H_{\text{eff}} = H_{\text{at}} - i\frac{\Gamma_{1D}}{2}\sum_{j,l=1}^{N}\exp(ik_0|z_j - z_l|)\sigma_j^{eg}\sigma_l^{ge} - \sqrt{\frac{\Gamma_{1D}}{2}}\mathcal{E}_{\text{in}}(t)\sum_j e^{-ik_0 z_j}\sigma_j^{eg} - \frac{i}{2}|\mathcal{E}_{\text{in}}(t)|^2. \quad (2.31)$$

In general H_{at} can describe any additional atomic evolution; in the specific case of two level atoms coupled to a probe of frequency ω_p we can write, in the frame rotating with in the input frequency, $H_{\text{at}} = \sum_j(-\Delta - i\Gamma'/2)\sigma_j^{ee}$, where $\Delta = \omega_p - \omega_{eg}$.

The quantum jump approach uses the above decomposition of the master equation to restate the evolution of the density operator as a sum of pure state evolutions called trajectories [133], where the wave function evolution is divided into (a) deterministic evolution under H_{eff} and (b) stochastic quantum jumps made by applying jump operators O_l. Starting from a pure state $|\psi(t)\rangle$ at time t, the deterministic evolution over a time step δt gives $|\psi(t+\delta t)\rangle = e^{-iH_{\text{eff}}\delta t}|\psi(t)\rangle$. However, during this evolution the norm of the state decreases to $\delta p =$

$1 - \langle\psi(t)| e^{iH_{\text{eff}}^\dagger \delta t} e^{-iH_{\text{eff}}\delta t} |\psi(t)\rangle$, as the effect of the jump operators is neglected. The effect of these operators is instead accounted for stochastically, where after each deterministic evolution we generate a random number r between 0 and 1. If $r > \delta p$ the system remains in state $|\psi(t+\delta t)\rangle$. Otherwise, the state makes a random quantum jump to $|\psi(t+\delta t)\rangle = O_l |\psi(t)\rangle$ with probability $\delta p_l = \delta t \langle\psi(t)| O_l^\dagger O_l |\psi(t)\rangle$. The state is then normalized and the process repeats for the next time step and each sequence of evolutions gives a quantum trajectory. Any observable can be obtained by averaging its value over many trajectories. Furthermore, as we choose our quantum jumps to relate to physical processes, the distribution of the jumps can be thought of as corresponding to actual photon detection in an experiment. As an aside, we note that MPS-based techniques for evolution of density matrices have also been developed [136–139]. Whether and when such techniques out-perform quantum jump methods for our problem is likely a subtle question, which will be explored in more detail in future work.

There are then four essential manipulations of the MPS as illustrated in Fig. 2.8. We first describe how to implement (a) deterministic evolution over a small discrete time step δt and (b) stochastic quantum jumps that account for dissipation. Additional steps specific to MPS are (c) state compression, to constrain the growth of the MPS representation of the state in time, and (d) calculation of observables such as the output field given an MPS representation of a state.

(a) *Time evolution.* To evolve the state $|\psi(t)\rangle$ in time we need to apply the operator $e^{-iH_{\text{eff}}\delta t}$ to the MPS representation. This is achieved by applying a matrix product operator (MPO) to the state, where just as a state can be decomposed into an MPS, any operator W can be expressed in a local representation as

$$W = \sum_{\sigma_1', \ldots, \sigma_N', \sigma_1, \ldots, \sigma_N} W^{\sigma_1', \sigma_1} W^{\sigma_2', \sigma_2} \ldots W^{\sigma_N', \sigma_N} \times |\sigma_1', \sigma_2', \ldots, \sigma_N'\rangle \langle\sigma_1, \sigma_2, \ldots, \sigma_N| . \quad (2.32)$$

Here W^{σ_j', σ_j} are a set of matrices at site j, where the matrices now have two physical indices σ_j', σ_j due to W being an operator. An MPO may be "applied" to an MPS via a tensor contraction over the physical indices σ_j of the MPS and MPO, as shown in Fig. 2.8a. This generates a new MPS with higher bond dimension, as the bond dimension of the MPO, D_W, multiplies the bond dimension of the original MPS, and for the calculation to be tractable D_W must be small. Such a compact form is not known for the operator $e^{-iH_{\text{eff}}\delta t}$; however, the first order approximation $e^{-iH_{\text{eff}}t} = I - iH_{\text{eff}}\delta t$ has a compact MPO form

if H_{eff} does. This is the case for the 1D spin model where the bond dimension is $D_W = 4$. Indeed we have

$$W_j = \begin{pmatrix} I_j & -\frac{i\lambda\Gamma_{1D}}{2}\,\sigma_j^{eg} & -\frac{i\lambda\Gamma_{1D}}{2}\,\sigma_j^{ge} & H_j^{\text{loc}} \\ 0 & \lambda\, I_j & 0 & \sigma_j^{ge} \\ 0 & 0 & \lambda I_j & \sigma_j^{eg} \\ 0 & 0 & 0 & I_j \end{pmatrix}, \tag{2.33}$$

for $1 < j < N$, and

$$W_1 = \begin{pmatrix} I_1 & -\frac{i\lambda\Gamma_{1D}}{2}\,\sigma_1^{eg} & -\frac{i\lambda\Gamma_{1D}}{2}\,\sigma_1^{ge} & H_1^{\text{loc}} \end{pmatrix}, \tag{2.34}$$

$$W_N = \begin{pmatrix} H_N^{\text{loc}} & \sigma_N^{ge} & \sigma_N^{eg} & I_N \end{pmatrix}_T, \tag{2.35}$$

where $\lambda = e^{ik_0 d}$, I_j is the spin identity operator for atom j, and H^{loc} contains all the local terms in H_{eff}. Using a small time step δt we can then advance the wave function in time.

(b) *Quantum jumps.* After evolving a time δt, the state is either kept and renormalized, or a jump is applied. To apply the quantum jump formalism we then just require an MPO form of the jump operators that can be applied to the MPS at each time step, see Fig. 2.8b. The jump operators of the 1D spin model can be written in compact MPO form, where the loss into free space is a local matrix operation, and loss into the waveguide requires an MPO of bond dimension $D_W = 2$:

$$Z_j = \begin{pmatrix} I_j & -i\sqrt{\Gamma_{1D}/2}\, e^{-ik_0 z_j}\, \sigma_j^{ge} \\ 0 & I_j \end{pmatrix}, \tag{2.36}$$

for $1 < j < N$, and

$$Z_1 = \begin{pmatrix} I_1 & -i\sqrt{\Gamma_{1D}/2}\, e^{-ik_0 z_1}\, \sigma_1^{ge} + \mathcal{E}(t) I_1 \end{pmatrix}, \tag{2.37}$$

$$Z_N = \begin{pmatrix} -i\sqrt{\Gamma_{1D}/2}\, e^{-ik_0 z_N}\, \sigma_N^{ge} & I_N \end{pmatrix}^T. \tag{2.38}$$

The MPO of O_- is analogous, but without the external field term in Z_1 and with k_0 replaced by $-k_0$.

(c) *State compression.* After applying the time evolution operator or jump operators the size of the MPS increases as the bond dimension of the operator multiplies the bond dimension of the original state. Over time this would lead to exponential growth in the MPS size if not constrained. This increase in bond dimension can correspond to the true build up of entanglement, but may also correspond to the new state being

expressed inefficiently in the MPS form. In the second case, a more efficient representation can be found and the bond dimension compressed to a smaller value, as in Fig. 2.8c. This can be done using singular value decompositions (SVD) to find low rank approximations of the matrices A^{σ_j} in the MPS representation, or by variationally exploring the space of MPS states with a fixed bond dimension that are closest to the original state [130, 131]. The validity of such a compression can be evaluated by checking how strongly the parts of the state discarded in the compression contribute to the description. This can be calculated easily using the SVD compression algorithm. We denote by $\lambda_{t,j,l}$ the set of singular values at bond site j and time t, with $1 \leqslant l \leqslant D'$ (with the singular values ordered to monotonically decrease with increasing l), then we may reduce the bond dimension by only keeping the singular values with $l \leqslant D$. One measure of this compression error is the norm of the difference of the original state and the compressed state $\epsilon_t = \| \, |\psi(t)\rangle_D - |\psi(t)\rangle_{D'} \, \|$, which can be expressed as $\epsilon_t = 1 - \prod_{j=1}^{N-1}(1-\epsilon_{t,j})$ with $\epsilon_{t,j} = \sum_{l>D} \lambda_{t,j,l}^2$. The error accumulated during the whole time evolution is $\epsilon_T = 1 - \prod_t (1-\epsilon_t)$. Since all the terms are small one can approximate the products with sums and obtain

$$\epsilon_T \approx \sum_{t=0}^{T_f} \sum_{j=1}^{N-1} \sum_{l>D} \lambda_{t,j,l}^2. \tag{2.39}$$

ϵ_T is a figure of merit for the quality of the time evolution. By monitoring this quantity the bond dimension in the compression can be adjusted so that the error remains small.

(d) *Calculating observables.* At any point in time observables such as the spin populations or output field may be calculated for a particular quantum trajectory by applying the appropriate operator associated with that observable in MPO form to the state. For example, to find the output intensity, $\langle\psi(t)| \, E_{out}^\dagger(t) E_{out}(t) \, |\psi(t)\rangle$, one can express the individual elements as matrix product states or operators. The intensity for that trajectory can then be evaluated through a tensor contraction, as shown in Fig. 2.8d. This intensity is then averaged over all the quantum trajectories to find the expectation value $I_{out}(t) = \langle E_{out}^\dagger(t) E_{out}(t)\rangle$. Multi-time correlation functions such as $I_{out}^{(2)}(t, t+\tau) = \langle E_{out}^\dagger(t) E_{out}^\dagger(t+\tau) E_{out}(t+\tau) E_{out}(t)\rangle$ can also be found. This is done by propagating the state in time until time t and then applying the operator E_{out} to the state. The state is evolved a further time τ and the operator applied again. The norm of the resulting states are then averaged over many such evolutions to find the two-time correlation.

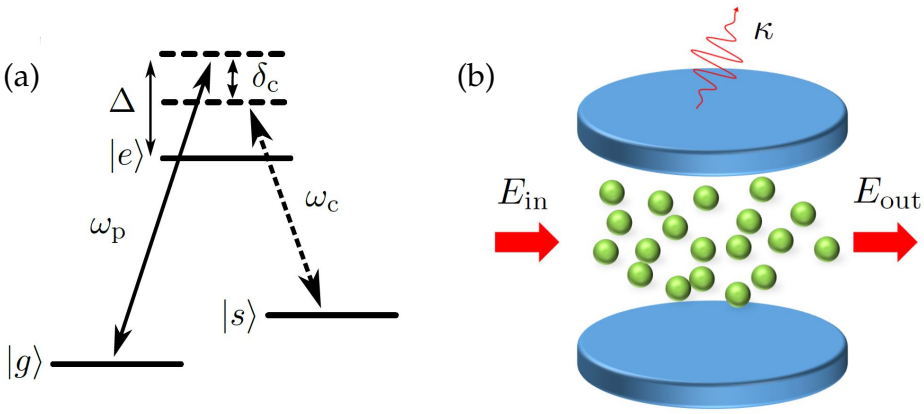

Figure 2.9: (a) VIT three-level scheme, where the transition $|s\rangle - |e\rangle$ is coupled to a cavity field with frequency ω_c, allowing for transparent propagation of probe photons (ω_p). (b) In VIT, an atomic ensemble is trapped inside an optical cavity where the atoms couple both to the probe field E_{in} and to a cavity mode which is initially in its vacuum state. Photons in the cavity have an associated decay rate κ from transmission through the mirrors.

2.6 VACUUM INDUCED TRANSPARENCY

The model introduced above gives a powerful and flexible algorithm for simulating the interaction of light with atomic ensembles in the multi-photon limit. To demonstrate the utility of this approach we now investigate the phenomenon of vacuum induced transparency (VIT) [58]. This example also serves to benchmark our method, as exact solutions for non-trivial multiphoton behavior are not available, while in the case of VIT at least the qualitative nature of the system dynamics is understood.

VIT is closely related to the effect of EIT, presented in Sec. 2.6, which occurs in three-level atomic media. The only difference is that the control field is replaced by strong coupling of the atoms to a resonant cavity mode as shown in Fig. 2.9a,b [58, 140], which is described by the Hamiltonian $H_{cav} = g\sum_j(\sigma_j^{es}a + \text{h.c.})/2$ in the case of uniform coupling g to a cavity mode with annihilation operator a. Here even when the cavity is empty the atomic medium can become transparent as vacuum Rabi oscillations transfer population from state $|e\rangle$ to $|s\rangle$ [59]. The propagation of light in the system then takes on the nature of the non-linear coupling of the atoms to the cavity. Specifically, the formation of a spin wave from n probe photons is accompanied by the excitation of the same number of cavity photons, which produce an effective control field strength of $\sqrt{n}g$. Since in EIT the group velocity of the light is determined by the con-

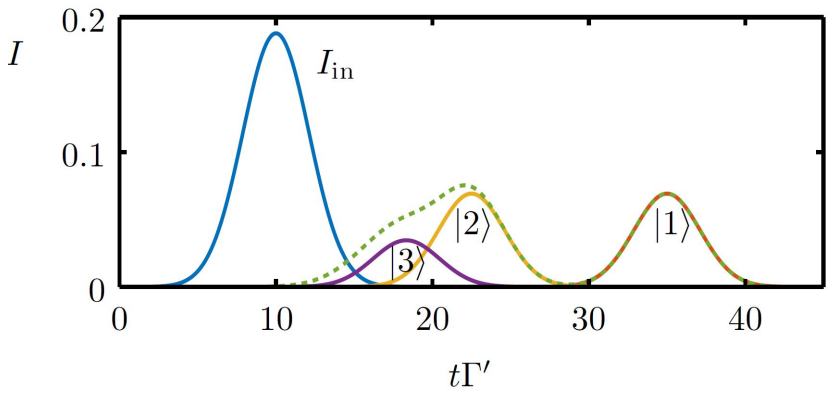

Figure 2.10: Idealized time-dependent transmission of a coherent pulse with average number of photons equal to one through a VIT medium. In the case where all loss mechanisms are ignored, as well as the effect of pulse distortion on entry and exit from the atomic ensemble, the individual Fock number state components $|n\rangle$ of the input pulse (blue) propagate through the medium with group velocity $v_n \propto n$. This leads to separation of the one- (red), two- (yellow) and three-photon (violet) components of the output field, and a total output intensity shown by the green dashed line. We have taken $v_1 = 4d\Gamma'$ and the medium has a length $L = 100d$.

trol field, where $v_g \propto |\Omega|^2$, the group velocity in VIT becomes number dependent $v_n \propto n$ [141, 142]. Fock states $|n\rangle$ input into the system are then expected to propagate at v_n.

On the other hand, a coherent state $|\alpha\rangle$ that has average number of photons $|\alpha|^2$ is a superposition of Fock states, where n photons are present with probability $e^{-|\alpha|^2}|\alpha|^{2n}/n!$. Input into the VIT medium, these components are then expected to spatially separate due to their different propagation velocities, given sufficient optical depth. The output intensity can then be calculated naively by simply delaying the input Fock components by a time $\tau_n = L/v_n$, where L is the length of the atomic medium. The output intensity in time resulting from such a toy model is shown in Fig. 2.10, for a coherent state input pulse with average number $\langle n_{\text{pulse}}\rangle = 1$. We have taken the system length to be $L = 100d$ (d being the distance between the atoms, equal to $3\lambda/4$) and the single photon velocity $v_1 = 4d\Gamma'$, which results for example from taking $g = 4\Gamma'$ and $\Gamma_{1D} = 2\Gamma'$ in which case the system's optical depth is $OD = 400$. We note that the experimental conditions needed to observe photon number separation in VIT are difficult to achieve [59], and thus our parameters are chosen to observe the desired effect, rather than correspond to a given experiment. Such an effect would be interesting in a

number of contexts; for example, it would allow for photon number resolving detection simply through timing.

A plot similar to Fig. 2.10 was given in the original theory of VIT [141], as at that time it was unknown how to calculate observables in the presence of losses and spatio-temporal effects, such as occurring from pulse entry and exit from the atomic medium. More recently, VIT has also been studied numerically in the weak-field limit using the space discretization technique [142]. In the weak field limit, only the single photon manifold contributes to the output intensity and the higher number components are only visible in higher order correlation functions like $g^{(2)}$. This also means that quantum jumps have a negligible effect on the system dynamics, and they were neglected in the calculations. In more general circumstances, using MPS simulations, we will show that the effects of quantum jumps and pulse distortion can have a significant effect on the output field.

For concreteness, we take input pulses with central frequency ω_p and Gaussian envelope $\mathcal{E}_{in}(t) = \alpha(\pi\sigma_t^2/2)^{-1/4}\exp(-(t-T)^2/\sigma_t^2))$, which have an average photon number of $\langle n_{pulse}\rangle = |\alpha|^2 \sim 1$. The average photon number chosen is not due to any intrinsic limitation coming from the MPS method itself, but rather because in VIT the spatial separation is largest for the Fock components with low photon number (see Fig. 2.10) and with $|\alpha|^2 = 1$ the single photon and two photon components of the coherent state give an equal contribution to intensity emphasizing this effect. In this case, number states with three or more photons make up 8% of the input state and constitute 26% of the input intensity due to their high photon number.

To treat VIT, we include in the spin model formalism the atomic part H_{at} of the total effective Hamiltonian

$$H_{at} = -\sum_j \left(\Delta + i\frac{\Gamma'}{2}\right)\sigma_j^{ee} - \left(\delta_c + i\frac{\kappa}{2}\right)a^\dagger a + \frac{g}{2}\sum_j (\sigma_j^{es} a + h.c). \quad (2.40)$$

Here $\Delta = \omega_p - \omega_{eg}$ is the detuning of the probe light from the $|e\rangle$-$|g\rangle$ transition frequency, $\delta_c = \omega_p - \omega_c - \omega_{sg}$ is the VIT two-photon detuning and κ is the decay rate of the cavity mode. The

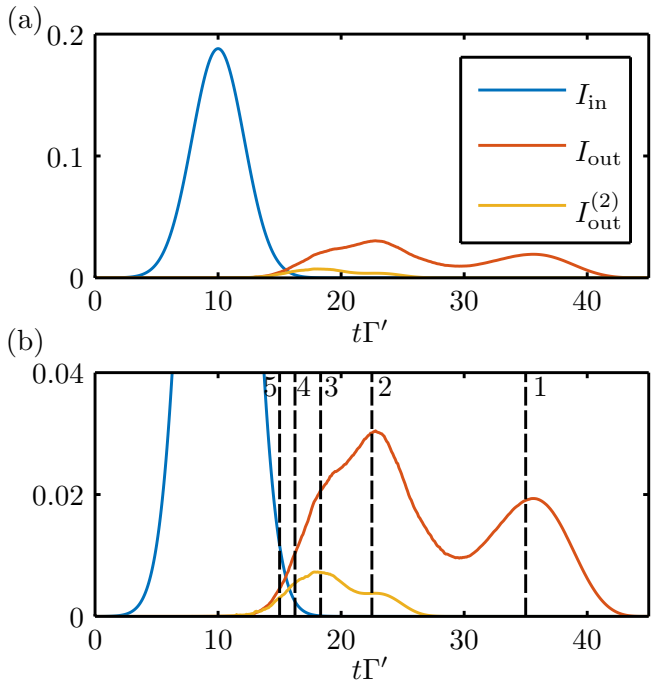

Figure 2.11: (a) Pulse propagation in a VIT medium with optical depth OD = 400, simulated using N = 100 atoms coupled to a 1D-waveguide, and averaged over 20000 quantum trajectories. Input of a coherent pulse with $|\alpha|^2 = 1$ (blue) results in an output intensity $I_{out}(t)$ (red) with two main peaks. Also plotted is the second-order correlation function $I^{(2)}_{out}(t,t)$ (yellow). (b) Zoom of the plot above, with dashed lines showing the expected positions of pulses delayed by τ_n, for $n = 1,\ldots,5$. Simulation parameters are $\Gamma_{1D} = 2\Gamma'$, $\Delta = \delta_c = 0$, $g = 4\Gamma'$, $\kappa = 0.03\Gamma'$, $\sigma_t = 3/\Gamma'$ and $T = 10/\Gamma'$. We chose $D = 50$ and $\delta t = 0.01/\Gamma'$ where convergence was observed for all observables of interest.

MPO of the effective Hamiltonian for VIT is a straightforward extension of (2.33):

$$W_j^{\mathrm{VIT}} = \begin{pmatrix} \dots & \dots & \dots & \frac{g}{2}\sigma_j^{es} & \frac{g}{2}\sigma_j^{se} & \dots \\ \dots & \dots & \dots & 0 & 0 & \dots \\ \dots & \dots & \dots & 0 & 0 & \dots \\ 0 & 0 & 0 & I_j & 0 & 0 \\ 0 & 0 & 0 & 0 & I_j & 0 \\ \dots & \dots & \dots & 0 & 0 & \dots \end{pmatrix}, \tag{2.41}$$

for $1 < j \leqslant N$, where the dots stand for the elements given in Eq. (2.33) and

$$W_{N+1}^{\mathrm{VIT}} = \begin{pmatrix} H^{\mathrm{loc,cav}} & 0 & 0 & a & a^\dagger & I^{\mathrm{cav}} \end{pmatrix}^T. \tag{2.42}$$

In what follows we assume both the probe and cavity are resonant with their respective transitions, so that $\Delta = \delta_c = 0$. Dissipation via the various loss channels is then included through quantum jump operators. The jump operator corresponding to cavity decay is $O_c = \sqrt{\kappa}a$ and we assume that the atomic excited state can decay via free-space spontaneous emission into either state $|g\rangle$ or $|s\rangle$ (taking these decay rates to be equal for simplicity), leading to 2N jump operators $O_{j,ge} = \sqrt{\Gamma'/2}\sigma_j^{ge}$ and $O_{j,se} = \sqrt{\Gamma'/2}\sigma_j^{se}$. The cavity mode is represented in our MPS treatment by an additional site in our spin chain, which can support up to n_c bosonic excitations. In the simulations we present here we have taken $n_c = 10$ and observe no difference in observables if n_c is increased.

In Fig. 2.11a,b we show the time-dependent output pulse intensity $I_{\mathrm{out}}(t) = \langle E_{\mathrm{out}}^\dagger(t)E_{\mathrm{out}}(t)\rangle$ calculated from an MPS simulation of 100 atoms and an input pulse with $|\alpha|^2 = 1$. We also show the zero-delay second order correlation function $I_{\mathrm{out}}^{(2)}(t,t) = \langle E_{\mathrm{out}}^\dagger(t)E_{\mathrm{out}}^\dagger(t)E_{\mathrm{out}}(t)E_{\mathrm{out}}(t)\rangle$. In the output intensity two main peaks are observed, where the first peak in time ($t\Gamma' \sim 23$) is due to photon number components with two or more photons, while the last peak ($t\Gamma' \sim 36$) is associated with the slow propagation and exit of the single-photon component. That the most delayed part contains only single photons can be seen by looking at the second order correlation function which is only nonzero in the first part of the pulse. In Fig. 2.11b we see good agreement between the features of the numerical pulse shape and the expected group velocity for each part of the pulse (compare with Fig. 2.10), where the vertical black dashed lines represent the expected times for the peaks of the Fock state components, that is, with delays τ_n.

Compared with the ideal picture in Fig. 2.10, where a clean separation is seen between one and two photons, one can see that the full simulation produces a much larger intensity between the one- and two-photon peaks. We now show how the trajectories from the MPS simulations can be further filtered and analyzed, to gain insight about the underlying physics. In particular, we find that quantum jumps play a key role in blurring the separation between the different number components in the output, even for the very good system parameters that we have chosen (OD $= 400$, $g/\kappa \sim 130$). An intuitive picture of how the blurring occurs can be gained by considering two photons that enter the medium, and initially propagate at a velocity $v_2 = 2v_1$. During evolution, this state may decay via spontaneous emission into free space and leave behind a single photon propagating in the medium, at which point the group velocity is slowed to v_1. This change in group velocity can happen at any point in the system and leads to single photons that arrive at the output earlier than expected if just a single-photon Fock state was input into the system, destroying the perfect separation of the single photon output from the two photon component.

We can quantify this behavior by analyzing the quantum jumps that happen in our simulations, where due to the choice of physical jump operators discussed above, the total number of jumps in a given trajectory corresponds to the number of photons emitted from the system. Furthermore, the type of jumps (and thus the emission channel) can be explicitly tracked, between free-space loss, cavity loss, or detection in the waveguide output. In Fig. 2.12a, we create a histogram of jumps corresponding to output into the waveguide versus time for the 20000 trajectories used to produce Fig. 2.11. The count of the jumps in the output channel provides an alternative way (compare to Fig. 2.11) to calculate the intensity, as would be done in an experiment where detector counts are averaged over many identical realizations. In Fig. 2.12a, the vertical axis is re-scaled in units of intensity rather than total number of events, to yield a more direct comparison with the previously calculated output intensity (black dotted line).

Furthermore, we can classify the jumps according to whether they come from trajectories where 1, 2 or 3+ photons are emitted into the waveguide (as indicated by the different bar colors in Fig. 2.12a). As we see in the plot, the higher the number detected in the waveguide, the earlier in time the jumps happen, in agreement with the the simple theoretical model and with the calculations of $I_{out}(t)$ and $I^{(2)}_{out}(t,t)$, discussed above. We can also select only the trajectories where a single photon is de-

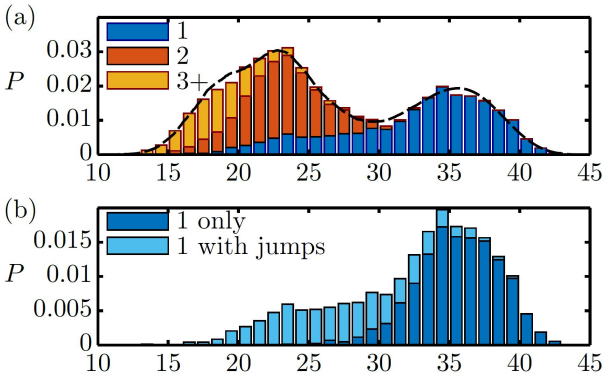

Figure 2.12: (a) Stacked bar graph of quantum jumps into the output channel over the 20000 quantum trajectories used in Fig. 2.11. The height of each bar is the proportion P of trajectories that have an output channel jump occurring in the time bin defined by the bar's width. The bars are then divided into three categories by classifying each jump according to how many jumps into the output channel occur for a particular trajectory (1, 2, or 3 or more). Jumps from trajectories where there are a higher number of photons emitted into the output channel are seen to occur earlier. For comparison the dashed black line shows the output intensity from Fig. 2.11. (b) Stacked bar graph for quantum jumps from trajectories where only a single photon is detected in the output of the waveguide. These jumps are then divided into jumps that are not accompanied by any other jump into other channels, and those that are. We see that the tail of photons detected earlier are due to trajectories where 2 or more photons entered the medium but all but one were lost into other channels.

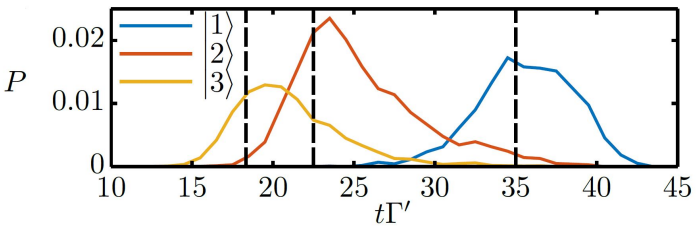

Figure 2.13: Post-selection of trajectories to find evolution for Fock state input. By selecting only trajectories where there were a total of 1 (blue), 2 (red), or 3 (yellow) jumps into any channel we can reconstruct the intensity output for the corresponding input Fock state.

tected at the waveguide output, and further separate those trajectories into two distinct cases: (i) when that is the only jump event (indicating a single photon was input and successfully propagated through the system), and (ii) where a multi-photon state was input, and all but one photon decayed into other channels. The histogram according to this classification in time is shown in Fig. 2.12b, where we see that the tail of faster arriving single photons, seen to the left of the main peak, results from the decay of number states with two of more photons, and the resulting mixing of propagation velocities.

Alternatively, we can use the jump statistics from a coherent state input to identify the intensity resulting from a Fock state input. Since the VIT system does not support any long lived excitations (compared with the simulated time scale), the total number of photon jumps (into any channel) out of the system for any one trajectory is equal to the number of the photons that entered the system for that trajectory. By post-selection on the total number of jumps we can then find the intensity that results from a Fock state input as shown in Fig. 2.13. Here we see the same effect of jumps as noted above but observed in a different way. In particular, while we categorized the trajectories in Fig. 2.12a,b by the number of photons that survive and are output, in Fig. 2.13 we classify them by the number that are input. For Fock state inputs of two or more photons, the output intensities show tails of longer than expected delay times, again as a result of photon loss and the mixing of propagation speeds.

These longer than expected delay times are not only due to quantum jumps however, they can also result from distortion of the multi-photon wavepacket as it enters the medium [142]. This distortion happens as the input pulse crosses the boundary of the atomic ensemble, as we illustrate for a two-photon wave function in Fig. 2.14a. There, the initial Gaussian distribution of the photon positions z_1 and z_2 is shown as a circle. The two-

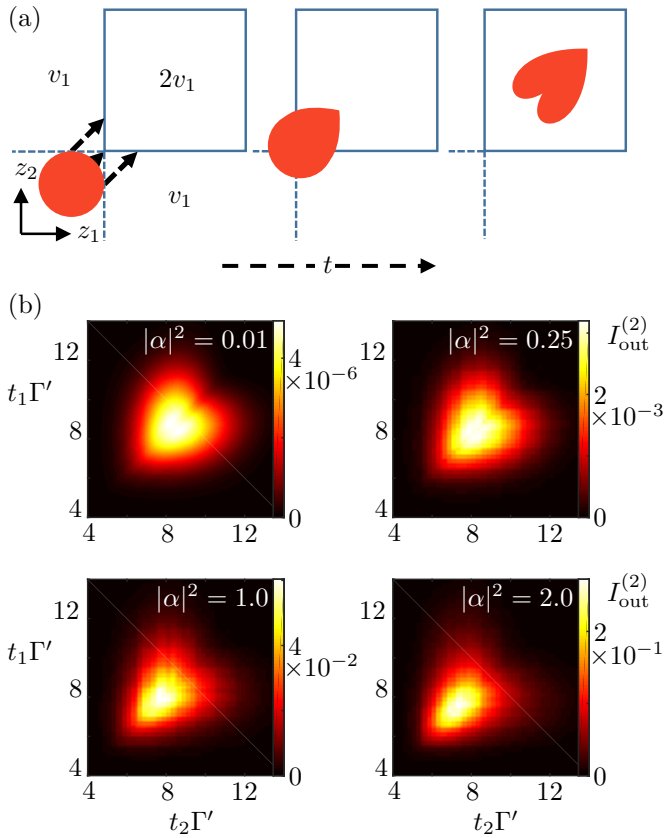

Figure 2.14: (a) Illustration of distortion as a two-photon wavefunction $\psi(z_1, z_2)$ enters the atomic medium. (b) Two-time correlation function for the output field, $I^{(2)}_{\text{out}}(t_1, t_2)$, of the VIT system, after excitation with a coherent Gaussian input pulse for various average input photon number, $|\alpha|^2 = 0.01$, 0.25, 1.0 and 2.0. The system parameters were for an optical depth of OD = 60, with N = 30, $\Gamma_{1D} = \Gamma'$, $\Delta = \delta_c = 0$, $g = 4\Gamma'$, $\kappa = 0.03\Gamma'$, $\sigma_t = 4/\Gamma'$ and $T = 6/\Gamma'$. We chose a bond dimension of D = 30 and a time step of $\delta t = 0.01/\Gamma'$ where convergence was observed for all observables of interest.

dimensional space of the photon pair is divided into regions where only one photon is inside the medium and has group velocity v_1, indicated by the dashed lines, and when both photons are inside the medium having velocity $v_2 = 2v_1$, the square box. Photon pairs with greater separation spend more time in the regions where only one photon is inside the medium, delaying them compared to pairs with $z_1 = z_2$, leading to a characteristic heart shaped pattern. In Fig. 2.14b we show how this behavior can be observed in the two time correlation measurement of the output photons for an input coherent pulse at low input photon number. At weak input field the two-time correlation function is purely due to the two photon component and shows a clean heart shape. As the number of input photons increases, higher photon number components contribute, which travel faster through the medium distorting the pattern and pulling it forward in time.

2.7 CONCLUSIONS

In summary, in this chapter we have first introduced a powerful theoretical model to describe light propagation in atomic ensembles by means of purely atomic one-dimensional effective Hamiltonian, and then we have presented a technique to numerically simulate this effective model, which is based on the powerful toolbox of matrix product states. This technique appears quite versatile, and adaptable to many cases of theoretical and experimental interest (*e.g.*, with regard to level structure, types of interactions, additional degrees of freedom, etc.). Similar to the important role that DMRG and MPS played in one-dimensional condensed matter systems, we envision that results gained from our numerical techniques could be used to push forward the development of effective theories of strongly interacting systems of light [57, 112–114, 125, 143, 144], and conversely that such analytical work could be used to improve numerical algorithms.

Beyond that, it would be also interesting to investigate further why MPS apparently works well in the context of our open, long-range interacting system, and under what conditions MPS might fail. This could help to provide insight into the growth of entanglement, which naively seems like a potentially useful resource, but which has not been explored for such systems to our knowledge. Finally, the ability to formally map atom-light interactions to a quantum spin model appears rather intriguing in general, and it would be interesting to explore whether other techniques for solving spin systems could be applied here as well.

3

DESIGNING EXOTIC MANY-BODY STATES OF SPIN AND MOTION

3.1 INTRODUCTION

In Sec. 1.2.2 we have briefly introduced photonic crystal waveguides (PCW) [37], periodic dielectric structures in which the propagation of light can differ significantly from uniform media. An important feature of photonic crystals is the appearance of photonic band gaps, where strong interference in scattering from the periodic dielectric yields a complete absence of propagating modes within some bandwidth. We have also seen that an excited atom whose transition frequency resides in the gap would not be able to spontaneously emit, but that an atom-photon bound state can form, in which the atom becomes dressed by a localized photonic cloud [40, 45–48]. This photonic cloud can mediate exchange of excitations between atoms, realizing long-range atom-atom interactions. Furthermore, the tight spatial confinement associated with the band gap photon yields large dispersive forces on proximal atoms that depend on the atomic internal "spin" states, thus realizing a coupling between the internal degrees of freedom of the atoms and their position in space.

In condensed matter rich phenomena arise when quantum spin systems couple to phonons or orbital degrees of freedom of the underlying crystal lattice. Perhaps the most famous example is the spin-Peierls model [68–71], wherein the spin interaction leads to a lattice instability resulting in a ground state of singlet pairs and a bond-ordered density wave. Motivated by this emergence of new physics, we investigate if the interplay between internal and motional degrees of freedom that is realized in the atoms-PCW interface can realize exotic many-body states, where the spin-dependent forces dictate the properties of the emergent spatial order. In such a case we would be in presence of a novel "quantum crystal" that has not existed before, in which the emergent spatial patterns and spin properties are intricately locked together, and where driving one would automatically affect the properties of the other.

In this chapter we first review more in detail the physics of atoms coupled to PCW's, using a generalization of the formalism introduced in Chapter 2 for the case of atoms coupled to a 1D waveguide. Then we focus our investigation on

one of the many models that can be realized with the atoms-PCW platform. In the case considered atoms are trapped in a weak one-dimensional external potential, and a short-range spin-dependent force can be made sufficiently strong to exceed the external potential. To understand the emergent orders of this system we begin by treating the motion of the atoms classically and their spins quantum mechanically. We find an effect reminiscent of the spin-Peierls transition, in which the atoms spatially dimerize and realize a high degree of entanglement within each dimer. We then proceed to a fully quantum model. Using density matrix renormalization group (DMRG), we find a rich variety of quantum phases beyond the spin-Peierls state, such as a state where spin and phonon excitations form composite particles, phonon-induced Néel ordering, and spatial trimers associated with magnetization plateaus.

While a specific model is studied, the results obtained suggest that spin-orbital coupling can be a dominant phenomenon in all hybrid systems of atoms and photonic crystals. Similar considerations could also apply to a number of other atomic systems where spatially-dependent spin interactions can be realized, including polar molecules [145–147], Rydberg atoms [148], ion chains [50, 51, 149], and atoms in high-finesse cavities [150].

3.2 ATOM-ATOM INTERACTIONS IN DIELECTRIC SURROUNDINGS

In Sec. 2.2.1 we have derived an effective theory for atoms interacting through the guided modes of a 1D waveguide to which they are coupled. Here, we present the extension of that formalism to the case of a generic atomic ensemble in a dielectric surrounding, which we will later apply to the case of an ensemble of atoms interacting via the process of photon exchange near a photonic crystal. We generally begin by considering an ensemble of two-level atoms with ground state $|g\rangle$ and excited state $|e\rangle$, with corresponding transition frequency ω_{eg}. The atoms can be in the vicinity of any linear, isotropic dielectric materials, characterized by dimensionless electric permittivity $\epsilon(\mathbf{r}, \omega)$. Here $\mathbf{r}$ denotes the spatial coordinate, and ϵ in general is allowed to be dependent on frequency ω and absorbing (*i.e.*, have an imaginary component). A quantum theory of atom-light interactions in the presence of such dielectric media has been pioneered in a number of works by Welsch and co-workers [151, 152]. Here we will not go through the derivation again, but will present the main results and qualitatively argue why the results are physically reasonable.

Intuitively, two-level atoms can interact via the electromagnetic field through the exchange of photons. Microscopically, one atom would be able to de-excite by emitting a photon (as characterized by the atomic lowering operator $\sigma^{ge} \equiv |g\rangle\langle e|$ and another atom would be able to absorb the photon and become excited (as characterized by the raising operator $\sigma^{eg} \equiv |e\rangle\langle g|$). By integrating out the field, one obtains an effective atom-atom interaction Hamiltonian of the form [152]

$$H_{dd} = -\sum_{j,l=1}^{N} J_{jl}\, \sigma_j^{eg}\sigma_l^{ge}, \tag{3.1}$$

where $J_{jl} = \mu_0\omega_{eg}^2\, \mathbf{d}^* \cdot \mathrm{Re}\{\mathbf{G}(\mathbf{r}_j, \mathbf{r}_l, \omega_{eg})\} \cdot \mathbf{d}$. Here $\mathbf{d}$ is the dipole matrix element of the transition, and $\mathbf{G}$ is the classical electromagnetic Green's function, defined as the solution to the wave equation with a point source,

$$\left[(\nabla \times \nabla \times) - \omega^2 \epsilon(\mathbf{r}, \omega)/c^2\right] \mathbf{G}(\mathbf{r}, \mathbf{r}', \omega) = \delta(\mathbf{r} - \mathbf{r}') \otimes \mathrm{I}. \tag{3.2}$$

The Green's function $\mathbf{G}$ is in fact a 3×3 matrix, whose elements G_{ab} have the meaning of being the field at r projected along a ($a = x, y, z$), due to an oscillating source of frequency ω at $\mathbf{r}'$, whose dipole moment is oriented along b. For simplicity, from here forward we will not explicitly indicate the tensor nature of $\mathbf{G}$, *e.g.*, by considering a transition that is linearly polarized along x, $\mathbf{d} = \wp\hat{x}$, such that only the G_{xx} component is relevant (and thus dropping the subscripts). Physically, although a two-level system produces non-classical light, classical and quantum fields *propagate* the same way, and thus the coherent interaction strength between the atoms can be characterized by the classical Green's function. Moreover, the dependence of H_{dd} on the real part of G has a classical analogy, in that a field in phase with an oscillating dipole stores time-averaged energy.

Likewise, an ensemble of atoms should experience dissipation in the form of spontaneous emission. Eliminating the fields results in a corresponding master equation for the density matrix ρ of the atoms alone, with Lindblad operator given by

$$\mathcal{L}_{dd}[\rho] = \sum_{j,l=1}^{N} \frac{\Gamma_{jl}}{2}(2\sigma_j^{ge}\rho\sigma_l^{eg} - \sigma_j^{eg}\sigma_l^{ge}\rho - \rho\sigma_j^{eg}\sigma_l^{ge}), \tag{3.3}$$

where $\Gamma_{jl} = 2\mu_0\omega_{eg}^2\mathbf{d}^* \cdot \mathrm{Im}\{\mathbf{G}(\mathbf{r}_j, \mathbf{r}_l, \omega_{eg})\} \cdot \mathbf{d}$. This equation also has a classical analogy, in that the field out of phase with an oscillating dipole performs time-averaged work. As a simple limit, one can consider the case of a single atom in vacuum, for which $\epsilon(\mathbf{r}, \omega) = 1$. The corresponding Green's function G_0 has the property that $\mathrm{Im}\, G(\mathbf{r}, \mathbf{r}, \omega_{eg}) = \omega_{eg}/(6\pi c)$. Substituting

this into $L[\rho]$ one finds that $L[\rho] = \Gamma_0(2\sigma^{ge}\rho\sigma^{eg} - \sigma^{ee}\rho - \rho\sigma^{ee})$, where $\Gamma_0 = \omega_{eg}^3\wp^2/(3\pi\epsilon_0\hbar c^3)$ correctly identifies as the single-atom free-space spontaneous emission rate.

Eqs. (3.1) and (3.3) are quite general and completely dictate the atomic dynamics given knowledge of the Green's function G. For an actual photonic crystal structure such as the "alligator" PCW used in experiments [42, 44], the Green's function G can be numerically calculated using standard electromagnetic simulation software, as has been done in Ref. [46]. G contains information about fundamental dissipation rates such as atomic spontaneous emission into free space, and in principle numerical simulations could also incorporate any kind of imperfections stemming from structure disorder (that can be captured in some imperfect dielectric profile $\epsilon(\mathbf{r}, \omega)$) to infer its effect on atom-atom interactions. However, in Ref. [46] it was shown that the predictions from numerical simulations of G for a realistic photonic crystal waveguide agree quantitatively with a simpler theoretical model of atom-atom interactions at a band edge. We thus present the simple model below, which provides excellent intuition about the strengths of the coherent interactions and dissipation, and the effect of certain imperfections.

3.3 MODEL OF ATOM-ATOM INTERACTIONS AT A PCW BAND EDGE

In this section we present the model for the interaction between atoms mediated by guided photons of a PCW, whose effects at the many-body level will be investigated in the remaining of this chapter.

3.3.1 *Band-gap mediated interactions*

We consider an idealized 1D model of atoms interacting via a band edge of a photonic crystal structure. The two-level atoms are assumed to predominantly couple to a single band, whose dispersion relation can be expanded quadratically around the band edge, $\omega(q) = \omega_b(1 - \alpha(q - k)^2/k^2)$ (see Fig. 3.1a). Here, ω_b is the frequency at the band edge, q is the Bloch wavevector of the guided mode, $k = \pi/a$ is the edge of the Brillouin zone determined by the structure periodicity a, and $\alpha > 0$ is a dimensionless parameter characterizing the band curvature. The atomic transition frequency $\omega_{eg} > \omega_b$ is assumed to lie within the band gap and couple to an upper band edge, as shown in Fig. 3.1a. The conclusions below would also hold if the atoms were coupled to a lower band edge, but with a change in the sign of the resulting atom-atom interaction.

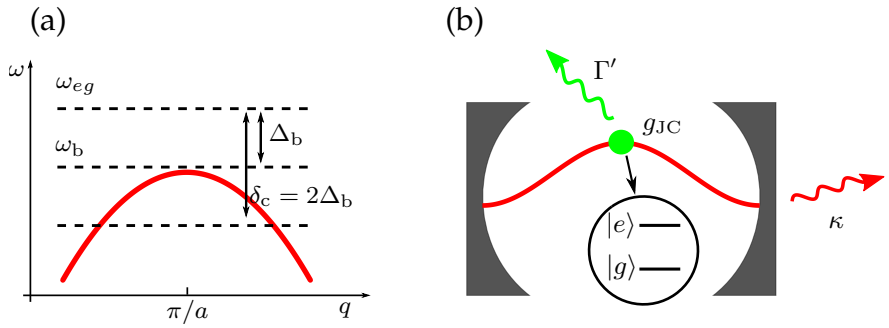

Figure 3.1: (a) Energy level structure for a two-level atom coupled to a photonic crystal. The transition frequency ω_{eg} has a detuning Δ_b above the band-edge frequency ω_b. $\delta_c = 2\Delta_b$ is the detuning of the atom from the effective "cavity" mode frequency. (b) Schematic representation of the Jaynes-Cummings model: a two-level atom is coupled to a cavity mode with coupling strength g_{JC}. The atom can decay to free space at a rate Γ' (green arrow), while the cavity mode decays at a rate κ (red arrow).

The Hamiltonian describing the coupled atom-photonic crystal system is given by $H = H_0 + V$, where

$$H_0 = \sum_j \omega_{eg}\sigma_j^{ee} + \int dq\, \omega(q) a_q^\dagger a_q, \tag{3.4}$$

$$V = g\sum_j \int dq (\sigma_j^{eg} a_q u_q(x_j) e^{iqx_j} + \text{h.c.}). \tag{3.5}$$

Here a_q is the annihilation operator associated with guided mode q, and $u_q(x)$ is a dimensionless periodic Bloch function associated with the electric field profile of the guided mode. The interaction strength g is given by $g = \wp\sqrt{\omega_b/(4\pi\epsilon_0\hbar A)}$, where A is the effective mode cross-sectional area.

Before deriving the atom-atom interactions, we first note that while the dispersion relation $\omega(q)$ provides the frequency of the guided modes q, it also has physical meaning for frequencies in the band gap. In particular, defining $\Delta_b = \omega_{eg} - \omega_b > 0$ as the detuning of the atomic frequency from the band edge and substituting it in for $\omega(q)$, one finds an imaginary wavevector q as the solution, $q - k = i\sqrt{k^2\Delta_b/\alpha\omega_b}$. This describes an evanescently decaying field, with a corresponding attenuation length of $L = 1/\text{Im}\,(q-k) = \sqrt{\alpha\omega_b/k^2\Delta_b}$. This is the length over which the field from a dipole source would attenuate if its frequency were within the band gap. We now proceed to eliminate the photonic modes to arrive at an effective atom-atom interaction, as formally described in the previous section. Beginning with the manifold of states consisting of any number of atomic ground and excited states and zero photons,

$\{|g\rangle, |e\rangle\}^{\otimes N} \otimes |0\rangle$, the interaction Hamiltonian V couples these states to a manifold with one fewer excited atom and one photon in mode q, $|1_q\rangle$. The goal is to treat the fluctuations to the manifold containing one photon within second-order perturbation theory and project the effective system dynamics back to the zero-photon manifold (*e.g.*, by Schrieffer-Wolff transformation), resulting in a purely atomic interaction. The derived effective Hamiltonian takes the form [46]

$$H_{\text{int}} = \frac{g_c^2}{2\Delta_b} \sum_{jl} u_k(x_j) u_k(x_l)\, e^{-|x_j - x_l|/L}\, \sigma_j^{eg} \sigma_l^{ge}, \tag{3.6}$$

where $g_c = \sqrt{2\pi/L}g$ (note that g is a coupling strength to a continuum and has units $s^{-1}\sqrt{m}$, so g_c has units of s^{-1}). Here, we have assumed that the spatial Bloch modes $u_q \approx u_k$ can be treated as nearly constant near the band edge. For realistic PhC structures they appear sinusoidal $u_k(x) = \cos \pi x/a$ along the axis of the waveguide, *i.e.* at the band edge, the modes form a standing wave exactly as in a Fabry-Perot cavity. The mode area A (which enters in g) and the band curvature α can be calculated independently from numerical simulations for a realistic structure, and upon doing so one finds that the simple model of Eq. (3.6) quantitatively agrees with full Green's function simulations without any free fitting parameters [46].

Hamiltonian (3.6) describes spin-spin interactions between the atoms whose coupling strengths depend on the relative and absolute positions of the atoms. The position-dependent coupling naturally creates correlations between the motional and the internal degrees of freedom of the atoms, which will be systematically investigated, at the level of ground state physics, in Secs. 3.4 and 3.5.

3.3.2 *Dissipative mechanisms*

Writing the effective Hamiltonian in the form of (3.6) suggests an elegant interpretation. Aside from the exponential spatial dependence $e^{-|x_j - x_l|/L}$, the interaction is exactly what one would find for atoms coupled to an off-resonant cavity within the Jaynes-Cummings model [16, 46, 153] described in Sec. 1.1.1 (see Fig. 3.1b). In particular, the Jaynes-Cummings Hamiltonian is given by

$$H_{JC} = \delta_{JC} \sum_j \sigma_j^{ee} + g_{JC} \sum_j \cos kx_j (\sigma_j^{eg} a + \text{h.c.}), \tag{3.7}$$

where g_{JC} is the single-atom vacuum Rabi splitting of the cavity, a is the annihilation operator of the cavity mode, and δ_{JC} is

the atom-cavity detuning. In the far-detuned regime $|\delta_{JC}| > g_{JC}$ the off-resonant photons can be eliminated to yield an effective atom-atom Hamiltonian $H_{JC,eff} = (g_{JC}^2/\delta_c) \sum_{jl} \cos kx_j \cos kx_l \sigma_j^{eg} \sigma_l^{ge}$ (see Eq. (1.7)). Compared to Eq. (3.6), this suggests that the PhC interaction can be understood as arising from an effective cavity, with the mapping $g_{JC} = g_c$ and $\delta_{JC} = \delta_c = 2\Delta_b$ (*i.e.*, the "cavity" mode for the PhC sits Δ_b below the band edge, see Fig. 3.1a). The photon associated with this "cavity" mode is simply that exponentially localized around an excited atom, unable to propagate in the waveguide due to the band gap.

This analogy can in fact be made more formal [46]. In particular, in a real cavity the vacuum Rabi splitting scales with mode volume as $g_{JC} \propto 1/\sqrt{V}$, and it can be shown that the interaction strength $g_c \propto 1/\sqrt{AL}$ in the PhC is exactly the same as a real cavity of the same size. Within the Jaynes-Cummings model, the role of losses is well understood, and one can exploit this mapping to predict the effect of dissipation in the PhC. As discussed in Sec. 1.1.1, within the Jaynes-Cummings model, two fundamental dissipation channels are the spontaneous emission rate of an excited state atom into free space (at a rate Γ' typically comparable to the vacuum emission rate Γ_0), and the decay of the cavity photon at a rate κ (see Fig. 3.1b). We have seen that the probability of losing a photon during the exchange process between two atoms optimized with respect to the detuning δ_{JC} is $\mathcal{E}_{min} = 1/\sqrt{C}$, where $C = g_{JC}^2/(\kappa\Gamma')$ is the single-atom cooperativity factor. In a PhC, the same loss mechanisms occur. An atom trapped near a PhC emits into free space at a rate $\sim \Gamma_0$, and the photon localized around an excited atom sees the absorption and scattering imperfections of the dielectric to decay at a rate κ. This rate κ should be similar to PhC cavities made from the same material and fabrication processes, for which quality factors of $Q > 10^5$ [154] have been achieved. Assuming an interaction length of $L \sim \lambda$, this translates into an effective vacuum Rabi splitting of $g_c/(2\pi) \sim 10$ GHz (for a Cs transition) and a cooperativity of $C_\lambda \sim 10^4$.

3.3.3 *Raman scheme*

In Secs. 3.3.1 and 3.3.2 we have presented the possible achievable strengths of interactions in photonic crystals and the relevant dissipation mechanisms. We now apply these results specifically to the case of observing spin-motion coupling. First, it should be noted that while the photon-mediated interactions in PhC's occur via the excited state, it is generally not convenient to directly work with excited states. In particular, we are interested in observing the influence of spin-motion cou-

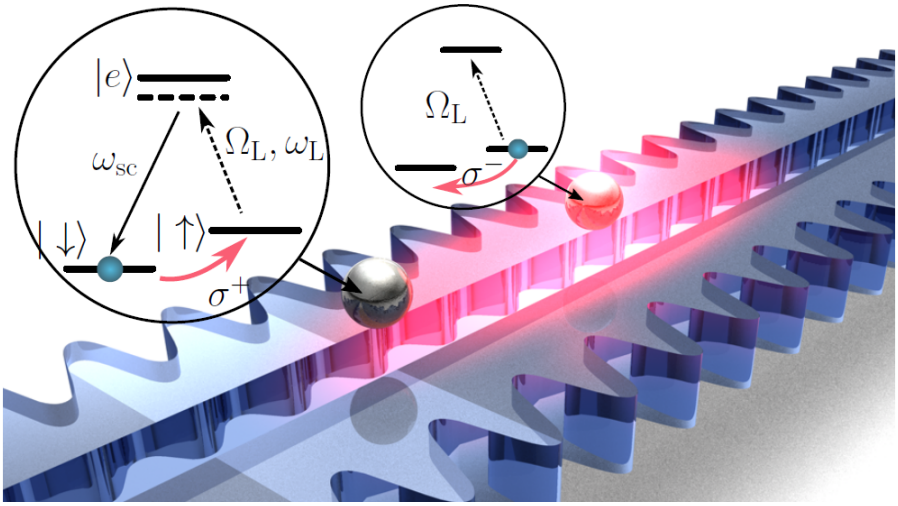

Figure 3.2: Schematic rendering of the "alligator" photonic crystal waveguide [43] with two atoms trapped. The atomic transition $|\uparrow\rangle - |e\rangle$ is globally driven by an external laser with Rabi frequency Ω_L. In principle, an atom originally in $|\uparrow\rangle$ can Raman scatter a laser photon and flip to state $|\downarrow\rangle$. However, when the frequency of the scattered photon ω_{sc} lies within a bandgap (see Fig. 3.1a), this photon becomes bound around the atom (illustrated by the pink cloud). It can be subsequently absorbed by another atom initially in state $|\downarrow\rangle$, resulting in a flip to state $|\uparrow\rangle$.

pling in competition with an external trapping potential for the atoms. Typical external trap frequencies are below $\omega_m/2\pi \lesssim 1$ MHz, which is much smaller than the achievable bare interaction strengths in PhC structures (*e.g.*, $g_c/(2\pi) \sim 10$ GHz), and the excited state decay rate ($\Gamma_0 \sim 2\pi \times 5$ MHz for Cs). Ideally one would like the interaction strength to be comparable to trapping energies, while making dissipation much smaller. To achieve this, one can work within a hyperfine ground-state manifold, employing an additional state $|s\rangle$ within the manifold as illustrated in Fig. 3.2 (here the states $|g\rangle$ and $|s\rangle$ are represented by the "spin" states $|\downarrow\rangle, |\uparrow\rangle$, respectively). A classical control beam Ω_L facilitates Raman transitions between $|g\rangle, |s\rangle$ via the excited state $|e\rangle$. For a control beam detuning Δ_L, the excited state $|e\rangle$ can be eliminated [46], resulting in a Hamiltonian identical in form to Eq. (3.6),

$$H_{int} = \frac{g_c^2}{2\Delta_b}\left(\frac{\Omega_L}{\Delta_L}\right)^2 \sum_{jl} u_k(x_j)u_k(x_l)\, e^{-|x_j-x_l|/L}\, \sigma_j^{sg}\sigma_l^{gs}, \quad (3.8)$$

but with state $|e\rangle$ replaced with state $|s\rangle$ and the interaction strength reduced by a factor $(\Omega_L/\Delta_L)^2$.

Using a Raman process also decreases the optimized dissipation rates by the same factor of $(\Omega_L/\Delta_L)^2$, such that the

square root of cooperativity $\sqrt{C}$ still describes the ratio between the rates of coherent interactions and dissipation [46]. Thus, the general strategy to observe coherent spin-motion coupling is to choose $(\Omega_L/\Delta_L)^2$ such that the characteristic magnitude $J = (g_c^2/\Delta_b)(\Omega_L/\Delta_L)^2$ of the spin-dependent potential becomes comparable to the energy scale of external trapping, which ensures that dissipation is highly suppressed compared to the energy scales in the ideal Hamiltonian. It should also be noted that the Raman process enables the Hamiltonian $H_{int}(t)$ to become time-dependent, if the control field amplitude $\Omega_L(t)$ is varied in time.

From here we will denote the states $|g\rangle$ and $|s\rangle$ as the "spin" states $|\downarrow\rangle, |\uparrow\rangle$, respectively. We can thus rewrite Eq. (3.8) in the equivalent but more compact form

$$H_{int} = \frac{J}{2} \sum_{j,l} f(x_j, x_l)(\sigma_j^+ \sigma_l^- + h.c), \tag{3.9}$$

with $f(x_j, x_l) = e^{-|x_j - x_l|/L} \cos kx_j \cos kx_l$, approximating the Bloch function associated with the electric field at the atomic position with a cosine. $\sigma^- = |\downarrow\rangle\langle\uparrow|$ denotes the spin lowering operator from $|\uparrow\rangle$ to $|\downarrow\rangle$, and conversely for σ^+. We will assume that the atoms are tightly trapped in the transverse direction, such that the position along x is the only dynamical variable. Note that absent any motional effects (*i.e.*, if f is constant), Eq. (3.9) corresponds to the "XX" spin model in 1D [155].

3.4 MANY-BODY MODEL OF INTERACTING ATOMS: CLASSICAL MOTION

We propose in this section a realistic experimental setup, which highlights the interplay of spin and motion, and we investigate it treating the atomic motion classically. Within this scheme, illustrated in Fig. 3.3, atoms interact via the Hamiltonian of Eq. (3.9), and are separately trapped by an external, spin-independent optical lattice $H_{trap} = V_L \sum_j \sin^2 k_{tr} x_j$ (this could originate from optical fields in another guided band far from the atomic resonance). Peculiarly, this lattice traps atoms at the *nodes* of the Bloch function, and thus nominally hides the atoms from the PCW interaction. Despite not being a fundamental requirement to see spin-motion coupling, we assume that the trapping wavelength is such that atoms are localized around even nodes of the Bloch wave functions, *i.e.* $k_{tr} = k/2 = \pi/(2a)$, where a is the length of the unit cell of the PCW. It can be readily shown that within our model, trapping atoms at every site would yield a phase transition with discontinuous change in the atomic positions.

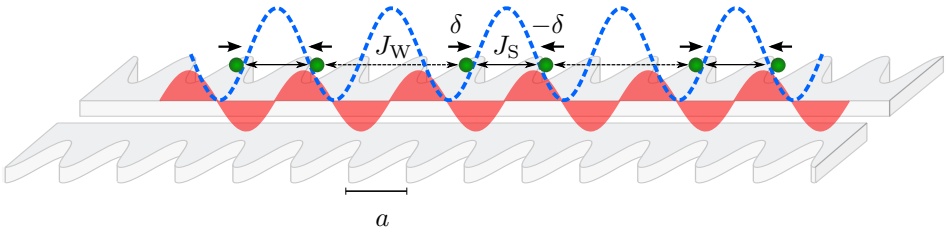

Figure 3.3: Schematic 1D representation of the model, with atoms (green) trapped in an external potential (blue). The photonic-crystal mediated interaction is modulated by the standing wave of the Bloch modes (red), while the external potential creates trapping sites centred around the nodes. The arrows represent the displacement from the trapping sites to a dimerized configuration.

We consider the Hamiltonian in the case of one atom per trapping site and an external magnetic field that can polarize the atoms with energy h along z:

$$\begin{aligned} H &= H_{trap} + H_{magn} + H_{int} = \\ &= \frac{V_L}{2} \sum_j \sin^2 k\delta_j/2 + h \sum_j \sigma_j^z + \frac{J}{2} \sum_{j \neq l} f(x_j, x_l)\,(\sigma_j^+ \sigma_l^- + h.c), \end{aligned} \tag{3.10}$$

where δ_j denotes the displacement of atom j from the bottom of its external well. In the present section we treat the atomic position classically, while investigating the case of quantum motion in the next section. We assume that the coupling strength J is positive. For simplicity, in Eq. (3.10) we also ignore the self-interaction term ($j = l$), which can be compensated by an external potential.

To study the many-body ground state of Hamiltonian (3.10) without any assumption about the spatial configuration is very difficult. Furthermore, for $L/a \gg 1$ the long-range character of the interaction makes the spin model relatively difficult, even for fixed positions. As a consequence, we restrict our attention to the case $L \sim a$, for which we can make a nearest-neighbor approximation.

We can get an intuition of the possible ground state configuration of a system of many atoms by considering how just two atoms in neighboring sites interact. If the atoms remain at the bottom of their trapping wells, the function $f(x_1, x_2) = 0$ as these positions coincide with nodes of the Bloch functions. However, the PCW interaction energy would become negative, if the two atoms were to form a triplet state, $|T\rangle = (|\uparrow\downarrow\rangle + |\downarrow\uparrow\rangle)/\sqrt{2}$ (or a singlet for $J < 0$), and simultaneously displace toward each other to form a spatial dimer. Such a process would

become energetically favourable overall for a certain ratio of J/V_L. Motivated by this simple case we make an ansatz that the spatial configuration of the many-body ground state consists of dimerized pairs. In particular, we assume that $x_j = 2ia + (-1)^j\delta$, where δ represents the displacement from the trap center, as pictured in Fig. 3.3. This is reminiscent of the lattice instability that creates spatial entangled dimers in the spin-Peierls model [68], but with the substantial difference that our system becomes non-interacting in the absence of dimerization (as the atoms are at the nodes). In the following, we treat δ as a variational parameter and proceed to solve the spin ground state exactly.

The nearest-neighbor spin Hamiltonian can be mapped to a chain of spinless fermions through standard Jordan-Wigner transformation [156], with the presence/absence of a fermion on a site corresponding to spin up/down, respectively. Because of the staggered spatial configuration, it is natural to define a unit cell j consisting of a pair of dimerized atoms (labelled L,R). Two different spin couplings $J_{S,W}(\delta) = J\,\sin^2 k\delta\, e^{-(2a\mp 2\delta)/L}$ then characterize the interaction between atoms within the same dimer, and between consecutive atoms R,L in neighboring dimers, respectively (see Fig. 3.3). The Hamiltonian then reads

$$\begin{aligned} H(\delta) = {} & \frac{NV_L}{2}\,\sin^2 k\delta/2 + 2h(c^\dagger_{L,j}c_{L,j} + c^\dagger_{R,j}c_{R,j} - 1) \\ & - \sum_j J_S(\delta)\,(c^\dagger_{L,j}c_{R,j} + h.c) + J_W(\delta)\,(c^\dagger_{R,j}c_{L,j+1} + h.c), \end{aligned} \tag{3.11}$$

where $c_{(L,R),j}$ are fermion annihilation operators for site j. It is convenient then to introduce the fermionic singlet and triplet operators $s_j = (c^\dagger_{L,j} - c_{R,j})/\sqrt{2}$ and $t_j = (c^\dagger_{L,j} + c_{R,j})/\sqrt{2}$ in terms of which (3.11) takes the form

$$\begin{aligned} H(\delta) = {} & E^{tr}(\delta) + 2h\sum_j (t^\dagger_j t_j + s^\dagger_j s_j - 1) - J_S(\delta)\sum_j (t^\dagger_j t_j - s^\dagger_j s_j) \\ & - \frac{J_W(\delta)}{2}\sum_j (t^\dagger_j t_{j+1} - s^\dagger_j s_{j+1} + t^\dagger_j s_{j+1} - s^\dagger_j t_{j+1} + h.c). \end{aligned} \tag{3.12}$$

This Hamiltonian can be exactly diagonalized going to Fourier space, obtaining

$$H(\delta) = E^{tr}(\delta) - Nh + \sum_q \Big[(2h + \epsilon_q)\, d^\dagger_q d_q + (2h - \epsilon_q)\, u^\dagger_q u_q\Big], \tag{3.13}$$

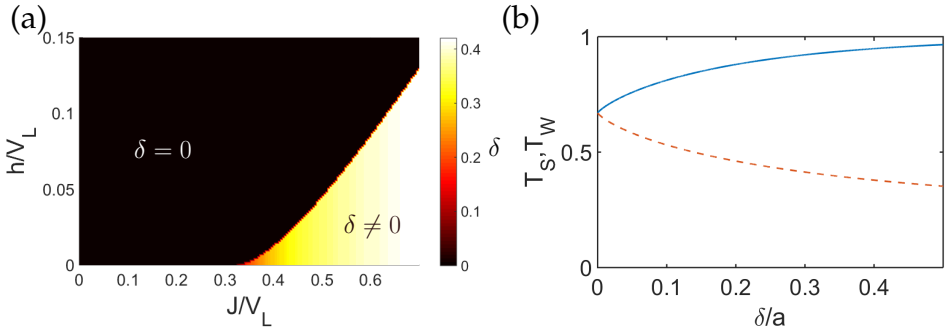

Figure 3.4: (a) Spatial dimerization δ (in units of the lattice constant a), as a function of the interaction strength J and the magnetic field energy h (in units of the external trap depth V_L). (b) Triplet fraction of the reduced density matrix for two atoms within a dimer (T_S, blue solid curve), and consecutive atoms in different dimers (T_W, red dashed), as a function of dimerization δ, at zero magnetic field ($h = 0$).

with the spectrum given by

$$\begin{aligned}\epsilon_q(\delta) &= \left(J_S^2(\delta) + J_W^2(\delta) + 2J_S(\delta)J_W(\delta)\cos q\right)^{1/2} \\ &= J\, e^{-2a/L}\, \sin^2 k\delta \left(4\cosh^2 2\delta/L + 2(\cos q - 1)\right)^{1/2} \qquad (3.14)\end{aligned}$$

and

$$d_q = \frac{1}{\sqrt{(\epsilon_q + a_q)^2 + b_q^2}}\Big(i(\epsilon_q + a_q)t_q + b_q s_q\Big), \qquad (3.15)$$

$$u_q = \frac{1}{\sqrt{(\epsilon_q - a_q)^2 + b_q^2}}\Big(-i(\epsilon_q - a_q)t_q + b_q s_q\Big), \qquad (3.16)$$

with $a_q = J_S(\delta) + J_W(\delta)\cos q$ and $b_q = J_W(\delta)\sin q$. Since ϵ_q is positive for every q and J has been assumed to be positive, the ground state involves only u operators and is equal to

$$|GS\rangle_\delta = \left(\prod_{q|\epsilon_q(\delta)>2h} u_q^\dagger\right)|0\rangle\,. \qquad (3.17)$$

By minimizing the ground-state energy with respect to δ we find the optimal spatial configuration (within the ansatz). In Fig. 3.4a we plot the resulting value of δ as function of the interaction strength J and of the magnetic field h (in units of V_L). In the $J - h$ plane one can clearly distinguish a critical value of the spin interaction strength, $J_{crit}(h)$, above which a phase transition occurs from a non-interacting to a dimerized state. The increase in spin entanglement with dimerization can be

quantified by taking the two-particle reduced density matrix ρ_{2S} of atoms within a dimer, and calculating its overlap with the triplet state, $T_S(\delta) = \langle T|\rho_{2S}|T\rangle = (1/N)\sum_j \langle t_j^\dagger t_j(1 - s_j^\dagger s_j)\rangle$. We plot $T_S(\delta)$ in Fig. 3.4b for zero magnetic field. For $\delta = 0$ this quantity tends to the value in the conventional XX spin model, $T_S(0) = (1/2 + 1/\pi)^2 \approx 0.67$, while for large values of δ and small L it tends to 1. Similarly, defining an analogous quantity $T_W(\delta)$ between consecutive atoms in neighboring dimers, we find a decrease in correlation with increasing dimerization.

3.5 MANY-BODY MODEL OF INTERACTING ATOMS: QUANTUM MOTION

In the previous section we have introduced an experimental scheme which produces correlations between the motional and spin state of the atoms interfaced with the PCW, and we have studied these correlations treating the positions of the atoms as classical variables. In this section we consider a quantum description of both motion and spins for the same model, which is relevant, *e.g.*, if the motion is initially cooled to its ground state.

3.5.1 *Derivation of the Hamiltonian*

As for the classical case, we assume a tight trapping of the atoms around the minima of the external potential, such that tunneling of atoms between sites can be neglected. We then proceed by projecting the Hamiltonian of Eq. (3.10) onto the lowest two motional bands, and denote by $|a\rangle_i$ and $|b\rangle_i$ the associated Wannier functions localized around site i, as shown in Fig. 3.5. In particular, the projection of the interaction Hamiltonian onto the two-band basis is equal to

$$H_{\text{int}} = \frac{J}{2}\sum_{j\neq l}\sum_{\alpha\beta\alpha'\beta'=a,b} V^{jl}_{\alpha\beta\alpha'\beta'}\,\tilde{\sigma}_j^{\alpha\beta}\tilde{\sigma}_l^{\alpha'\beta'}(\sigma_j^+\sigma_l^- + \text{h.c.}), \quad (3.18)$$

where we have introduced the operators $\tilde{\sigma}^{\alpha\beta} = |\alpha\rangle\langle\beta|$, acting on the motional basis. Because of the periodicity of the system, the Wannier wavefunction centered on site j, $w_{j,\alpha}(x)$, is equal to $w_{0,\alpha}(x - x_j)$. Thus the matrix elements appearing in Eq. (3.18) can be written as

$$V^{jl}_{\alpha\beta\alpha'\beta'} = \int dx dx'\, \sin kx \sin kx'\, e^{-|x_j - x_l - x + x'|/L} \times \\ \times\, w_\alpha(x)w_\beta(x)w_{\alpha'}(x')w_{\beta'}(x'), \quad (3.19)$$

with the site dependence now only appearing in the exponential.

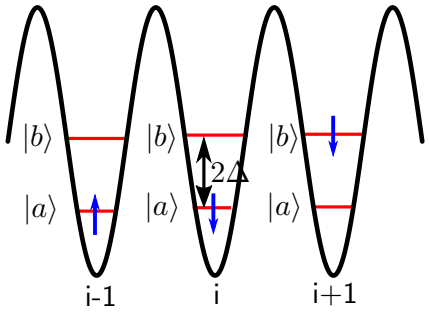

Figure 3.5: Representation of the truncated basis states for few sites. The blue arrow indicates the spin, while the two levels the motional states $|a\rangle$ and $|b\rangle$, separated by an energy difference 2Δ.

To simplify further the matrix elements we can use the initial assumption that the functions are tightly confined around the lattice sites and that the overlap between functions at different sites is negligible. Indeed, $|x - x'| < L$ in the region over which the wavefunctions will have appreciable weight, motivating an expansion of the coefficients in powers of $1/L$. As in the previous section we will assume that $L \sim a$, such that we can make the nearest-neighbor approximation for interactions. By exploiting the parity of the functions w_a and w_b and the sine function, we readily obtain that the zero order expansion of the exponential gives the interaction Hamiltonian

$$H_{int}^{(0)} = 2g \sum_j \tilde{\sigma}_j^x \tilde{\sigma}_{j+1}^x \left(\sigma_j^+ \sigma_{j+1}^- + \text{h.c.}\right), \tag{3.20}$$

while the term coming from the first order expansion gives

$$H_{int}^{(1)} = -2g(2a/L) \sum_j \left\{ \frac{\eta_a + \eta_b}{2\eta_0} \left(\tilde{\sigma}_j^x - \tilde{\sigma}_{j+1}^x\right) + \frac{\eta_b - \eta_a}{2\eta_0} \left(\tilde{\sigma}_j^x \tilde{\sigma}_{j+1}^z - \tilde{\sigma}_{j+1}^x \tilde{\sigma}_{j+1}^z\right) \right\} \left(\sigma_j^+ \sigma_{j+1}^- + \text{h.c.}\right). \tag{3.21}$$

In these expressions we have introduced a set of pseudo-spin operators on each site, $\tilde{\sigma}_j^z = |b_j\rangle\langle b_j| - |a_j\rangle\langle a_j|$, etc., to represent the motional degree of freedom, and we have defined the scaled coupling constant $g = Je^{-2a/L}\eta_0^2/2$ and the factors $\eta_0 = \int dx \sin k_0 x\, w_a(x) w_b(x)$ and $\eta_{a,b} = (1/2a)\int dx\, x \sin k_0 x\, w_{a,b}^2(x)$, whose values depend on the details of the trapping. For concreteness, in the following we take $L = 2a$ and the ratio between the trapping lattice depth V_L and the recoil energy E_R to be 20, for which numerical evaluation of the Wannier functions yields $\eta_0 \approx 0.54$, $\eta_a \approx 0.06$ and $\eta_b \approx 0.16$.

Eq. (3.20) has largest expectation value when atoms sit in an equal superposition of states $|a\rangle$ and $|b\rangle$ such that $\tilde{\sigma}^x = \pm 1$ (*i.e.*, the wave-function is maximally displaced from the center), which reflects that the atoms are trapped at nodes of the PCW. At lowest order in $1/L$, that is, ignoring the exponential in Eq. (3.8) completely, the atoms clearly have no sense of relative spacing, and thus Eq. (3.20) is equally maximized when each atom moves in any direction away from the node. The first order correction in $1/L$, given by Eq. (3.21) is then responsible for spatial dimerization. Adding to the interaction Hamiltonian terms for the energy arising from the band and from the external magnetic field, we get the equivalent of Hamiltonian (3.10) for quantized motion

$$H = \sum_j \Delta\tilde{\sigma}_j^z + h\sigma_j^z + 2g\left\{\tilde{\sigma}_j^x\tilde{\sigma}_{j+1}^x - \frac{a}{L\eta_0}\left[(\eta_a+\eta_b)(\tilde{\sigma}_j^x - \tilde{\sigma}_{j+1}^x)\right.\right.$$
$$\left.\left. + (\eta_b-\eta_a)(\tilde{\sigma}_j^x\tilde{\sigma}_{j+1}^z - \tilde{\sigma}_j^z\tilde{\sigma}_{j+1}^x)\right]\right\}(\sigma_j^+\sigma_{j+1}^- + \text{h.c}). \quad (3.22)$$

This represents the minimal model in which spin and motion can couple, since superpositions of states $|a\rangle$ and $|b\rangle$ yield spatial wave-functions that are displaced from the site centers, but at the same time constitutes an extreme case of spin-orbit coupled systems, as neither an orbital kinetic energy nor a motion-independent spin interaction appear. While in the following we present results for this specific Hamiltonian, we have also performed calculations involving a third band to verify that the conclusions made from the two-band approximation do not qualitatively change.

3.5.2 *Phase diagram*

We study here the phase diagram of Hamiltonian (3.22) in the $g-h$ plane by means of a finite-size density matrix renormalization group (DMRG) algorithm [131] (see Appendix A.2). The resulting phase diagram for $0 \leqslant g, h \leqslant 2\Delta$ is shown in Fig. 3.6 for $N = 62$ atoms, where we can clearly distinguish at least six phases. First, for sufficiently large magnetic fields $h > h_{crit}(g)$, with $h_{crit}(0) = 0$, the spins are fully polarized and thus the spin-motion coupling has no effect. The many-body state is thus separable, with each atom residing in the lowest motional band, $|\psi\rangle = |a,\downarrow\rangle^{\otimes N}$ ("P" phase in Fig. 3.6).

Along the g-axis up to g_{crit} we have a Néel ordered phase "N", where the magnetization per atom $M_z = 1/(2N)\sum_j \langle\sigma_j^z\rangle$ is zero and the Néel order parameter $\Phi = (1/N)\sum_j (-1)^j \langle\sigma\rangle_j^z$ has a finite value, as shown in Fig. 3.7. This phase also extends to finite values of h with a lobe-like shape. The existence of

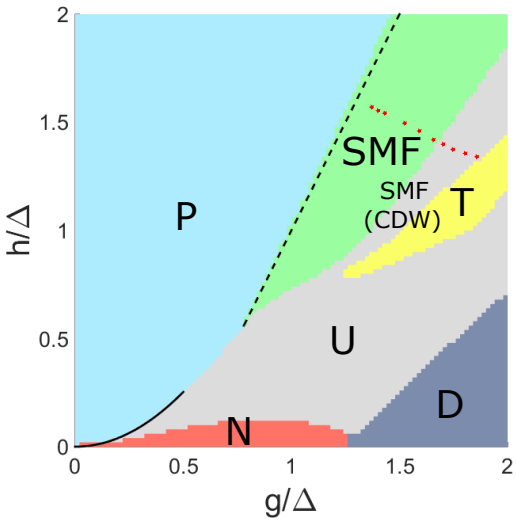

Figure 3.6: Ground state phase diagram obtained studying a system of 62 atoms with open boundary conditions with a DMRG algorithm. We identify unambiguously five phases: a paramagnetic phase (P), a Néel ordered phase (N), a dimerized phase of triplets (D), a spin-motion fluid phase (SMF) and a phase of trimers (T). There is an additional phase corresponding to a charge density wave with quasi-long-range order, labeled as SMF(CDW), and whose boundary with a set of still unknown phases U is not well understood. The continuous line is the border of the paramagnetic phase obtained analytically in the weak coupling regime (see text), the dashed line corresponds to $h = -\Delta + 2g$. The 10 red stars indicate parameters (g, h) where the correlations in Fig. 3.10c are evaluated.

this phase can be predicted analytically in the weak coupling regime, *i.e.* for $g/2\Delta$ small, such that the high-energy excitations associated with populating the upper band can be effectively integrated out. In particular, through a Schrieffer-Wolff transformation [157] on Eq. (3.22) one obtains the following effective Hamiltonian acting only on the spin degrees of freedom:

$$H_{\text{eff,wc}} = -N\Delta + \sum_j h\,\sigma_j^z + J_1\left(\sigma_j^z\sigma_{j+1}^z - 1\right) + 2J_2\left(\sigma_{j-1}^+\sigma_{j+1}^- + \sigma_{j-1}^-\sigma_{j+1}^+\right). \quad (3.23)$$

Here $J_1 = g^2(1+4\chi^2)/2\Delta$, $J_2 = g^2\chi^2/\Delta$ and $\chi = \eta_a/(\eta_0 L)$. Hamiltonian (3.23) describes a nearest neighbor anti-ferromagnetic (AF) Ising model with an additional XX term coupling next-nearest neighbors, with all such terms mediated by virtual phonons. For example, the spin-motion term in Eq. (3.22) proportional to $\tilde{\sigma}_i^x\tilde{\sigma}_{i+1}^x$ enables a fluctuation where two consecutive atoms, anti-aligned in their spins, jump to the higher band and exchange their spins, before returning to the original state (see

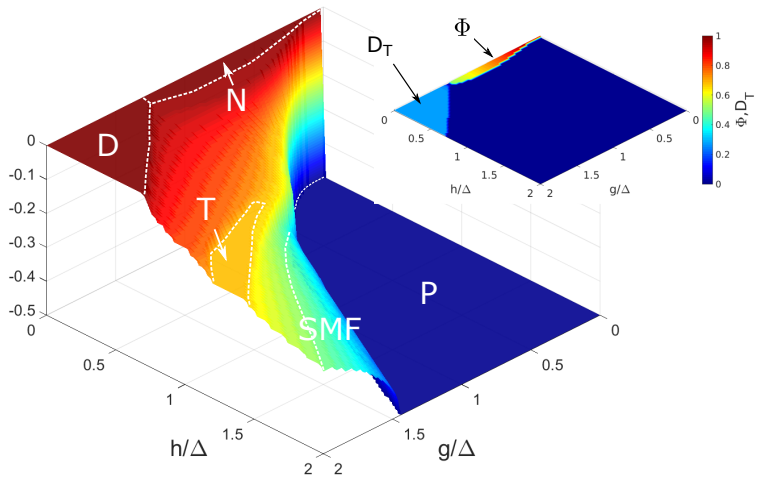

Figure 3.7: Surface plot of the magnetization per atom M_z, with the phases of Fig. 3.6 indicated. Inset: contour plot of the order parameters $|\Phi|$ and $|D_T|$ in a unique color scale.

Fig. 3.8a). This process results in a lower energy for the anti-aligned configuration and produces the longitudinal $(\sigma_j^z\sigma_{j+1}^z - 1)$ term in (3.23). For zero magnetic field, given that $J_1 \gg J_2$ the ground state exhibits AF ordering along z ($\Phi \approx 1$). On the other hand, for $h > h_{crit}(g)$ all spins are in state $|\downarrow\rangle$. Intuitively, one can expect that the transition from Néel ordering to polarized occurs with all $|\downarrow\rangle$ spins in the Néel phase remaining fixed (subchain "A"), while the $|\uparrow\rangle$ spins (subchain "B") "melt" and then re-configure pointing downward. One can thus make an ansatz where subchain A acts as an effective magnetic field for B. Thus, subchain B satisfies an XX model with $H_B^{eff,wc} = \sum_j (h - 2J_1)\sigma_i^z + 2J_2\,(\sigma_j^+\sigma_{j+1}^- + \sigma_j^-\sigma_{j+1}^+)$, which has two phase transitions to polarized phases (for subchain B) at $h = 2(J_1 \pm J_2)$. It follows that for $h < 2(J_1 - J_2)$ the total system (A and B) is in the Néel phase, while for $h > 2(J_1 + J_2)$ it is in the P phase, as illustrated in Fig. 3.8b . In between the two phases the subchain melts under the effective XX model. Since $J_2 \ll J_1$, in the $g - h$ plane this transition region is too narrow to quantitatively match the DMRG results to the XX model predictions, although the effective theory gives correctly the boundary between N and P at $h_{crit}(g) \approx g^2/\Delta$ for $g \ll \Delta$ (solid line in Fig. 3.6).

The Néel order extends to values of $g/\Delta \gtrsim 1$ where the low-energy description of (3.23) is no longer accurate, and decreases discontinuously to zero with the onset of a new phase of dimerized triplets (labelled "D" in Fig. 3.6). This phase is characterized by zero magnetization and a non-zero spin triplet dimer

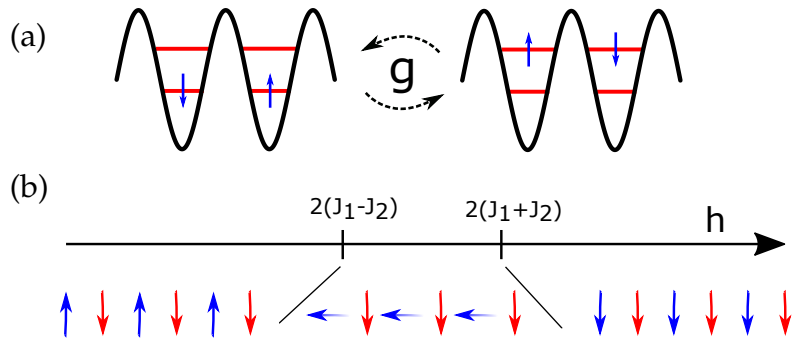

Figure 3.8: (a) The virtual process (for $g \ll \Delta$) of two atoms exchanging the spin excitation by jumping to the motional state $|b\rangle$ and returning to the original state, which gives rise to the effective Ising interaction term of Hamiltonian (3.23). (b) Schematic representation of the ground state spin configuration in the weak coupling regime. For $h < 2(J1 - J2)$ the system is in a Néel ordered phase, while for $h > 2(J1 + J2)$ the spin are all aligned (paramagnetic phase). For intermediate values of h subchains A (in red in the figure) remains completely polarized, while subchain B "melts" under an effective XX model.

order parameter, defined as $D_T = (1/N)\sum_j (-1)^j \langle T|\rho_{j,j+1}|T\rangle$ with $|T\rangle$ being the spin triplet state and $\rho_{j,j+1}$ the two-site spin reduced density matrix (Fig. 3.7). It also has a non-zero spatial dimer order parameter, defined as $D_x = (1/N)\sum_j (-1)^j \langle \tilde{\sigma}^x_j \rangle$. The entangled dimerized structure is evident in Fig. 3.9a, where we plot the triplet fraction in the two-particle density matrix, $\langle T|\rho_{j,j+1}|T\rangle$ and the displacement $\langle \tilde{\sigma}^x_j \rangle$ in a part of the chain for $(g, h) = (1.7, 0.2)\Delta$. Also, we can observe that $|\langle \tilde{\sigma}^x_j \rangle| \sim 1$. Thus, the two-band approximation for the atomic motion is technically violated since the displacement from the trap center is saturated. However, calculations involving a third motional band, which allows for a greater maximum displacement of atoms, exhibit a slower onset of saturation with increasing g but no appearance of new phases (at least within the range of parameters considered). Together, this suggests that an exact calculation involving all bands, although directly unfeasible, would produce a result similar to the previously discussed case of classical motion, with a steadily increasing degree of dimerization and triplet fraction with increasing g.

For simultaneously large values of g and h, there is a spin-motion fluid phase ("SMF") where the system is gapless and the magnetic field strongly polarizes the spins, such that M_z is close to -1/2. This phase corresponds with good approximation to the ground state of the XX Hamiltonian $H^+ = \sum_i (\Delta + h)\tau^z_i + 2g(\tau^+_i \tau^-_{i+1} + \text{h.c.})$. Here τ^z_i is the Pauli matrix with eigenstates

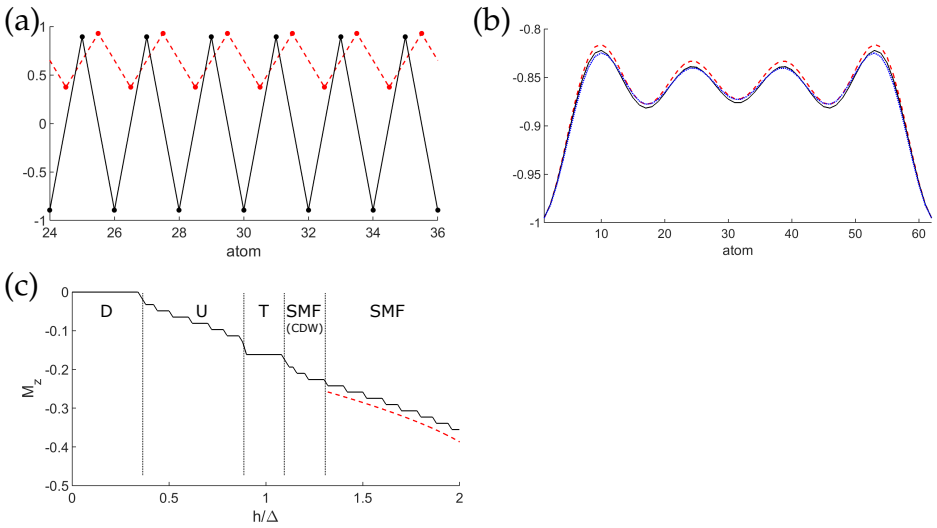

Figure 3.9: (a) Spin triplet fraction $\langle T|\rho_{i,i+1}|T\rangle$ (red dashed line with dots between i and $i+1$) and displacement $\langle\tilde{\sigma}^x_i\rangle$ (black solid line) of the ground state for $(g,h) = (1.7, 0.2)\Delta$, belonging to the dimerized ("D") phase. Only atoms 24-36 are shown for clarity. (b) $\langle\sigma^z_i\rangle$ (black solid line), $\langle\tilde{\sigma}^z_i\rangle$ (red dashed line) along the chain for the ground state at $(g,h) = (1.18, 1.4)\Delta$ belonging to the spin-motion fluid ("SMF") phase. The state contains 4 atoms flipped to $|\uparrow\rangle$ along the direction of the magnetic field. The blue dotted line is $\langle\tau^z_i\rangle$ on the ground state of H^+. (c) Magnetization curve for $g = 1.6\Delta$ as a function of h. The red dashed line is the magnetization predicted by H^+ for the SMF phase.

$|\Downarrow\rangle = |a,\downarrow\rangle$ and $|\Uparrow\rangle = |b,\uparrow\rangle$, while $\tau^\pm$ are associated raising and lowering operators. Thus, this phase corresponds to a dilute fluid of *composite flips* of spin and motion. The existence of this phase can be understood by noting that for large magnetic field, the system is only dilutely populated by spins pointing up. Thus the terms in Eq. (3.22) proportional to $\eta_{a,b}$ that are responsible for dimerization can be neglected. The structure of the remaining Hamiltonian connects naturally the states $|\Downarrow\rangle$ directly to $|\Uparrow\rangle$, in the form of H^+. The locking between spin and motional correlations can be observed in Fig. 3.9b, where the expectations values of σ^z_i and $\tilde{\sigma}^z_i$ obtained with DMRG are plotted for a representative point in the phase. The oscillations of $\langle\sigma^z_i\rangle$ and $\langle\tilde{\sigma}^z_i\rangle$ are due to the open boundary conditions in a finite system and are observable also in a pure XX model. In Fig. 3.9c the magnetization curve predicted by H^+ is compared with the numerical result from the DMRG study of the full Hamiltonian for $g = 1.6\Delta$, showing good agreement, while in Fig. 3.6 the predicted boundary with the "P" phase $h_{crit}(g) \approx -\Delta + 2g$ is represented by a dashed line.

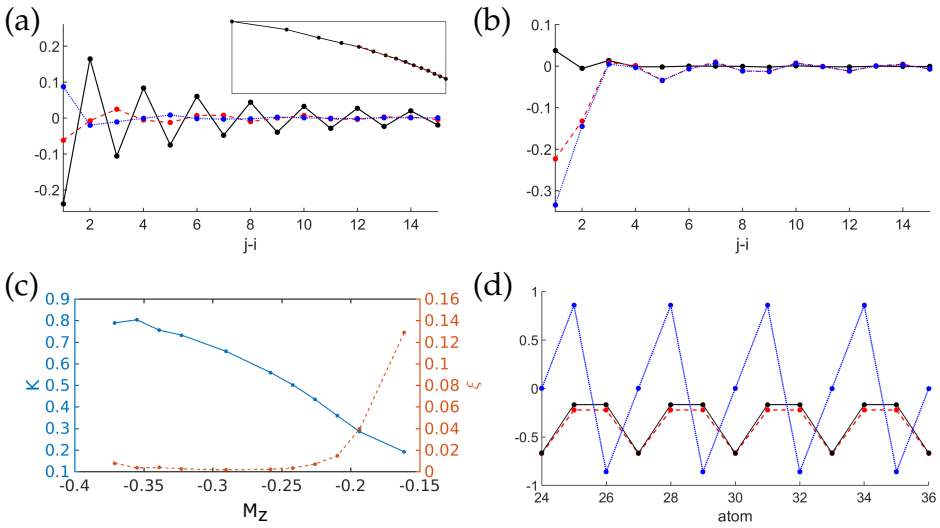

Figure 3.10: (a) Correlation functions $C^X_{ij} \equiv \langle X^+_i X^-_j \rangle - \langle X^+_i \rangle \langle X^-_j \rangle$ with X equal to τ (black solid line), $\tilde{\sigma}$ (red dashed line) and σ (blue dotted line) at $(g, h) = (1.74, 1.38)\Delta$, in the SMF(CDW) region of the phase diagram. The value of $i = 29$ is taken fixed in the bulk of the chain and j is ranging from 30 to 44. Inset: $|C^\tau_{ij}|$ plotted on a log-log scale (black curve), as is the best fit to a Luttinger liquid power-law decay for the points $|i - j| > 4$ (red dashed line). (b) As in (a) but for the density correlation functions $\langle X^z_i X^z_j \rangle - \langle X^z_i \rangle \langle X^z_j \rangle$. (c) In blue: value of the fitted Luttinger parameter K as a function of the magnetization, obtained by fitting the long-range part of the C^τ_{ij} correlation function for the (g, h) values marked by stars in Fig. 3.6b. In red: sum of the squares of the residuals ξ of the fit. (d) $\langle \sigma^z_i \rangle$ (black solid line), $\langle \tilde{\sigma}^z_i \rangle$ (red dashed line) and $\langle \sigma^x_i \rangle$ (blue dotted line) along the chain for the ground state at $(g, h) = (1.7, 1.1)\Delta$, where the ground state belongs to the trimer ("T") phase.

For $-1/4 \lesssim M_z < 0$, H^+ no longer serves as a good description for the ground state. Most of this region consists of a set of phases "U" whose origin is not completely understood yet. However, for strong interactions $g/\Delta \gtrsim 1$, the system qualitatively appears to behave as an interacting Luttinger liquid for the τ particles. Numerical evidence is shown in Fig. 3.10a, where the two-point correlation functions $C^X_{ij} \equiv \langle X^+_i X^-_j \rangle - \langle X^+_i \rangle \langle X^-_j \rangle$ are plotted for various $X = \tau, \sigma, \tilde{\sigma}$, for a representative set of values $(g, h) = (1.74, 1.38)\Delta$. In particular, if τ behaves as a Luttinger liquid, then the long-range decay of interactions is predicted to have a power law form of $C^\tau_{ij} \sim (-1)^{|j-i|} |j - i|^{-1/2K}$ [158]. The inset of Fig. 3.10a plots the absolute value $|C^\tau_{ij}|$ on a log-log scale, which confirms an approximate power law decay. On the other hand, correlations of the other degrees of freedom exhibit

more erratic behavior. Similar observations hold for the density correlation functions (Fig. 3.10b). We fit the Luttinger parameter K [158] from the numerical data, taking the ten (g, h) values indicated by red stars in Fig. 3.6b across the SMF to U boundary. These fits are performed on the points $|i-j| > 4$ of C^{τ}_{ij}, in order to reduce the influence of short-range corrections, which exist even for an ideal Luttinger liquid [158]. The inset of Fig. 3.10a shows the best fit (red dashed line) for $(g, h) = (1.74, 1.38)\Delta$, while the fitted values of K for all ten chosen (g, h) points are plotted in Fig. 3.10c. We have also simultaneously plotted ξ, the sum of the squares of the residuals between the best linear fit on a log-log scale and the numerical data. We note that while the choice of region of exclusion of $|i-j| \leqslant 4$ in taking the fit is somewhat arbitrary, modifying this region (or excluding no points at all) does not change the qualitative conclusions. The decrease below $K = 1$ is indicative of the formation of a charge density wave phase with quasi-long-range order, *i.e.* algebraic decay of the correlation functions. We thus denote this part of the phase diagram as SMF(CDW). The precise boundary of this phase and the nature of the transition to neighboring phases is still not completely understood.

Approaching $M_z \to -1/6$ we notice that not only the fitted value of K tends to zero but also the quality of the fit decreases rapidly, as indicated by the increase in the residual error ξ. This indicates a change of the decay of the correlation function from polynomial to exponential. This is in agreement with the fact that the decrease in K is also known to facilitate the possibility of phases with spontaneously broken symmetry, which is observed in our system as well. At $M_z = -1/6$ (one third of the maximum magnetization), we observe indeed the presence of a plateau in the magnetization curve (Figs. 3.7 and 3.9c), for values of g sufficiently large. In this region the ground state assumes a trimerized configuration, as shown in Fig. 3.10d, where $\langle \sigma^z_i \rangle$, $\langle \tilde{\sigma}^z_i \rangle$ and the displacement $\langle \tilde{\sigma}^x_i \rangle$ are plotted. While we are not able to predict the appearance of such a plateau in our model from first principles, we note that all of its features are consistent with the conditions of Ref. [159]. In particular, our Hamiltonian allows for a gapped phase with spontaneously broken symmetry in the ground state with spatial periodicity $n = 3$, provided that the quantization condition $n(S - M_z) =$ integer is satisfied (here $S = 1/2$ is the total spin). Such a gapped phase should be accompanied by a magnetization plateau.

3.6 CONCLUSIONS

The platform of cold atoms coupled to photonic crystals offers fascinating opportunities to create quantum materials in which spin and motion interact strongly with one another. We have analysed in detail the ground state properties of one experimentally feasible setup, but there exist many exciting avenues for future research. The field of interfacing atoms and photonic crystals is still new and rapidly developing, which makes it difficult to say precisely how the ground state or nearby states can be probed and prepared, but we briefly describe some of the possibilities here. First, it has already been demonstrated that tightly focused optical tweezers can be used to controllably position single atoms nearby nanophotonic structures and couple the atom to the optical mode [154]. Separately, there have been spectacular experiments to create arrays of up to $\sim 10^2$ atoms in individual optical tweezers [84, 85, 160], and demonstrated capabilities in such systems for motional ground-state cooling and spin readout [160]. An optical tweezer array applied to nanophotonic systems could then be a promising route toward both deterministic positioning of atoms and single-site resolution. Absent single-site measurements, there are a number of global measurements that could be applied to yield signatures of the various phases. For example, it has also been theoretically and experimentally shown [62, 88, 121, 122] that different atomic spatial patterns can give rise to very different global reflection and transmission spectra for a weak guided probe field. Similar to free space, a guided mode could also be used to efficiently read out global spin properties [17]. In terms of preparation of the ground state, one likely possibility would be through adiabatic evolution (given that the atomic "spin" states are internal states that do not readily thermalize). Here, the atoms would be initially optically pumped to a separable state (such as $|\downarrow\rangle^{\otimes N}$), which corresponds to the ground state of a single-particle Hamiltonian H_s. The system could then adiabatically evolve through a Hamiltonian $H(t) = H_s(t) + H_{int}(t)$, where the single-particle Hamiltonian is gradually turned off while the PCW interactions are turned on. Understanding the fidelity of this process requires a more thorough investigation of the excitation spectrum, which itself should exhibit non-trivial properties, including the possibility of signatures of fractional spin [161].

The strong coupling between spin and motion more broadly invites a number of other intriguing questions. For example, it would be interesting to understand the transport properties when spin and motion strongly hybridize. Moreover, it would

be highly interesting to consider models without an external lattice potential, and investigate whether the spin interaction alone can produce full spin-entangled crystallization. One might also consider models where the spin part of the interaction already exhibits non-trivial character, such as frustration or topology. Finally, in terms of applications, it would be interesting to explore whether specially engineered spin-motion Hamiltonians can give rise to useful many-body spin states (such as squeezed states for metrology), when the spin interaction alone is incapable of producing such states.

4

SECOND-ORDER QUANTUM NONLINEAR OPTICAL PROCESSES IN GRAPHENE NANOSTRUCTURES AND ARRAYS

4.1 INTRODUCTION

In Section 1.1 and 1.2 we have reviewed the main approaches to obtain optical nonlinearities at the level of single photons by exploiting the nonlinearity of the individual atom. The use of bulk materials for the same task is typically prevented by the extremely low nonlinear coefficients of conventional nonlinear crystals. An open question is if recently discovered low-dimensional materials such as graphene can instead provide a useful platform for quantum nonlinear optics.

In this chapter, we show that graphene is a promising second-order nonlinear material at the single-photon level due to its extraordinary electronic and optical properties [72]. This approach makes use of the fact that a conductor enables a nonlinear optical interaction that is spatially nonlocal over a distance comparable to the inverse of the Fermi momentum k_F. In graphene, this length can be electrostatically tuned to be significantly larger than in typical conductors. At the same time, graphene can support tightly confined surface plasmons (SPs) –combined excitations of electromagnetic field and charge density waves– whose wavelength is reduced well below the free-space diffraction limit [73] and whose momentum q_p is consequently enlarged. We show that the ability to achieve ratios q_p/k_F approaching unity enables giant second-order interactions between graphene plasmons.

We first study the implications of such nonlinearities in a finite-size nanostructure, obtaining a general scaling law for the nonlinearity as a function of the linear dimension of the structure and the doping. To give an explicit example, we compute numerically the nonlinearities associated with a structure designed to support plasmon resonances at frequencies ω_p and $2\omega_p$, which enables second harmonic generation (SHG) or down conversion (DC). Under realistic conditions, we find that the rate of internal conversion between a single quantized plasmon in the upper mode and two in the lower mode can be roughly 1% of the bare frequency, indicating a remarkable interaction strength.

It is not straightforward to directly observe plasmons, and instead they are typically excited and coupled out to propagating photons with low efficiencies. Thus, we then investigate how the extremely strong internal nonlinearities can manifest themselves given free-space input and output fields. First, we show that the collectively enhanced coupling of an array of nanostructures to free-space fields enables an extremely low-intensity input beam to be converted to an outgoing beam at the second harmonic, via interaction with plasmons. Next, we derive an important fundamental result, that while such an array can collectively increase the linear coupling between free fields and plasmons, it ultimately *dilutes* the effect that the intrinsic nonlinearities of plasmons can have on these free fields. Motivated by this, we finally argue that it is crucial to develop techniques to couple efficiently to single nanostructures. We show that efficient coupling would enable SHG or DC with inputs at the single-photon level, and predict a set of experimental signatures in the output fields that would verify that strong quantum nonlinear interactions are occurring between graphene plasmons.

4.2 SECOND-ORDER NONLINEAR CONDUCTIVITY OF GRAPHENE

Graphene has attracted tremendous interest due to its ability to support tightly confined, electrostatically tunable SPs [73–77, 162–164]. More recently, the nonlinear properties have gained attention [165–169]. For example, four-wave mixing produced by single-pass transmission through a single graphene layer has been observed [166], while a second-order response at oblique incidence angles has been predicted [167], and intrinsic second-order nonlinearities have been used to excite graphene plasmons from free-space beams via difference frequency generation [168]. It has also been proposed that graphene nanostructures could enable quantum third-order nonlinearities [169].

We use a unified approach to determine the linear and nonlinear properties within the single-band approximation based upon the semi-classical Boltzmann transport equation [165, 169–171]. This approach is semi-classical in the sense that the quantum-mechanical band dispersion relation of the carriers is included in the theory, but the position and momentum of the carriers obey classical equations of motion. In particular, within this theory the carriers are described by means of a distribution function $f_{\mathbf{k}}(\mathbf{r}, t)$, which is defined so that

$$dN = f_{\mathbf{k}}(\mathbf{r}, t)\, d^2\mathbf{k}\, d^2\mathbf{r} \tag{4.1}$$

is the number of carriers with positions lying within a surface element $d^2\mathbf{r}$ about $\mathbf{r}$ and momenta lying within a momen-

tum space element $d^2\mathbf{k}$ about $\mathbf{k}$, at time t. The position and momentum $\mathbf{k}$ and $\mathbf{r}$ obey the classical equations of motion: $\dot{\mathbf{r}} = \mathbf{v}_\mathbf{k} = (1/\hbar)\partial\epsilon_\mathbf{k}/\partial\mathbf{k}$, and $\hbar\dot{\mathbf{k}} = -e\mathbf{E}$. $\epsilon_\mathbf{k}$ is the dispersion relation of graphene, and since we are interested in energy scales $\lesssim 1$ eV, we linearize it around the Dirac points, *i.e.* $\epsilon_\mathbf{k} = \pm\hbar v_F|\mathbf{k}|$, where +(-) denotes doping to positive (negative) Fermi energies E_F. The single-band approximation, and thus most of the results presented here, holds provided that the optical frequency is less than $\sim 2E_F$, such that absorption arising from interband electron-hole transitions is suppressed [162]. When collisions between the carriers are neglected, the conservation equation for the carrier distribution function $f_\mathbf{k}(\mathbf{r}, t)$ is

$$\frac{d}{dt}f_\mathbf{k}(\mathbf{r}, t) = \frac{\partial}{\partial t}f_\mathbf{k}(\mathbf{r}, t) + \dot{\mathbf{r}}\cdot\nabla_\mathbf{r}f_\mathbf{k}(\mathbf{r}, t) + \dot{\mathbf{k}}\cdot\nabla_\mathbf{k}f_\mathbf{k}(\mathbf{r}, t) = 0. \quad (4.2)$$

Inserting in Eq. (4.2) the equations of motion for $\mathbf{r}$ and momentum $\mathbf{k}$, we obtain the Boltzmann equation, which describes the dynamics of the distribution function,

$$\frac{\partial}{\partial t}f_\mathbf{k}(\mathbf{r}, t) \pm v_F\hat{\mathbf{k}}\cdot\nabla_\mathbf{r}f_\mathbf{k}(\mathbf{r}, t) = \frac{e}{\hbar}\mathbf{E}(\mathbf{r}, t)\cdot\nabla_\mathbf{k}f_\mathbf{k}(\mathbf{r}, t), \quad (4.3)$$

where here $\mathbf{E}$ is the sum of the external field $\mathbf{E}^{ext}$ and the induced field $\mathbf{E}^{ind}$ generated by the carrier distribution.

The macroscopic quantities such as the density of charge and the surface current can be related to the microscopic dynamics of the carriers. For instance, the surface current depends on the microscopic carrier velocities as

$$\mathbf{J}(\mathbf{r}, t) = -eg_v g_s\int\frac{d^2\mathbf{k}}{(2\pi)^2}\mathbf{v}_\mathbf{k}f_\mathbf{k}(\mathbf{r}, t), \quad (4.4)$$

where $g_s = g_v = 2$ are the spin and valley degeneracies of graphene.

The set of Eqs. (4.3) and (4.4) is nonlinear, since the electric field on the right-hand side of Eq. (4.3) depends on the carrier distribution. The strategy we adopt to solve the nonlinear system is to solve perturbatively Eq. (4.3) and then use Eq. (4.4) to get the relation between the surface current and the electric field (*i.e.* the conductivity) at the different orders. In particular, in Fourier space Eq. (4.3) can be written as

$$f_\mathbf{k}(\mathbf{q}, \omega) = \frac{ie}{\hbar(\omega \mp v_F\hat{\mathbf{k}}\cdot\mathbf{q})}\int\frac{d^2\mathbf{p}}{(2\pi)^2}\int_{-\infty}^{\infty}\frac{d\nu}{2\pi}\mathbf{E}(\mathbf{q}-\mathbf{p}, \omega-\nu)\cdot\frac{\partial f_\mathbf{k}(\mathbf{p}, \nu)}{\partial\mathbf{k}}. \quad (4.5)$$

At lowest order, one assumes that $f_\mathbf{k}$ is slightly displaced from its equilibrium (zero temperature) Fermi distribution, $f^{(0)}_\mathbf{k}(\mathbf{r}, t) =$

$\theta(k_F - k)$. Thus, one can substitute $f_{\mathbf{k}}^{(0)}$ into the r.h.s. term of equation (4.5), obtaining the first order contribution to f:

$$f_{\mathbf{k}}^{(1)}(\mathbf{q},\omega) = -\frac{ie\hat{\mathbf{k}}\cdot\mathbf{E}(\mathbf{q},\omega)}{\hbar(\omega \mp v_F\hat{\mathbf{k}}\cdot\mathbf{q})}\delta(k-k_F). \tag{4.6}$$

Inserting Eq. (4.6) yields a linear relationship between the current and the electric field $J_i(\mathbf{q},\omega) = \sigma_{ij}^{(1)}(\mathbf{q},\omega)\,E_j(\mathbf{q},\omega)$, where

$$\sigma_{ij}^{(1)}(\mathbf{q},\omega) = \frac{ie^2 g_v g_s v_F}{\hbar}\int\frac{d^2\mathbf{k}}{(2\pi)^2}\frac{k_i k_j}{k^2(\omega \mp v_F\hat{\mathbf{k}}\cdot\mathbf{q})}\delta(k-k_F). \tag{4.7}$$

In the long-wavelength limit ($v_F q/\omega \ll 1$) one can expand the denominator in q to the zero order obtaining the well-known (local) linear Drude conductivity [74, 75]

$$\sigma^{(1)}(\omega) = \frac{ie^2|E_F|}{\pi\hbar^2\omega}. \tag{4.8}$$

Before calculating the second order conductivity we observe that graphene is a centro-symmetric material, which is typically associated with a vanishing second-order nonlinearity [1]. Indeed, if the nonlinear response is spatially local, $J^{(2)}(2\omega,\mathbf{r}) = \sigma^{(2)}(\omega)E(\omega,\mathbf{r})^2$, spatial inversion symmetry implies that $-J = \sigma^{(2)}(-E)^2$, which enforces that $\sigma^{(2)} = 0$. This argument breaks down if the conductivity is nonlocal [172], for example if $\sigma(\omega,q) \propto q$, such that the current depends on the electric field gradient, $J^{(2)} = \sigma^{(2)}(\omega)E\partial_{\mathbf{r}}E$.

In principle, nonlocal effects are present in any material. For a given electric field strength, the size of this nonlinear effect depends on a dimensionless parameter k/k_{nl} [173]. Here k is the wavevector of the light that dictates how rapidly the field changes in space, and k_{nl}^{-1} is a characteristic length scale over which carriers in the material become sensitive to field gradients. In materials where the charges are tightly bound to their atoms, the relevant length scale k_{nl}^{-1} is given by the atomic size of Angstroms, which is thus negligible compared to optical wavelengths. In conducting materials, the length scale is set by the typical distance between carriers, which is proportional to the inverse of the Fermi wavevector. In a typical metal like silver, the high carrier density also yields a negligible length scale of $k_{nl}^{-1} \sim k_F^{-1} \sim 1$ Angstrom. In contrast, in graphene we can simultaneously exploit two effects to increase significantly k/k_{nl}. First, graphene can be electrostatically tuned to have very low carrier densities to increase k_F^{-1}. Second, one can use tightly confined plasmon excitations in graphene, which have been shown to yield a reduction in the wavelength (or equivalently enhancement in wavevector q_p) compared to free-space light by

two orders of magnitude. Indeed, below we show specifically that $k/k_{nl} \sim q_p/k_F \lesssim 1$ emerges as the relevant quantity to characterize the strength of nonlocal nonlinearities in graphene.

After these considerations, we calculate the second-order conductivity using the same procedure adopted for the calculation of the linear conductivity. In particular we first insert $f^{(1)}$ into the r.h.s. of (4.5) to obtain $f^{(2)}$, and then use the result in Eq. (4.4) to obtain the second-order conductivity. As with the linear conductivity we expand it in powers of q_p, in order to have an analytical expression in the long-wavelength limit. As expected, the zeroth-order term, which corresponds to the local contribution, vanishes, while the term linear in q_p provides a relation (in real space) between the electric fields at frequency ω_p and an induced current density at frequency $2\omega_p$

$$J_i^{2\omega_p} = \sigma^{(1)}(2\omega_p)\, E_i^{2\omega_p} + \sigma^{(2)}_{ijkl}(2\omega_p;\omega_p)\, E_j^{\omega_p} \nabla_k E_l^{\omega_p}. \qquad (4.9)$$

Here $ijkl$ denote in-plane vector indices and summation over repeated indices is implied. The nonlocal second order conductivity tensor reads

$$\sigma^{(2)}_{ijkl}(2\omega_p;\omega_p) = \mp \frac{ie^3 g_v g_s v_F^2}{32\pi\hbar^2\omega_p^3} \left(5\delta_{ij}\delta_{kl} - 3\delta_{ik}\delta_{jl} + \delta_{il}\delta_{jk}\right). \quad (4.10)$$

This result can be converted into a relation between the electrostatic potential and the induced charge, which reproduces previously obtained results for the nonlinear polarizability [167].

4.3 QUANTUM MODEL OF INTERACTING GRAPHENE PLASMONS

The Drude conductivity for infinite graphene given by equation (4.8) provides a valid description of the carrier dynamics of graphene when $\hbar\omega \lesssim E_F$ [74, 75], where the interband transitions can be neglected. Like any conductor in contact with a dielectric (or vacuum, as we assume here), graphene supports SPs with a dispersion relation given by

$$\frac{q_0}{q_p} \approx 2\alpha \frac{E_F}{\hbar\omega_p}, \qquad (4.11)$$

where $q_0 = \omega/c$ is the free-space wavevector at the same frequency and $\alpha \approx 1/137$ is the fine structure constant. As $E_F \gtrsim \hbar\omega_p$, equation (4.11) indicates a reduction in the plasmon wavelength compared to free space by up to two orders of magnitude, which should significantly drive up the effects of spatially nonlocal interactions.

We have seen that at fixed field strength, the nonlinear interactions between plasmons in graphene should be increased

due to a large ratio of q_p/k_F. However, what is most important for nonlinear optics is how to maximize the interaction strength per photon (*i.e.* per quantized plasmon). A simple argument, made more precise below, is that because the energy of a single plasmon is fixed at $\hbar\omega_p$, confining it to as small volumes V as possible maximizes its intensity or electric field, $E_0 \sim \sqrt{\hbar\omega_p/\epsilon_0 V}$. This motivates the study of nonlinear optical interactions between plasmons in nano-structures, which we now present in detail. As a specific example, we will focus on nanostructures that have plasmon resonances at frequencies ω_p and $2\omega_p$. This particular choice of structure is to facilitate DC or SHG.

The derivation of the quantum Hamiltonian of the system starts from the expression of the electrostatic energy (a valid approach provided that the linear dimension of the structure D is small compared to the free-space wavelength λ_0 so that retardation effects can be neglected)

$$H = \frac{1}{2}\int_S d^2\mathbf{r}\left(\rho^{\omega_p *}(\mathbf{r})\phi^{\omega_p}(\mathbf{r}) + \rho^{2\omega_p *}(\mathbf{r})\phi^{2\omega_p}(\mathbf{r})\right), \tag{4.12}$$

where ρ is the charge density and ϕ the electrostatic potential. The charge density can be replaced by the current density using the continuity equation. The potential can be expressed as well in terms of the electric field, obtaining

$$H = \frac{1}{2i\omega_p}\int_S d^2\mathbf{r}\, J_i^{\omega_p *}(\mathbf{r})E_i^{\omega_p}(\mathbf{r}) + \frac{1}{4i\omega_p}\int_S d^2\mathbf{r}\, J_i^{2\omega_p *}(\mathbf{r})E_i^{2\omega_p}(\mathbf{r}). \tag{4.13}$$

After expressing the current at frequency ω_p in terms of the electric field, we impose the quantization condition to the first mode:

$$\frac{\sigma^{(1)}(\omega_p)}{2i\omega_p}\int_S d^2\mathbf{r}\,|E_i^{\omega_p}(\mathbf{r})|^2 = \hbar\omega_p\, a^\dagger a, \tag{4.14}$$

which can be enforced with the substitution $E_i^{\omega_p}(\mathbf{r}) \to \tilde{E}_i^{\omega_p}(\mathbf{r})\, a = E_0^{\omega_p} f_i^{\omega_p}(\mathbf{r})\, a$. Here, $f^{\omega_p}(\mathbf{r})$ is a vectorial function which describes the geometry of the mode and normalized such that $\max|f^{\omega_p}(\mathbf{r})| = 1$, $E_0^{\omega_p} = \left(\hbar\omega_p q_p/\epsilon_0 S\mu\right)^{1/2}$ is the maximum single-photon electric field amplitude, and $\mu = S_{\text{eff}}^{\omega_p}/S$, with $S_{\text{eff}}^{\omega_p} = \int_S d^2\mathbf{r}\,|f_i^{\omega_p}(\mathbf{r})|^2$ being the ratio between the effective mode area and the physical area of the structure. Similarly we can use the result of the previous section to express the current at frequency $2\omega_p$ in terms of the electric field and quantize the second mode.

We obtain in this way the quantum Hamiltonian of the structure

$$H = \hbar(\omega_p - i\Gamma_a/2)\, a^\dagger a + \hbar(2\omega_p - i\Gamma_b/2)\, b^\dagger b + \hbar g\left(b^\dagger a^2 + \text{h.c.}\right),$$

(4.15)

where a and b are the annihilation operators of the two SP modes, and g is an oscillation rate between a single plasmon with frequency $2\omega_p$ and two plasmons with frequency ω_p [174]. Adopting a quantum jump approach we have added to the frequencies an imaginary part accounting for the total decay rates Γ_a and Γ_b of the two modes. The quantization associates with a single plasmon a typical electric field amplitude $E_0^{\omega_p} \sim \left(\hbar\omega_p q_p/\epsilon_0 S\right)^{1/2}$, where S is the structure area, confirming the large per-plasmon field associated with tight confinement.

The quantum coupling constant g is rigorously given by the classical interaction energy between the nonlinear current at $2\omega_p$ and the fields at ω_p, but with the classical field values replaced by the per-photon field strengths $\tilde{\mathbf{E}}^{\omega_i}(\mathbf{r})$

$$\hbar g = \left| \frac{1}{4i\omega_p} \sigma^{(2)}_{ijkl}(2\omega_p;\omega_p) \int_S d^2\mathbf{r}\, \tilde{E}_i^{2\omega_p}(\mathbf{r}) \tilde{E}_j^{\omega_p}(\mathbf{r}) \nabla_k \tilde{E}_l^{\omega_p}(\mathbf{r}) \right|. \tag{4.16}$$

Eq. (4.16) shows that g is directly proportional to the second-order conductivity $\sigma^{(2)}_{ijkl}$ calculated in the previous section, and its dependence on the particular geometric configuration of the modes is confined to the overlap integral [175]. It should be noted that for extended graphene, the mode functions are simply propagating plane waves $E(\mathbf{r}) \sim e^{ikz}$. Thus the integral in Eq. (4.16) produces a delta function, $g \propto \delta(2k_1 - k_2)$, which reflects momentum conservation. In contrast, in small structures the spatially complex modes can be thought of as a superposition of many different wavevectors, and a large interaction strength is ensured by engineering the modes such that they have good spatial overlap [176].

Using the fact that $E_0^{\omega_p} \sim \left(\hbar\omega_p q_p/\epsilon_0 S\right)^{1/2}$, that the nonlinear conductivity has an amplitude $\sigma^{(2)} \sim e^3 v_F^2/\hbar^2\omega_p^3$, and that the field gradients occur over a length scale q_p^{-1}, one can readily verify that equation (4.16) predicts a general scaling of $g/\omega_p = \beta/(k_F D)^{7/4}$. The dimensionless coefficient of proportionality, which we call β, depends only on the geometric overlap of the modes (*e.g.*, $\beta = 0$ if the modes have the wrong symmetries, or $\beta \sim 1$ for modes with good overlap). As the minimum dimension of the structure should be comparable to the plasmon wavelength, $D \sim 1/q_p$, the maximum ratio of g/ω_p scales like $(q_p/k_F)^{7/4}$, confirming the enhanced nonlinearities as q_p become comparable to k_F. Note that this relation is valid only for $q_p \lesssim k_F$, where the conductivity of graphene is Drude-like, as discussed above. In this derivation, we have assumed that a finite-size structure has the same conductivity as infinite graphene. Although this is

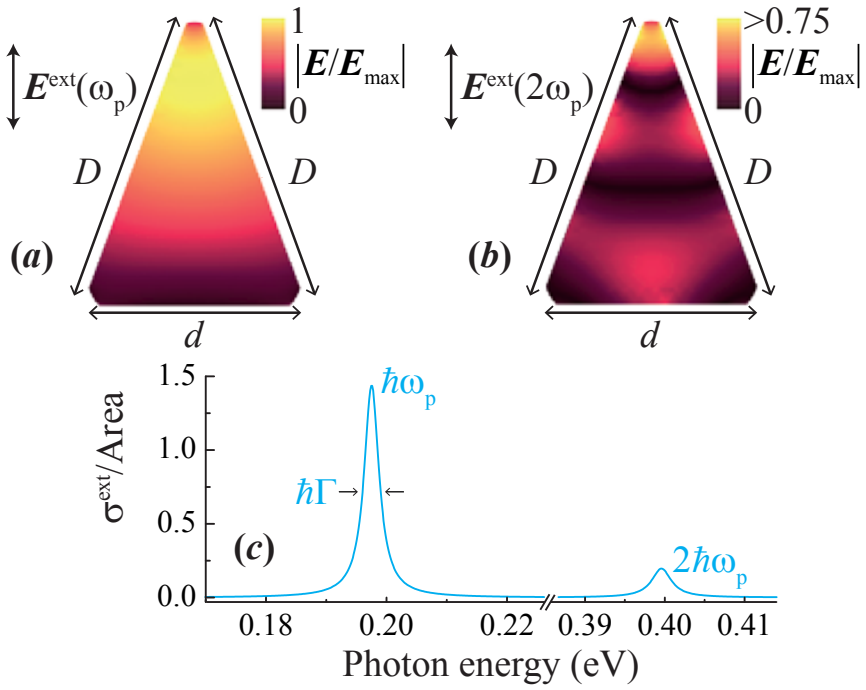

Figure 4.1: Plasmon modes in the graphene triangular nanoisland. (a), (b) Induced electric field distribution associated with the first (a) and second (b) harmonic modes, respectively. The graphene structure consists of an isosceles triangle with side lengths $D = 22\,\text{nm}$ and $d = 16.9\,\text{nm}$, and a doping level $E_F = 0.2\,\text{eV}$ with an intrinsic decay rate $\hbar\Gamma = 3\,\text{meV}$ (decay time $\sim$ 220 fs). (c) Extinction cross section normalized to the area ($S = 169.6\,\text{nm}^2$) of the triangles depicted in panels (a) and (b) with a strong fundamental dipolar mode and a secondary weaker dipolar mode.

not true for arbitrarily small structures, where quantum finite-size effects play a significant role, this approximation is already qualitatively correct for structures with $D \gtrsim 10\,\mathrm{nm}$ [177].

To show that a high overlap factor of $\beta \sim 1$ can be reached in typical structures, we consider one specific example of a doped graphene isosceles triangle embedded in vacuum. This choice enables a simple optimization to obtain the desired ratio of 2 between the SP mode frequencies. Indeed, we find that an aspect ratio $r = 1.3$ produces plasmons at frequencies ω_p and $2\omega_p$ (see Fig. 4.1). The modes shown in Fig. 4.1 are numerically computed using a commercial finite-difference code (COMSOL®) by driving the system with a plane wave whose associated external field $\mathbf{E}^{\mathrm{ext}}$ is polarized along the axis of symmetry of the triangle. We model the structure as a thin slab with rounded edges and a dielectric function $\epsilon = 1 + 4i\pi\sigma^{(1)}/\omega t$. The thickness t is chosen to be $t = 0.5\,\mathrm{nm}$ (this value is sufficiently small that the in-plane current has converged, and the results do not depend on the specific value), and the expression of $\sigma^{(1)}$ is given by the equation (4.8). Since the characteristic length of the structure is much smaller than the free-space wavelength, the response can be determined electrostatically, where the retardation and the response to the magnetic field are neglected. Furthermore, the ratio $1:2$ between the first and second plasmon resonances is preserved independently of the actual size of the triangle and the doping [178]. While the remaining parameters are somewhat arbitrary, as a numerical example, we consider the realistically achievable length and doping level of $D = 22\,\mathrm{nm}$ and $E_F = 0.2\,\mathrm{eV}$. For this choice, we observe a pronounced first harmonic mode (Fig. 4.1a,c) with energy $\hbar\omega_p \simeq 0.20\,\mathrm{eV}$, and a second harmonic resonance (Fig. 4.1b,c) twice as energetic. Once we obtain the mode profiles, their nonlinear coupling is evaluated using the equations (4.10) and (4.16). Numerical calculations for this structure yield a value of $\beta = 0.34$, hence the quantum oscillation rate g reaches a remarkable 1.25% value of the dipolar frequency ω_p.

Surface plasmons in realistic graphene structures generally decay by non-radiative mechanisms, whose precise nature is still under active investigation [77, 179, 180]. We thus use a phenomenological description associating an intrinsic decay rate Γ' to the modes. For our numerical calculations we will assume a mode quality factor of $Q = \omega_p/\Gamma$, where Γ is the total decay rate defined below, ranging from some tens to one hundred, close to what has been experimentally observed in nanostructures [77], although in our analytical results we will explicit keep track of the scaling with Γ.

In addition to intrinsic decay channels, graphene SPs can also be excited and detected through desirable channels, *i.e.* via radiative decay. We will use the notation $\kappa_{a,b}$ to indicate such decay rates. The total decay rate introduced in Hamiltonian (4.15) is thus $\Gamma_{a,b} = \Gamma'_{a,b} + \kappa_{a,b}$. We will also introduce the notation $\eta_{a,b}$ to indicate the external coupling efficiencies of the modes, defined as $\kappa_{a,b}/\Gamma_{a,b}$. For example, in our structure, the first and second harmonic modes radiate into free space at rates $\kappa_a \approx 2 \times 10^{-7}\omega_p$ and $\kappa_b \approx 5.4 \times 10^{-8}\omega_p$, as numerically calculated through the extinction cross sections of the incident field. The external coupling efficiency can be increased by using more sophisticated techniques, such as SNOM [76] or graphene nanoribbons [169].

4.4 OBSERVING AND UTILIZING THIS NONLINEARITY: CLASSICAL LIGHT

The rate of oscillation or internal conversion between a single quantized plasmon and two lower-frequency plasmons is remarkable, particularly considering that the state-of-the-art down-conversion efficiency in conventional nonlinear crystals is $\sim 10^{-8}$ [78, 181]. It should be pointed out that the internal conversion rate holds independently of how the plasmons are generated. Of course, for both practical observation and for technological relevance, it would be ideal if the plasmons could be efficiently excited and subsequently converted back into propagating photons (such as from free space, fiber, or other evanescent modes). Motivated by this, we now examine the coupling problem to propagating photons in more detail and investigate how their intermediate conversion and interaction as plasmons manifests itself as strong, effective nonlinearities between propagating photons.

Remarkably, the extinction cross section $\sigma^{ext} = (3/2\pi)\lambda_0^2\kappa/\Gamma$ of a single nano-structure, as that one of a single atom, can exceed its physical size. However, the low values of κ/Γ still imply that σ^{ext} is much smaller than the diffraction limited area λ_0^2 for free-space beams, indicating that such sources cannot be used to excite plasmons efficiently. In particular, it can be shown using time-reversal symmetry that the best in-coupling (excitation) efficiency that can be achieved is the same as the out-coupling efficiency, η [83]. The situation is illustrated schematically in Fig. 4.2. This raises an important conceptual question. On one hand, graphene plasmons seem to represent the "ultimate" quantum nonlinear optical device, capable of internal conversion at the single-photon level. However, very little incoming light enters the structure and turns into a plasmon, and

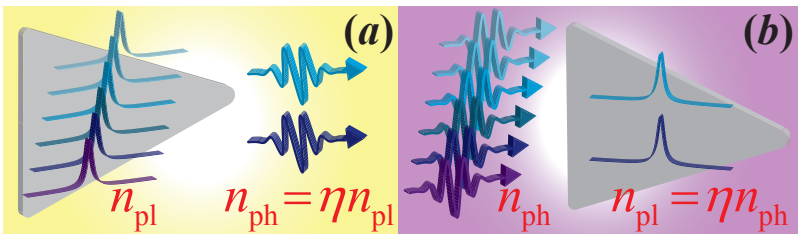

Figure 4.2: (a) A given plasmon mode radiates into free space (or more generally, into any desirable channel) with an efficiency characterized by η. (b) By time-reversal symmetry, incoming photons in the same spatial mode excite plasmons with the same efficiency. The efficiency η is related to the extinction cross section and free-space wavelength by $\eta = (2\pi/3)\sigma^{ext}/\lambda_0^2$.

vice versa, a small percentage of plasmons are radiated back into light. We now discuss various ways in which the strong quantum-level internal nonlinearities of graphene can be observed and utilized, given these limitations.

One way of increasing the coupling to radiation, which has already been discussed in the linear optical regime, is to exploit an array of nano-structures [77, 182]. Intuitively, since the extinction cross section of a single element can exceed its physical size, having a dense array extending over an area larger than λ_0^2 guarantees efficient interaction with an incoming beam. We thus proceed to consider the nonlinear interaction between an incoming radiation field with frequency ω_p resonant with the fundamental mode and an array of nano-structures, as illustrated in Fig. 5.1. We expect that the efficient coupling with an array will enable the incoming photons to excite plasmons at ω_p, internally convert to plasmons at $2\omega_p$, and then re-radiate into free-space as a second harmonic signal. We consider here a hexagonal lattice of nanostructures with lattice period $l = 50$nm. The array is illuminated at normal incidence with a field of frequency ω, and polarized along $\hat{x}$ to maximally drive the plasmon resonance (see Fig. 5.1).

From Hamiltonian (4.15) extended to include the coupling between the structures, we get the equations of motion of the

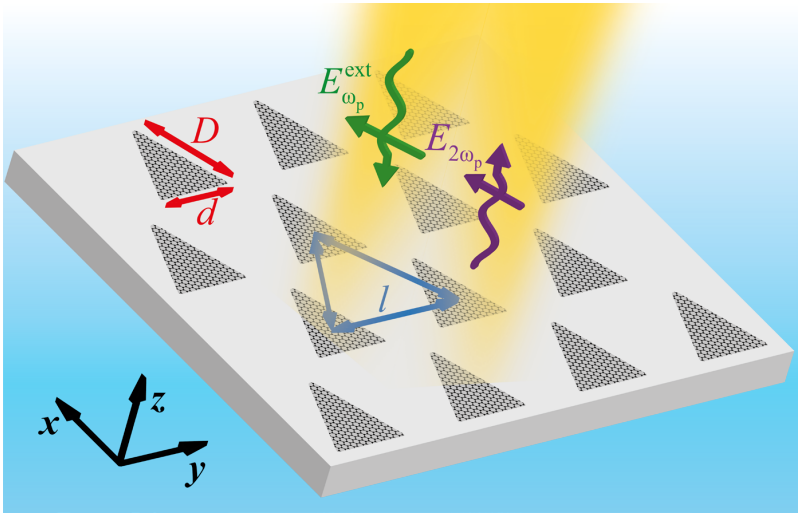

Figure 4.3: A hexagonal array of triangular nanostructures illuminated by laser light at normal incidence and frequency ω_p, resonant with the first plasmonic mode of the structures. The nonlinear coupling between this mode and the mode at frequency $2\omega_p$ generates an outgoing radiation field at this second harmonic, which is in a direction normal to the array.

operators for the first and second harmonic modes of structure j in the array are

$$\dot{a}_j = -i\left(\omega_p - i\Gamma_a/2\right) a_j - i\frac{p_a}{\hbar} E^{ext}_{\omega_p} - 2ig\, a_j^\dagger b_j + i\frac{p_a^2}{\hbar}\sum_l G^{\omega_p}_{jl} a_j, \tag{4.17}$$

$$\dot{b}_j = -i\left(2\omega_p - i\Gamma_b/2\right) b_j - i\frac{p_b}{\hbar} E^{ext}_{2\omega_p} - ig\, a_j^2 + i\frac{p_b^2}{\hbar}\sum_l G^{2\omega_p}_{jl} b_l, \tag{4.18}$$

where the last term in both equations accounts for the dipole-dipole interaction with other nanostructures l in the array. $G_{jl} = G(r_j, r_l)$ is the electromagnetic Green's function describing the field produced at position r_j by a dimensionless dipole oscillating at r_l assuming that all the dipoles have the same polarization (see Sec. 3.2 for a more detailed discussion of the electromagnetic Green's function), while $p_a = \sqrt{3\pi\epsilon_0\hbar\kappa_a c^3/\omega_p^3}$ is the modulus of the electric dipole moment of a single plasmon in the first mode (an equivalent expression holds for p_b at frequency $2\omega_p$). We have also included the possibility of driving either mode with classical free-space external fields, denoted by $E^{ext}_{\omega_p}$ and $E^{ext}_{2\omega_p}$.

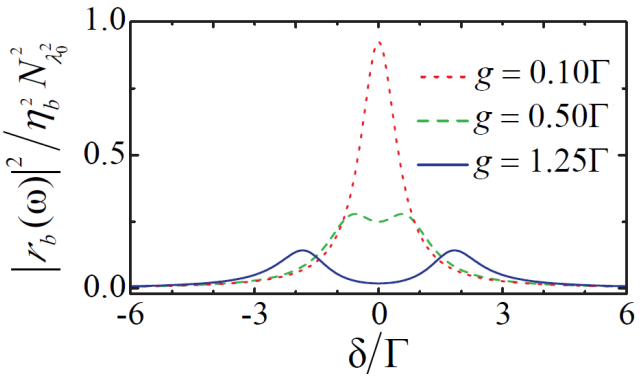

Figure 4.4: Back-scattered spectrum around $2\omega_p$. Reflectance curves for a weak driving field as a function of the detuning δ (in units of the total decay rate Γ) from the second mode of frequency $2\omega_p$, plotted for different values of the ratio g/Γ. The value of the solid curve corresponds to the ratio $g/\Gamma = 1.25$ that we have predicted theoretically for the structure presented in Fig. 4.1.

Before considering the generation of a second harmonic, it is already interesting to point out that the strong internal interactions between plasmons can manifest itself in the *linear* optical response to an incoming laser with frequency near the second mode $2\omega_p$. We proceed by solving the coupled system of equations (4.17) for a weak external driving field of frequency ω around $2\omega_p$. We consider specifically an approximation where edge effects are ignored (which becomes exact in the plane-wave limit and an infinite array), which makes the sum $\sum_l G_{jl}$ identical for each element. The effect of the Green function is to renormalize both the resonance frequencies and the losses, so that $\omega_p \to \tilde{\omega}_p, \Gamma_a \to \tilde{\Gamma}_a$, etc. We find that the linear reflection coefficient of the array is

$$r_b(\omega) = -\frac{i\kappa_b N_{\lambda_0^2}}{2} \frac{\tilde{\delta}_a + i\tilde{\Gamma}_a}{\left[\tilde{\delta}_a + i\tilde{\Gamma}_a\right]\left[\tilde{\delta}_b + i\tilde{\Gamma}_b/2\right] - 2g^2}, \tag{4.19}$$

where $\tilde{\delta}_a = \omega - 2\tilde{\omega}_p$ is the detuning of the input field with respect to two times the renormalized first harmonic SP frequency, and similarly for $\tilde{\delta}_b$. The quantity $N_{\lambda_0^2} = (3/2\pi)(\lambda_0/2)^2/A$ is proportional to the number of structures in a diffraction limited area λ_0^2, as A is the area of a unit cell in the array. In Fig. 4.4, we plot $|r_b(\omega)|^2$ as a function of the detuning for different values of the ratio Γ/g. Here we have ignored the renormalized detunings, $\tilde{\delta}_{a,b} \to \delta_{a,b}$, as the structure dimensions can be slightly altered to compensate for these shifts. We also take $Q = 100$ and $Q = 50$ for modes a and b, respectively. Note that if the nonlinear interaction between plasmons is negligible ($g \ll \Gamma$), the spectrum exhibits the typical Lorentzian peak associated

with a resonant scatterer. We observe a qualitative difference in the reflection curve passing from the regime $g < \Gamma/2$ to the regime in which $g > \Gamma/2$, which is characterized by the appearance of a splitting in the reflection curve. Importantly, while an efficient external coupling increases the peak reflection of the structure, the magnitude of the mode splitting $2\sqrt{2}g$ does not depend on the coupling efficiency and represents a robust signature of quantum strong coupling between the SPs modes. We also emphasize that Eq. (4.19) is only obtained by solving fully the Eqs. (4.17), including quantum correlations between the two plasmon modes. Solving the classical limit, in which all quantum operators are replaced with numbers, would produce a Lorentzian spectrum for any value of g, which reinforces the appearance of a mode splitting as a quantum signature.

In a similar way, we can calculate the intensity emitted at frequency $2\omega_p$, when the system is driven at frequency ω_p by a classical external field. We find that the SHG signal intensity radiated into the far field is approximately

$$I^{far}_{2\omega_p} \approx \frac{8g^2}{\hbar\omega_p {\Gamma_a}^2 \Gamma_b} \frac{[\sigma^{ext}_a]^2 \sigma^{ext}_b}{A^2} \left[I^{ext}_{\omega_p}\right]^2, \tag{4.20}$$

where $\sigma^{ext}_{a,b}$ are the extinction cross sections of the two modes. This expression is valid in the undepleted pump approximation, where the converted intensity is a small fraction of the incident. Using the previously quoted parameters for the triangular nanostructure, we find that a 1% conversion efficiency can be observed for the low driving intensity of roughly 10^8 Wm^{-2}.

While we have presented here a semi-classical calculation, in which the input fields are treated as classical numbers, it would be interesting to find what is the conversion efficiency at the single-photon level. In particular, it would be interesting to see how graphene compares to the state-of-the-art efficiencies of $\sim 10^{-8}$ in bulk crystals for SHG of just a two-photon input. For this purpose, in the next section we use an approach based on the S-matrix formalism.

4.5 QUANTUM FREQUENCY CONVERSION

In general, for a given few-photon input state, we wish to determine the effect of nonlinear interactions on the output. All of this information is contained in the S-matrix [90], which specifically describes the overlap amplitude between a set of monochromatic incoming and outgoing freely propagating photons. Because monochromatic photons form a complete basis, the S-matrix thus contains all information about photon dy-

namics. In particular, it can be used to determine how a wave packet consisting of a superposition of monochromatic photons (*i.e.* decomposed into frequency components) interacts with the graphene nanostructure.

A simple example of an S-matrix element consists of the linear reflection amplitude $r_b(k)$ of a single photon of frequency k_b, which interacts with the higher-frequency SP mode (mode b), which we have calculated in the previous section by solving the Heisenberg equations of motion. In the S-matrix language the reflection coefficient corresponds to the matrix element between an incoming photon propagating in one direction (say to the right) and a photon of the same frequency $p_b = k_b$ scattered in the other direction (to the left). More compactly, this relation is formally written as $\langle p_b^L | S | k_b^R \rangle \equiv r_b(k)\delta(k-p)$, where $\delta(k-p)$ denotes the Dirac delta function. Such an S-matrix element can be calculated by using standard input-output techniques [15, 90], which enable one to relate the outgoing field (after interaction) to the incoming field and internal dynamics of the nanostructure (governed by the Hamiltonian of Eq. (4.15)). We assume that the incoming photon is focused at the diffraction limit, $S \sim \lambda_0^2$, and interacts with $N \equiv N_{\lambda_0^2}$ structures. In particular, adopting the generalized input-output formalism presented in Chapter 2 we can show that the resulting reflection coefficient gives a result of the form of Eq. (4.19) [183].

Analogously, we can express the amplitude for the DC process as the S-matrix element between an incoming photon of frequency k_b near $2\omega_p$ and two outgoing photons of frequencies p_a, q_a near ω_p. For simplicity we study the case in which the incoming photon is a superposition of a photon coming from the right and one coming from the left so that we can avoid directional labels. We thus find for an array of N structures

$$\langle p_a, q_a | S | k_b \rangle = C \; r_b(k)\, r_a(p)\, r_a(q)\, \delta(k-p-q), \qquad (4.21)$$

where r_a, r_b are respectively the reflection coefficients for photons in mode a and b, and $C = 2Ng/\sqrt{2\pi\kappa_a^2\kappa_b}$.

The S-matrix also enables one to calculate the dynamics of an incoming pulse. In particular, assuming a single-photon input wavepacket with a Fourier transform given by $f(k)$, we find that the total DC efficiency is given by $P_{DC} = 1/2 \int dp\, dq\, |f(p+q)\, r_b(p+q)\, r_a(p) r_a(q)|^2$. For a near monochromatic resonant incoming photon, *i.e.* $|f(k)|^2 \approx \delta(k-2\omega_p)$, the result simplifies to

$$P_{DC} = \frac{16N^2\kappa_a^2\kappa_b\, g^2}{\Gamma_a[\Gamma_a\Gamma_b + 4g^2]^2}, \qquad (4.22)$$

where in this case $\Gamma = \Gamma' + N\kappa$. The value of the coupling constant that maximizes the probability of conversion is $g = \sqrt{\Gamma_a \Gamma_b}/2$, for which we have

$$P_{DC} = N^2 \left(\frac{\kappa_a}{\Gamma_a}\right)^2 \left(\frac{\kappa_b}{\Gamma_b}\right). \tag{4.23}$$

In general, we expect g to exceed the plasmon linewidth in the graphene nanostructure considered, so that the condition $g = \sqrt{\Gamma_a \Gamma_b}/2$ is satisfiable, in contrast to conventional materials with weak nonlinear coefficients. For what concerns the optimal number of nanostructures, we identify two limits, one of low external coupling efficiency in which the array-enhanced external coupling does not overcome the losses, *i.e.* $\kappa \ll \Gamma'$, and the opposite case in which $\kappa \gtrsim \Gamma'$. In the first limit, which is satisfied for the system parameters presented earlier, the total decay rate Γ is roughly independent of the number of structures N and $P_{DC}^{max} \approx N^2 \eta_a^2 \eta_b$ (we recall again that $\eta_{a,b} = \kappa_{a,b}/\Gamma_{a,b}$). It is clear that in this limit the use of an array of nanostructures is an efficient way to increase the conversion (which anyway remains much smaller than 1). For our system parameters, we find that $P_{DC}^{max} \approx 10^{-7}$, which compares favorably with state-of-the-art numbers $\sim 10^{-8}$, a surprising result considering that graphene is not a bulk nonlinear crystal. In the opposite limit of good external coupling we find that $P_{DC}^{max} = N^{-1} \eta_a^2 \eta_b$. This remarkable result indicates that ultimately, there is a fundamental inequivalence between using many structures to increase the (linear) response, and working to improve the coupling to just a single structure. In particular, in the limit of efficient coupling, the strong nonlinear interaction between plasmons becomes diluted by having multiple structures. Intuitively, this N^{-1} scaling can be understood from the complementary process of SHG (whose S-matrix is identical to DC, as shown later). Clearly, in order for two incoming photons to create a second harmonic, they must excite two plasmons in the same structure. However, with many structures, the probability that this occurs (*i.e.*, compared to exciting single plasmons in two different structures) falls like N^{-1}. We thus argue that the development of techniques [76, 169] to efficiently couple to single structures is of fundamental importance to take maximal advantage of the strong intrinsic nonlinear interactions between graphene plasmons.

It should further be noted that the created photon pairs are frequency-entangled (see Eq. (4.21)), as energy conservation requires that the sum of their frequencies equals that of the incoming single photon. Intuitively, one expects that the DC process remains efficient as long as the incoming pulse bandwidth σ is

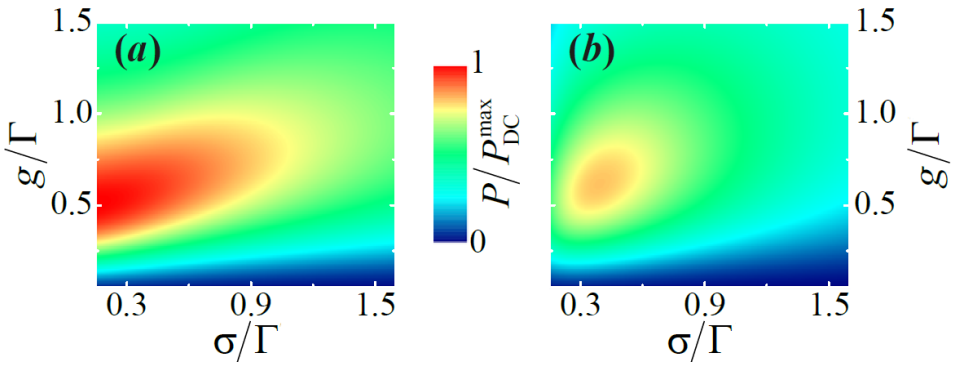

Figure 4.5: (a) Probability of DC for a photon in a Gaussian wavepacket of center frequency $2\omega_p$ and bandwidth σ. P_{DC} is plotted as function of σ and g (in units of Γ), and normalized with respect to P_{DC}^{max}. (b) Probability of SHG for a pair of uncorrelated photons in Gaussian wavepackets of center frequency ω_p and bandwidth σ, normalized as in (a).

smaller than the cavity linewidth Γ. This can be seen quantitatively in Fig. 4.5a, where Gaussian single-photon inputs with bandwidth σ are considered, *i.e.* $f(k) \propto e^{-(k-\omega_p)^2/4\sigma^2}$.

In SHG two photons with frequencies centered around ω_p are (partially) converted in a single photon of frequency $2\omega_p$. By the time reversal symmetry of the scattering matrix the relation $\langle p_a, q_a| S |k_b\rangle = \langle k_b| S |p_a, q_a\rangle^*$ holds. This implies that in principle, a maximum up-conversion efficiency of $P_{SHG}^{max} = P_{DC}^{max}$ can be achieved, but only if the two-photon input itself is an entangled state. In Fig. 4.5a, we consider the more realistic case of two identical, separate photons, each represented as a Gaussian pulse of width σ. It can be noticed the qualitatively different functional behavior of P_{DC} and P_{SHG}. The latter saturates at a lower value than the former and exhibits a maximum for a finite value of σ, going to zero for both the limits $\sigma \to 0$ and $\sigma \to \infty$. The inability to deterministically up-convert two separate photons ($P_{SHG} = 1$), even for perfect coupling efficiencies, notably deviates from the semiclassical prediction that perfect conversion can be achieved [176].

We conclude showing that a single graphene nanostructure can generate nonclassical light when irradiated with weak classical light at the lower frequency. We have seen above that in the strong quantum coupling regime, $g > \Gamma/2$, a mode splitting at the second resonance appears. Physically, this splitting arises because the nonlinear interaction given in the Hamiltonian of equation (4.15) strongly mixes a single photon $|0;1\rangle$ in mode $2\omega_p$ with two photons $|2;0\rangle$ in mode ω_p, as shown in Fig. 4.6b. The resulting eigenstates of the Hamiltonian are

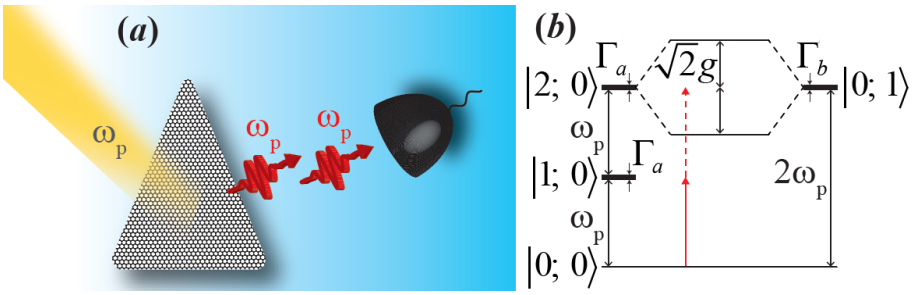

Figure 4.6: (a) Schematic showing the creation of non-classical light. A coherent state beam (yellow) of frequency ω_p incident on the graphene is scattered and produces anti-bunched light (red). (b) Energy level structure of the system, where the notation $|m, n\rangle$ indicates the occupation of m (n) plasmons in mode ω_p ($2\omega_p$). The dressed states generated by the coupling between $|2;0\rangle$ and $|0;1\rangle$ are also represented. Red arrows illustrate the origin of photon blockade. Due to the nonlinear coupling, the nominally degenerate states $|2;0\rangle$ and $|0;1\rangle$ hybridize into two dressed states with frequencies $2\omega_p \pm g/\sqrt{2}$. When the fundamental mode is resonantly driven, the population of that mode by a single photon (solid red arrow) blocks the excitation of a second photon (dashed red arrow), as the mode hybridization results in the absence of a state at $2\omega_p$.

symmetric and antisymmetric combinations $|0;1\rangle \pm |2;0\rangle$ with frequencies $2\omega_p \pm \sqrt{2}g$. The mode splitting creates an effective nonlinearity: once a single plasmon of frequency ω_p enters the system, the absence of a resonant state at $2\omega_p$ prevents a second plasmon from entering, creating a blockade effect [174]. This is a complementary signature of strong coupling observable in the lower mode. It can be quantified by considering the second-order correlation function of back-scattered photons (for instance left-propagating photons when the system is driven by right-propagating laser light)

$$g_a^{(2)}(t) = \frac{\langle a_{L,out}^\dagger(\tau) a_{L,out}^\dagger(\tau+t) a_{L,out}(\tau+t) a_{L,out}(\tau)\rangle}{\langle a_{L,out}^\dagger(\tau) a_{L,out}(\tau)\rangle^2}. \quad (4.24)$$

The output field itself is related to the input field and plasmon mode by the equation $a_{L,out} = a_{L,in} + \sqrt{\kappa_a/2}\, a$. However, as the left-going input field is in the vacuum state, the corresponding input operator has no effect. Thus the second-order correlation function can be written directly in terms of the plasmon mode a,

$$g_a^{(2)}(t) = \frac{\langle a^\dagger(\tau) a^\dagger(\tau+t) a(\tau+t) a(\tau)\rangle}{\langle a^\dagger(\tau) a(\tau)\rangle^2}. \quad (4.25)$$

For $t = 0$ this function indicates the relative probability to detect two photons at the same time. Values of $g^{(2)}(0) < 1$ indicate the presence of nonclassical light. In the limit of weak driving amplitude we find that

$$g_a^{(2)}(0) = \frac{\Gamma^2(16g^2 + 3\Gamma^2)}{3(4g^2 + \Gamma^2)^2}. \tag{4.26}$$

For $g = 0$ it acquires a value of $g_a^{(2)}(0) = 1$, reflecting the coherent state statistics of the laser, while exhibiting strong antibunching ($g_a^{(2)}(0) < 1$) when $g \gtrsim \Gamma/2$. It is particularly important that $g_a^{(2)}(0)$ is independent of the external coupling efficiency κ/Γ, thus making this effect a robust signature of strong quantum coupling between plasmon modes.

4.6 CONCLUSIONS

We have shown that second-order nonlinear optical interactions between plasmons in graphene nanostructures can be remarkably strong. Signatures of such nonlinearities should be immediately observable in experiments involving arrays of nanostructures, where incident free-space light can undergo frequency mixing at very low input powers via interaction with plasmons.

We further show that single nanostructures should exhibit the capability to generate non-classical states of light, observable even with low coupling efficiencies, which opens up a novel route to quantum optics as compared to the conventional approach of using atom-like emitters. With improved coupling efficiencies to the modes of these nanostructures, it would become possible to realize efficient second-harmonic generation or down-conversion at the level of a few quanta, which would exceed the capabilities of current systems by several orders of magnitude. While we focused on one concrete example consisting of a graphene nanotriangle, our conclusions are quite adaptable. Thus, it would be interesting to explore further the potential of this unique “nonlinear crystal" in a wide variety of classical and quantum nonlinear optical devices. It would also be interesting to investigate the nonlinear optical response of even smaller structures [184, 185], which is expected to deviate significantly from large-scale graphene due to quantum finite-size effects. Finally, we anticipate that our work will open up the intriguing possibility of a search for new materials that are capable of attaining the quantum nonlinear regime.

5

QUANTUM MEMORIES WITH ATOMIC ARRAYS

5.1 INTRODUCTION

One of the most highly explored potential applications for ensembles of atoms consists of a quantum memory of light, in which a quantum state of light can be "stored" and then retrieved on demand at a later time [20, 22, 79, 80]. Quantum memories form an important component of various protocols within quantum information processing, including quantum repeaters [186], single-photon sources [187, 188], and quantum logic operations between photons [189].

Different schemes have been proposed theoretically and demonstrated experimentally to realize quantum memories with atomic ensembles. The common idea is to reversibly convert a photon into a long-lived atomic excitation. For instance, EIT (see Sec. 2.4) can be used to convert a propagating photon into a slow-propagating dark-state polariton and then a completely stationary one [29], by changing dynamically the control field $\Omega(t)$. In a similar approach the photonic excitations are mapped into the metastable state of the atoms by stimulated Raman transitions keeping a large detuning of both the probe and control field in order to suppress the population of the fast-decaying excited state [81]. In the photon-echo approach the map to the metastable state is instead realized by mean of a fast resonant π pulse on the $|e\rangle - |s\rangle$ transition [82].

An important figure of merit is the storage (retrieval) efficiency, the probability that a photon can be mapped to an atomic excitation (or vice versa). A time reversal symmetry argument shows that the maximum efficiencies of these two processes are equal [83]. The approaches described above have several sources of error. For instance, in all of them the pulse is required to fit within the medium to get high-fidelity mapping of the photonic excitations into the atomic degrees of freedom. On the other hand, a pulse that is too short does not fit fully into the transparency window of EIT, and similarly cannot be absorbed by the atoms with the photon-echo technique [83]. An analysis of the efficiencies of these approaches has been done in Ref. [83] by Gorshkov and coauthors within a unified physical picture. There the storage and retrieval processes of the atomic ensemble have been studied using the Maxwell-Bloch equations (see Secs. 1.1.2 and 2.2.2), where the atomic distribution is mod-

elled by a continuous field. The propagation and interaction of a single transverse mode of light with the atoms is modelled by a quasi-1D wave equation, while the interaction of the atoms with the remaining free-space modes is accounted for heuristically via an effective, independent decay rate Γ' of the atomic population. Within this model it is predicted that the minimum error in the retrieval efficiency is $\epsilon \sim 5.8/\mathrm{OD}$, where OD is the optical depth of the atomic ensemble.

While the previous analysis serves as a faithful empirical model of free-space atomic ensembles with disordered atomic positions, recently it has become possible to realize atomic arrays of ordered positions with high fidelity [84, 85]. Much like how a phased antenna array can be used to achieve highly directed emission of radio waves, one might expect that in ordered atomic arrays the absorption and emission of light is highly affected by interference and the specific atomic positions. A spectacular example has been described theoretically in Ref. [190], where it has been predicted that an infinite 2D square lattice of atoms can act as a perfect mirror for resonant light at normal incidence, when the lattice constant of the array is smaller than the resonant wavelength, $d < \lambda_0$. This occurs because for such a lattice constant, all potential diffraction orders of light supported by the lattice become evanescent, enabling all of the incoming optical energy to be returned along the original propagation direction. Naively, this result seems to suggest that a 100% interaction probability between light and an atomic array is possible. Motivated by this observation, we are interested to functionalize this system, turning it from a passive mirror into a quantum memory, and to investigate the ultimate performance limits.

In this chapter we begin by presenting a formalism to calculate the retrieval efficiency of a single photon stored in an arbitrary atomic array, given only the spatial mode into which the photon is collected and the Green's function of the system. Our formalism builds upon the general spin model for atom-light interactions introduced in Sec. 3.2, which is an exact formulation that accounts for the discreteness of the atoms and interference in emission to all orders [86, 153]. We will show that when a specific mode for the detection is fixed, the initial conditions that maximize the retrieval efficiency, *i.e.* the initial distribution of the atomic excitation in the array, are given by an Hermitian matrix eigenvalue problem, in analogy with the continuum case [83]. We then apply the formalism to the case of a finite 2D square array of $N \times N$ atoms with a Gaussian-like detection mode (without assuming the paraxial approximation), finding that for an optimized beam waist the retrieval error

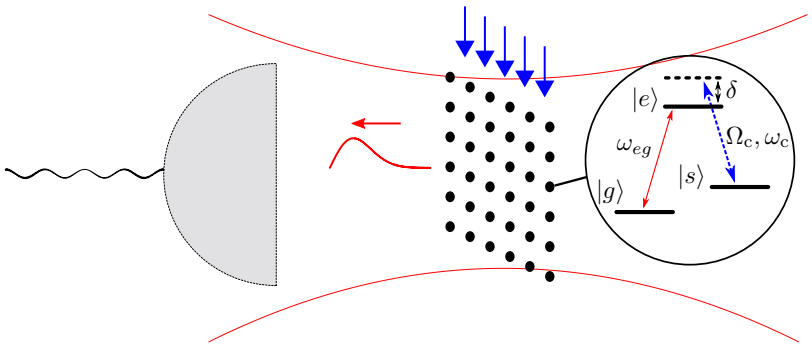

Figure 5.1: Schematic representation of a quantum memory realized with an atomic array. An excitation initially stored in the $|s\rangle$-manifold is retrieved as a photon by turning on the classical control field Ω_c (blue arrows), which then creates a Raman scattered photon from the $|g\rangle - |e\rangle$ transition. The photon is then detected in some given mode, illustrated here as a Gaussian beam.

scales as $\epsilon \sim (\log \sqrt{N_a})^2/N_a^2$. While there is no straightforward way to compare a single ordered layer of atoms with a continuous 3D atomic ensemble, it is nonetheless interesting to note that the error in the array decreases faster with atom number than the 3D ensemble case, $\epsilon \sim 5.8/OD \propto 1/N_a$, indicating the power that lies in exploiting strong interference.

5.2 THE SPIN MODEL RE-VISITED

In this section we describe how the dynamics of an arbitrary collection of atoms in free space, specified only by their discrete, fixed positions $\mathbf{r}_j$ (see Fig 5.1), can be related to the spin model described in Sec. 3.2. We consider three-level atoms with two ground states $|g\rangle$ and $|s\rangle$ and an excited state $|e\rangle$. We assume that the transition $|g\rangle - |e\rangle$ is coupled with a continuum of free space modes which includes the detection mode, while the transition $|s\rangle - |e\rangle$ is driven by a classical control field $\Omega_c(t)$ with frequency ω_c, which we assume to be homogeneous over the array. The formalism can be extended with little effort to the case of a modulated control field. We will focus our attention on the single excitation retrieval process in which an excitation is stored in the $|s\rangle$ manifold and then retrieved as a Raman scattered photon on the $|g\rangle - |e\rangle$ transition when the control field is turned on.

As we have seen in Secs. 2.2 and 3.2 the interaction of the $|g\rangle - |e\rangle$ transition with light (including re-scattering from other atoms) can be described by the effective spin model [151–153]

$$H_{\text{eff}} = -\mu_0 d_{eg}^2 \omega_{eg}^2 \sum_{j,l} \hat{\mathbf{d}}_j^* \cdot \mathbf{G}_0(\mathbf{r}_j, \mathbf{r}_l, \omega_{eg}) \cdot \hat{\mathbf{d}}_l \, \sigma_j^{eg} \sigma_l^{ge} = \\ = -3\pi\hbar\Gamma_0 \sum_{j,l} M_{jl} \sigma_j^{eg} \sigma_l^{ge}, \quad (5.1)$$

where $d_{eg}\hat{\mathbf{d}}_j$ is the dipole moment of atom j, and $\Gamma_0 = \mu_0 \omega_{eg}^3 d_{eg}^2 / 3\pi\hbar c$ is the single-atom spontaneous emission rate in vacuum. $\mathbf{G}_0(\mathbf{r}_j, \mathbf{r}_l, \omega_{eg})$ is the electromagnetic Green's function tensor in free space, which is the solution of the equation

$$\left[(\nabla \times \nabla \times) - \omega_{eg}^2/c^2\right] \mathbf{G}_0(\mathbf{r}, \mathbf{r}', \omega_{eg}) = \delta(\mathbf{r} - \mathbf{r}') \otimes \mathbf{I}. \quad (5.2)$$

The Green's function can be explicitly derived in free space, and takes the form

$$\mathbf{G}_0(\mathbf{r}_j, \mathbf{r}_l, \omega_{eg}) = \\ = \frac{e^{ik_0 R}}{4\pi R}\left[\left(1 + \frac{ik_0 R - 1}{k_0^2 R^2}\right)\mathbf{I} + \frac{3 - 3ik_0 R - k_0^2 R^2}{k_0^2 R^2} \frac{\mathbf{RR}}{R^2}\right], \quad (5.3)$$

where $R = |\mathbf{r}_i - \mathbf{r}_j|$ and k_0 is the wavevector associated with the resonant frequency ω_{eg}. In Eq. (5.1) we have defined for convenience the dimensionless matrix $M_{jl} = k_0^{-1} \hat{\mathbf{d}}_j^* \cdot \mathbf{G}(\mathbf{r}_j, \mathbf{r}_l, \omega_{eg}) \cdot \hat{\mathbf{d}}_l$. The Hamiltonian of Eq. (5.1) is non Hermitian, describing an open system where the excitations can be lost with the emission of photons into free space.

We want to study the dynamics of the atomic ensemble, when it initially contains a single metastable spin excitation $|\psi(t=0)\rangle = \sum_j c_j(t=0)\sigma_j^{sg}|g\rangle^{\otimes N_a}$. Formally, the dynamics of the retrieval process, where the spin flip $|s\rangle$ eventually gets mapped to a Raman scattered photon, is encoded in the dynamics of the wave function under the Hamiltonian $H = H_{\text{eff}} + H_c$, where the control field Hamiltonian $H_c = \sum_j (\Omega_j(t)\sigma_j^{es} + \text{H.c.})$. In order to calculate the efficiency of retrieval, we also need to be able to re-construct the spatio-temporal properties of the field E_{out} emitted by the array as the atoms evolve. Within the input-output formalism the emitted field can be reconstructed by the knowledge of the atomic states:

$$\mathbf{E}_{\text{out}}(\mathbf{r}) = \mathbf{E}_{\text{in}}(\mathbf{r}) + \frac{d_{eg} k_0^2}{\epsilon_0} \sum_{j=1}^{N} \mathbf{G}_0(\mathbf{r}, \mathbf{r}_j, \omega_{eg}) \cdot \hat{\mathbf{d}}_j \sigma_j^{ge}. \quad (5.4)$$

In the retrieval case the input field is vacuum, and can be dropped from Eq. (5.4) for our observables of interest.

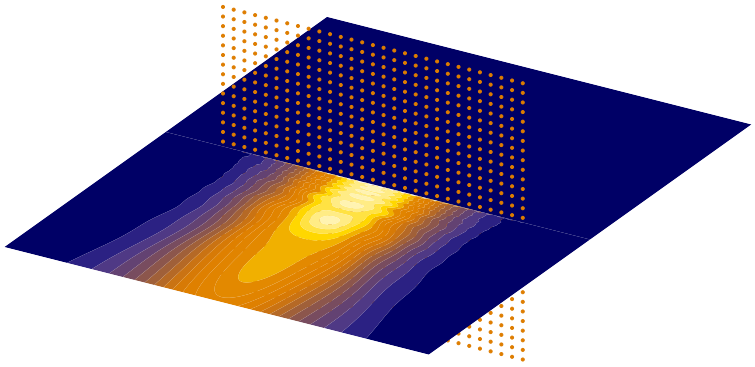

Figure 5.2: The total field produced by a 30×30 atomic array in the $x-y$ plane, when illuminated by a weak Gaussian beam normal to the array. The figure shows a cut of the field in the $y = 0$ plane. A nearly 100% reflectance of the Gaussian beam can be observed (with visible interference fringes between the incident and reflected fields), while transmission is highly suppressed. (Figure courtesy of Mariona Moreno-Cardoner.)

The input-output equation above enables the field to be calculated at any point $\mathbf{r}$, based upon the evaluation of an atomic correlation function $\sim \mathbf{G}_0(\mathbf{r}, \mathbf{r}_j, \omega_{eg}) \cdot \hat{\mathbf{d}}_j \sigma_j^{ge}$ weighted by the Green's function. It is certainly possible to build up the field everywhere in space, by re-evaluating the Green's function at each $\mathbf{r}$ and the corresponding atomic correlation function. An example is illustrated in Fig. 5.2. Here, a weak Gaussian beam drives a finite 30×30 array of two-level atoms on resonance, and the field is calculated in space to show the highly efficient reflection of the array (here the atomic wave function is calculated in the Schrödinger picture, truncated to a single excitation). This approach to field construction can be quite tedious, however, if many spatial points are taken. On the other hand, in experiments one often cares about the efficiency that the field can be collected into a specific spatial mode, such as a Gaussian. In the following section, we will show that the input-output equation can be projected efficiently into such a mode, so that only a single weighted atomic correlation function needs to be evaluated.

5.3 GAUSSIAN-LIKE DETECTION MODE

In this section we describe a concrete example of a detection mode, onto which the field emitted by the array is projected. A common and natural mode to project into is a Gaussian beam

shape. There is a technicality, however, since a Gaussian beam is only an approximate solution to Maxwell's equations (*i.e.* in the paraxial limit). While such an approximation suffices for most purposes, it is anticipated in our case that one can achieve nearly perfect storage and retrieval efficiencies. Thus, it is not obvious a priori that the small (actual) retrieval errors are not overwhelmed by the analysis error of the paraxial approximation itself. Thus, we first present an exact solution for Maxwell's equations, which approaches the Gaussian solution in the limit of large beam waist.

We choose a solution where the x-component of the electric field has a Gaussian distribution in wavevector space, while the y-component is identically zero. The value of the z-component is then determined by Maxwell's equations [191]. It is convenient to define the detection mode in the angular spectrum representation (ASR), which consists of an expansion in propagating and evanescent plane waves with fixed wavevector length k_0 and defined by $p = k_x/k_0$ and $q = k_y/k_0$ [192]. In this representation the mode electric field components are

$$E^x_{\text{det}}(p,q) = \frac{E_0}{2\pi} e^{-(p^2+q^2)k_0^2 w_0^2/4}\,\Theta(1-p^2-q^2), \tag{5.5}$$

$$E^y_{\text{det}}(p,q) = 0, \tag{5.6}$$

$$E^z_{\text{det}}(p,q) = -\frac{p}{m} E^x_{\text{det}}(p,q), \tag{5.7}$$

where $m = \sqrt{1-p^2-q^2}$ if $p^2+q^2 \leqslant 1$ or $m = i\sqrt{p^2+q^2-1}$ if $p^2+q^2 > 1$.

The real space profile of this mode is immediately obtained by Fourier transforming Eqs. (5.5)-(5.7):

$$\begin{aligned} E^x_{\text{det}}(\mathbf{r}) &= \int_{-\infty}^{+\infty} dp\,dq\, E^x_{\text{det}}(p,q)\, e^{ik_0(px+qy+mz)} = \\ &= E_0 \int_0^1 db\, b\, e^{-b^2k^2w_0^2/4}\, e^{ik_0 z\sqrt{1-b^2}}\, J_0(bk_0\rho), \end{aligned} \tag{5.8}$$

and

$$\begin{aligned} E^z_{\text{det}}(\mathbf{r}) &= -\int_{-\infty}^{+\infty} dp\,dq\, \frac{p}{m} E^x_{\text{det}}(p,q)\, e^{ik_0(px+qy+mz)} = \\ &= -iE_0 \frac{x}{\rho} \int_0^1 db\, \frac{b^2}{\sqrt{1-b^2}}\, e^{-b^2k_0^2w_0^2/4}\, e^{ik_0 z\sqrt{1-b^2}}\, J_1(bk_0\rho), \end{aligned} \tag{5.9}$$

where (ρ, z) are the cylindrical coordinates for $\mathbf{r}$, while J_0 and J_1 are Bessel's functions. Without the step function in Eq. (5.5), the corresponding field in real space would identically consist of a Gaussian in the focal plane with beam waist w_0. The step function removes evanescent field components, which in real space

enforces a diffraction limit, and distorts the beam to prevent a waist $w_0 \lesssim \lambda_0$. For large w_0 the mode tends to the paraxial solution, *i.e.* E^z_{det} vanishes and E^x_{det} assumes the form of a fundamental Laguerre-Gauss mode [192]. For this reason in the following we will loosely refer to w_0 as the beam waist of the mode. One can also expand the modes into the set of plane waves defined on the sphere of radius k_0 in wavevector space, with each of these plane waves having two possible orthogonal polarizations. Within this representation the detection mode considered is defined by

$$\mathbf{E}_{det}(\theta,\phi) = \frac{E_0}{2\pi k_0^2}\, e^{-\sin^2\theta k_0^2 w_0^2/2} \Big(\cos\theta\sin\phi, \cos\phi\Big)\,, \quad (5.10)$$

where the vector denotes the two components of the polarizations, which are orthogonal to $\mathbf{k}$ and between them.

This last representation is particularly convenient to calculate the normalization factor of the mode

$$\begin{aligned} F_{det} &\equiv \langle \mathbf{E}_{det}|\mathbf{E}_{det}\rangle = \int_{z=const} d^2\mathbf{r}\, \mathbf{E}^*_{det}(\mathbf{r})\cdot\mathbf{E}_{det}(\mathbf{r}) = \\ &= 4\pi^2 k_0^{-2}\int_0^{2\pi} d\phi \int_0^{\pi/2} d\theta \sin\theta\, \mathbf{E}^*_{det}(\theta,\phi)\cdot\mathbf{E}^*_{det}(\theta,\phi) = \\ &= \frac{\pi E_0^2}{k_0^2\beta^2}\left[1+\sqrt{2}\big(-\beta^{-1}+\beta\big)D_+(\beta/\sqrt{2})\right] \equiv \frac{\pi E_0^2 \tilde{F}_{det}(\beta)}{k_0^2}, \end{aligned} \quad (5.11)$$

where $\beta = k_0 w_0$, $D_+(z)$ is the Dawson's integral and we have defined the dimensionless function $\tilde{F}_{det}(\beta)$. The flux of energy of this mode, calculated for instance considering the surface integral of the z-component of the Poynting vector across the plane $z = 0$ [192], is given by

$$\Phi_{det} = 2\epsilon_0 c F_{det}. \quad (5.12)$$

Finally, we calculate the overlap between the field emitted by a collection of atoms and the detection mode. This can be done quite straightforwardly by expanding the electromagnetic Green's function in plane waves. We obtain

$$\langle \mathbf{E}_{det}|\mathbf{E}_{out}\rangle = \frac{i d_{eg} k_0}{2\epsilon_0}\sum_j \mathbf{E}^*_{det}(\mathbf{r}_j)\cdot\hat{\mathbf{d}}_j \sigma_j^{ge}, \quad (5.13)$$

a result that can be generalized to an arbitrary detection mode, and shows that the overlap depends only on the values of the electric field of the detection mode at the positions of the emitters. In particular, it has the nice property that only a single weighted atomic operator needs to be evaluated, in order to calculate emission into the mode of interest.

5.4 RETRIEVAL EFFICIENCY

We now turn to the question of the retrieval efficiency of a quantum memory, and we derive a prescription that enables one to find a strict upper bound for the efficiency, given a particular atomic spatial configuration and detection mode. As mentioned in the introduction, the retrieval efficiency is defined as the ratio between the total energy emitted in the detection mode and the energy $\hbar\omega_{eg}$ that must be emitted in the form of a Raman scattered photon. The retrieved energy is the time integral of the intensity in the detection mode during the retrieval process $I_{ret}(t) = (\Phi_{det}/F_{det})|\langle \mathbf{E}_{det}|\mathbf{E}_{out}(t)\rangle/\sqrt{F_{det}}|^2$, so that we can express the efficiency as

$$\eta = \frac{1}{\hbar\omega_{eg}}\int_0^\infty dt I_{ret}(t) = \frac{1}{\hbar\omega_{eg}}\frac{\Phi_{det}}{F_{det}}\int_0^\infty dt\left|\frac{\langle \mathbf{E}_{det}|\mathbf{E}_{out}(t)\rangle}{\sqrt{F_{det}}}\right|^2. \tag{5.14}$$

For the case of the detection mode introduced in the previous section we can use Eqs. (5.11), (5.12) and (5.13) in the last equation obtaining

$$\eta = \frac{3\Gamma_0}{2\tilde{F}_{det}(k_0 w_0)}\sum_{j,l} U_j U_l^* \int_0^\infty dt\, \sigma_j^{ge}(t)\sigma_l^{eg}(t), \tag{5.15}$$

where we have defined the dimensionless vector $U_j = \mathbf{E}^*_{det}(\mathbf{r}_j)\cdot\hat{\mathbf{d}}_j/E_0$ as the relative amplitude of the mode seen locally at each atomic position $\mathbf{r}_j$.

From H we obtain the equations of motion of the coherence operators:

$$\dot{\sigma}_j^{ge} = i\delta\sigma_j^{ge} - i\Omega(t)\sigma_j^{gs} + 3\pi i\Gamma_0\sum_l M_{jl}\sigma_l^{ge} \tag{5.16}$$

$$\dot{\sigma}_j^{gs} = -i\Omega(t)\sigma_j^{ge}, \tag{5.17}$$

with $\delta = \omega_c - \omega_{es}$. As discussed in detail in Ref. [153], since the matrix M is symmetric rather than Hermitian, its eigenvalues λ_ξ are complex and its eigenmodes $\mathbf{v}_\xi$ are non orthogonal in the quantum mechanics sense, but obey the orthogonality and completeness conditions $\mathbf{v}_\xi^T\cdot\mathbf{v}_{\xi'} = \delta_{\xi\xi'}$ and $\sum_\xi \mathbf{v}_\xi\mathbf{v}_\xi^T = I$. In this basis the equations of motion decouples into N_a pairs:

$$\dot{\sigma}_\xi^{ge} = i(\delta + 3\pi\Gamma_0\lambda_\xi)\sigma_\xi^{ge} - i\Omega(t)\sigma_\xi^{gs} \tag{5.18}$$

$$\dot{\sigma}_\xi^{gs} = -i\Omega(t)\sigma_\xi^{ge}, \tag{5.19}$$

where $\sigma_\xi^{ge,gs} = \sum_j v_{\xi,j}\sigma_j^{ge,gs}$. From these equations, and the assumption that the control field is turned on for a time long enough such that all the excitation leaves the system (so that all

the atoms end up in the ground state at $t = \infty$), one can derive the following equality

$$\int_0^\infty dt\, \sigma_j^{ge}(t)\sigma_l^{eg}(t) = \\ = \frac{i}{3\pi\Gamma_0} \sum_{\xi,\xi'} \nu_{j,\xi}\nu^*_{l,\xi'}(\lambda_\xi - \lambda^*_{\xi'})^{-1}\sigma^{gs}_\xi(0)(\sigma^{gs}_{\xi'}(0))^*. \quad (5.20)$$

Using this result in Eq. (5.15) we find

$$\eta = \frac{1}{2\pi\tilde{F}_{det}(k_0 w_0)} \sum_{j,l} \sigma^{gs}_{j,in} K_{jl} (\sigma^{gs}_{l,in})^*, \quad (5.21)$$

where

$$K_{jl} = i \sum_{\xi,\xi'} \nu_{j,\xi}\nu^*_{l,\xi'} \frac{U_\xi U^*_{\xi'}}{\lambda_\xi - \lambda^*_{\xi'}}, \quad (5.22)$$

where $U_\xi = \sum_m \nu_{\xi,m} U_m$. While the last two equations may appear cumbersome, they have actually a simple interpretation. It is immediate to verify indeed that K is an $N_a \times N_a$ Hermitian matrix which depends only on the positions of the atoms, the Green's function and the detection mode, but not on the specific time dependence of the control field. The maximum retrieval efficiency is thus given by the initial configuration corresponding to the eigenvector of K with the largest eigenvalue.

5.5 TWO-DIMENSIONAL ARRAY

In this section we apply the results of the previous sections to the case of a two-dimensional square atomic array with lattice constant d. As said in the introduction, an infinite 2D square array can act as a perfect mirror for incoming light at normal incidence when its lattice constant is smaller than the wavelength λ_0 associated with the atomic transition frequency [190]. Indeed, under such conditions the polarization created by the incoming light produces a field that is evanescent at all diffraction orders except that perpendicular to the plane. Then, the transmission is suppressed because of destructive interference with the input field, with all the energy back-scattered, in the same way a two-level system perfectly coupled with a 1D waveguide reflects a resonant photon travelling in the waveguide [120]. For light incident at an angle θ with respect to the normal, the array provides complete reflection if $\theta < \theta_{crit}(d/\lambda_0)$. The critical angle reaches the value of $\pi/2$ when the lattice constant d is smaller than $\lambda_0/2$, meaning that complete reflection is achieved at every angle of incidence [190]. It should be noted, however, that

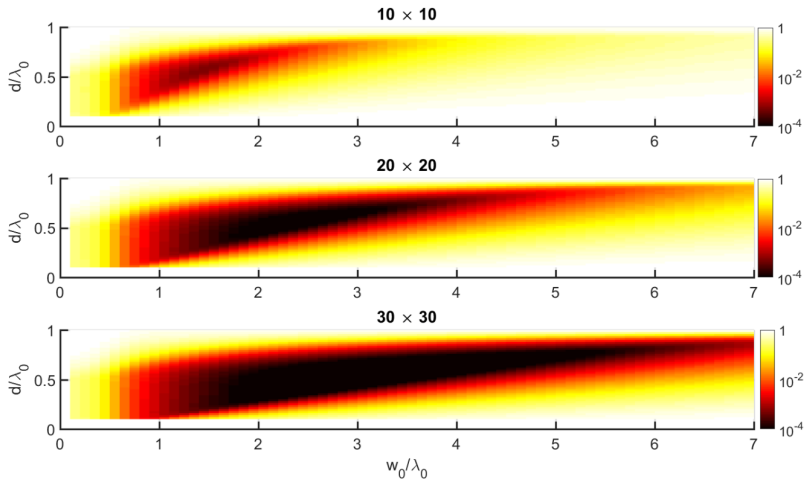

Figure 5.3: Minimum retrieval error as function of the lattice constant d and the beam waist w_0 for three different numbers of atoms.

this mirror is not broadband. In particular, 100% reflectance is only achieved at one particular incident frequency (close to ω_{eg}), and whose value varies with θ.

As a consequence, when an excitation is stored uniformly in the infinite array with $d < \lambda_0$, the retrieved photon is emitted symmetrically in the two directions normal to the array with unit efficiency. However, this is an highly idealized situation, since in the real world no infinite atomic array nor plane wave detectors are at one's disposal. In the following we analyse the retrieval efficiency of an $N \times N$ array, assuming that the detection mode is that introduced in the previous section. Through all the section we assume that the array lies in the focus plane of the detection mode, with its center on the axis of the mode.

To understand how the retrieval efficiency can decrease when using a finite array it is helpful to first think to the reflectance problem. Here, if the beam waist w_0 is too large with respect to the array dimensions, then part of the incoming light will not see the atoms and will be transmitted or scattered in other directions by the edges of the array. If w_0 is too small, the incoming mode will contain a broad range of wavevectors with different propagation directions. Since different angles have maximum reflectance at different detunings, the overall reflectance for a monochromatic photon will be reduced. For a given array there is thus an optimal value of the input mode beam waist that maximizes the reflectance of an incoming photon (at optimal detuning). The situation is analogous for the retrieval problem, where the optimization over the photon frequency is replaced by an optimization over the initial distribution of the excitation, as discussed in the previous section. This is evident from Fig. 5.3

(a)

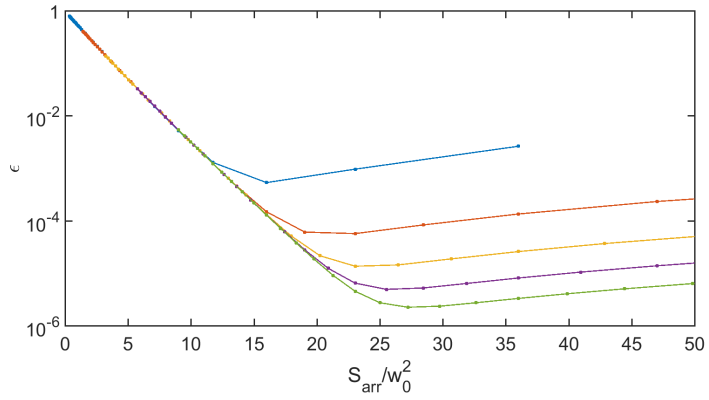

(b)

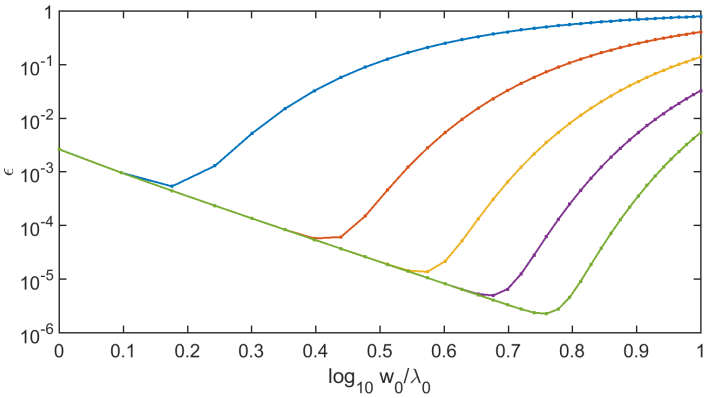

Figure 5.4: Minimum retrieval error as function of (a) S_{arr}/w_0^2, with $S_{arr} = d^2 N_a$ and (b) $\log_{10} w_0/\lambda_0$ for $d = 0.6\lambda_0$ and $N = 10, 20, 30, 40, 50$ (different colors).

where the minimum retrieval error, *i.e.* the error of the optimal initial spin excitation configuration, is plotted as function of d and w_0 for three different arrays 10×10, 20×20 and 30×30. There it is possible to see that, as expected, 1) for constant d and w_0 the error decreases as the array size N is increased, 2) for constant d and N there is an optimal value of the beam waist, and 3) for constant w_0 and N there is an optimal value of $d < \lambda_0$.

Here we look more in detail at the way the minimum error scales with the different parameters. In Fig. 5.4a we plot the error (in linear-log scale) as a function of the ratio between the array area $d^2 N_a$ (with $N_a = N^2$) and the square of the beam waist w_0. It can be shown that when this ratio is not too big the error is $\epsilon \approx 1 - \mathrm{Erf}^2(Nd/\sqrt{2}w_0)$, where $\mathrm{Erf}(x)$ is the error function. This result is not unexpected, since it corresponds to the fraction of the energy of the detection mode associated with the area outside of the array. In Fig. 5.4b we plot in log-

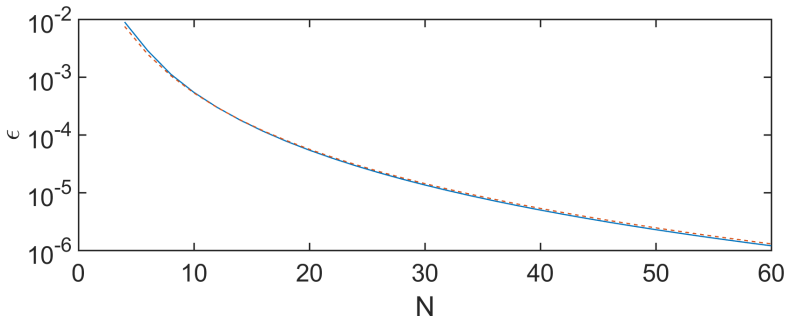

Figure 5.5: Minimum retrieval error optimized with respect to the beam waist w_0. The blue line is the value from numerical optimization, the red dashed line the approximated analytical value given by Eq. (5.24).

log scale the retrieval error as function of the ratio between w_0 and λ_0 (for values larger than one), again for different array sizes. We can see that up to a point where the beam waist becomes comparable with the array dimension, the error scales as $\epsilon \approx (\lambda_0/w_0)^4$. As anticipated, this error comes from the range of wavevector components that make up the detection mode, which is inversely proportional to w_0, as clear from Eq. (5.10). The exact scaling behaviour can be derived more easily by considering the reflectance problem of an infinite array. There one can expand the reflection coefficient as a function of θ, obtaining the quartic scaling of the reflectance error. The same mechanism gives the quartic scaling of the retrieval error. Overall we have that the minimum error can be approximated by the expression

$$\epsilon(N, d, w_0) \approx C/d)(\lambda_0/w_0)^4 + 1 - \mathrm{Erf}^2(dN/\sqrt{2}w_0), \quad (5.23)$$

where C depends on d and can be obtained by fitting the error: we find $C \approx\approx 0.0024$ for $d = 0.6\lambda_0$.

One can use Eq. (5.23) to find the optimal beam waist. After optimizing w_0 we find that that the leading term for the error is given by

$$\epsilon_{\mathrm{opt}} \sim (\log \sqrt{N_a})^2/N_a^2 \quad (5.24)$$

In Fig. 5.5 the approximated analytical value for the optimized minimum retrieval error is compared with the value obtained by numerical optimization. Interestingly, the figure indicates that even a 4×4 array of atoms can in principle already enable a storage/retrieval efficiency of above 99%.

One useful feature of our technique for calculating retrieval efficiency is that it readily enables different spatial configurations to be studied. Thus, we can easily include imperfections

such as the absence of atoms (*i.e.*, "holes") in the array, or classical disorder in the positions. We first examine the case of holes in the array. Averaging over many configurations and (low) densities of holes, we find statistically the relation

$$\eta_{\mathrm{def},\{j\}} \sim \eta\left(1-\alpha\frac{\sum_{\{j\}}|U_j|^2}{\sum_l|U_l|^2}\right), \tag{5.25}$$

where $\eta_{\mathrm{def},\{j\}}$ is the optimized retrieval efficiency for an array with missing atoms at positions $\{j\}$, while η is the optimized retrieval efficiency of a perfect array. Eq. (5.25) connects the loss of efficiency with the portion of energy of the detection mode associated with the missing atom, establishing a direct proportionality between the two quantities. Since U_i decreases exponentially with the distance from the center of the beam (and thus of the array), the magnitude of the relative retrieval error introduced by the defect can range several orders of magnitude. We find that the constant of proportionality α in Eq. (5.25) depends only on d and is about 1.25 for $d = 0.6\lambda_0$.

Classical disorder for the atomic positions consists in having the atoms displaced by random amounts $\delta_j = (\delta_{x,j}, \delta_{y,j})$ from their position in the perfect lattice. It is shown in Ref. [190] for the case of the reflectance of an infinite array that, when the δ's are extracted from a Gaussian distribution with standard deviation σ, then the decrease in reflectance introduced by the disorder scales as σ^2/d^2. We find numerically the same result for the retrieval error. In particular, in Fig. 5.6 the error introduced by the disorder is plotted as function of σ for different arrays dimensions and fixed lattice constant. This error is defined as the difference between the optimized maximum retrieval efficiency η, *i.e.* optimized with respect to the initial excitation distribution and with the optimal value of the beam waist, and the mean retrieval efficiency η_{dis} (sampled over many configurations) with the same initial conditions and beam waist but with disorder in the atomic positions. A study of the effect of local (quantum) motion on the retrieval efficiency will be left to future work.

5.6 CONCLUSION

In summary, in this chapter we have introduced a compact formalism to calculate the efficiency of a quantum memory realized with an atomic ensemble. We have considered the conventional three-level atom quantum memory, and defined a realistic detection mode over which the emitted field is projected. In our analysis, we explicitly account for the atomic positions, and solve for the resulting interference in emission exactly. In

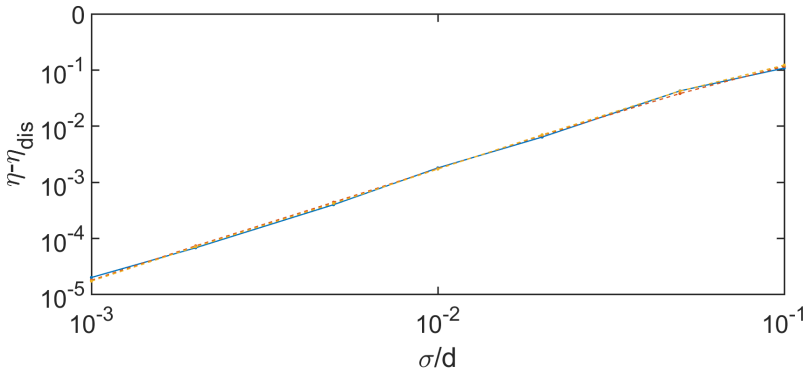

Figure 5.6: Difference between the optimized maximum retrieval efficiency η and the mean retrieval efficiency η_{dis} obtained using with the same initial conditions and beam waist but with disorder in the atomic positions (log-log scale). The different colors correspond to $N = 10, 20, 30$, with $d = 0.6\lambda_0$ in all cases.

the previous studies [83], on the contrary, the emission into modes other than the detection mode has been always treated under the assumption of being independent of atomic correlations. We show that in a 2D array, interference effects can lead to highly efficient memories even for relatively small numbers of atoms, and that the scaling of the efficiency significantly differs with atom number than a disordered 3D atomic ensemble. This work should hopefully stimulate a broad examination of the potential of atomic arrays for quantum optics applications.

Part III

APPENDIX

A

MATRIX PRODUCT STATES (MPS)

In the first section of the Appendix we review in greater detail the concept of matrix product states [131], which is at the basis of the algorithm we presented in Chapter 2 for the time evolution of the spin model in the regime of high intensity input. In the second section we present briefly the DMRG-MPS algorithm that we have used in Chapter 3 to obtain the ground state of the Hamiltonian of the photonic crystal waveguide-atoms system studied.

A.1 MATRIX PRODUCT STATES

A system of N particles, each with d possible states, can assume d^N configurations. The generic state of the system consists of a superposition of all these configurations, and thus requires d^N coefficients to be defined. This exponential growth of the Hilbert space with the number of particles poses a big obstacle to the numerical study of quantum many-body systems. Recently, it has been realized that in many problems of interest the relevant states of the system are not spread over all the Hilbert space, but occupy a small corner of it whose dimension is not exponential in N, as we will see below.

Here we will focus only on one-dimensional spin systems, whose generic wave function is

$$|\psi\rangle = \sum_{\sigma_1 \ldots \sigma_i \ldots \sigma_N} c_{\sigma_1 \ldots \sigma_i \ldots \sigma_N} |\sigma_1\rangle \ldots |\sigma_i\rangle \ldots |\sigma_N\rangle \,, \tag{A.1}$$

where c is a d^N-dimensional tensor containing all the coefficients of the basis states $|\sigma_1\rangle \ldots |\sigma_i\rangle \ldots |\sigma_N\rangle$. Formally, one can reshape the tensor as a matrix $\Psi_{\sigma_1,(\sigma_2 \ldots \sigma_N)}$, where rows are indexed by σ_1 and the columns by the collective index $(\sigma_2 \ldots \sigma_N)$, and perform a singular value decomposition (SVD) on it. The result is

$$c_{\sigma_1 \sigma_2 \ldots \sigma_N} = \sum_{a_1}^{r_1} U_{\sigma_1, a_1} S_{a_1, a_1} (V^\dagger)_{a_1, (\sigma_2 \ldots \sigma_N)} \equiv \sum_{a_1}^{r_1} A^{\sigma_1}_{a_1} c_{a_1, \sigma_2 \ldots \sigma_N}, \tag{A.2}$$

where $r_1 \leqslant d$ is the rank of the decomposition. In an SVD, U and V take the form of unitary matrices, while S is a diagonal matrix with real, non-negative entries (the singular values). In

the last step we have multiplied S and $V^\dagger$ and reshaped the resulting matrix into a tensor. We also have reshaped the matrix U_{σ_1,a_1} into a collection of vectors A indexed by σ_1 for reasons that will be clearer below. Similarly, one can reshape the tensor $c_{a_1,\sigma_2\ldots\sigma_N}$ as the matrix $c_{(a_1,\sigma_2)(\sigma_3\ldots\sigma_N)}$ and perform an SVD, obtaining

$$c_{\sigma_1\sigma_2\ldots\sigma_N} = \sum_{a_1}^{r_1}\sum_{a_2}^{r_2} A^{\sigma_1}_{a_1} U_{(a_1\sigma_2),a_2} S_{a_2,a_2} (V^\dagger)_{a_2,(\sigma_3\ldots\sigma_N)} = \\ = \sum_{a_1}^{r_1}\sum_{a_2}^{r_2} A^{\sigma_1}_{a_1} A^{\sigma_2}_{a_1,a_2} c_{a_2,\sigma_3\ldots\sigma_N}, \quad (A.3)$$

where $r_2 \leqslant dr_1 \leqslant d^2$. Going on with such operations one can rewrite the state as

$$|\psi\rangle = \sum_{\sigma_1\sigma_2\ldots\sigma_N} A^{\sigma_1} A^{\sigma_2} \ldots A^{\sigma_N} |\sigma_1\rangle |\sigma_2\rangle \ldots |\sigma_N\rangle, \quad (A.4)$$

where the A^{σ_i}'s are matrices whose multiplication is implicit (*i.e.* we have suppressed the indices $a_1, a_2, \ldots$).

Each state in the Hilbert space can thus be written in the form of Eq. (A.4), *i.e.* as a matrix product state. It is easy to see that the maximum dimension of the matrices A's increases exponentially (*i.e.* $(1 \times d)$, $(d \times d^2)$, $(d^2 \times d^3)$,...), as one can expect from the fact that no approximation has been performed. These matrices satisfy the orthogonality relation

$$\sum_{\sigma_\iota} A^{\sigma_\iota\dagger} A^{\sigma_\iota} = I, \quad (A.5)$$

and are said to be *left-normalized*. Starting the decomposition of the tensor c from the last spin N instead one can find an MPS representation of the state

$$|\psi\rangle = \sum_{\sigma_1\sigma_2\ldots\sigma_N} B^{\sigma_1} B^{\sigma_2} \ldots B^{\sigma_N} |\sigma_1\rangle |\sigma_2\rangle \ldots |\sigma_N\rangle, \quad (A.6)$$

in terms of matrices B's satisfying the orthogonality relation

$$\sum_{\sigma_\iota} B^{\sigma_\iota} B^{\sigma_\iota\dagger} = I. \quad (A.7)$$

These matrices are said to be *right-normalized*. Because of the different properties of matrices A's and B's, the MPS in Eq. (A.4) is said to be in the *left-canonical* form, while the MPS in Eq. (A.6) in the *right-canonical* form.

The most important form of an MPS is the mixed-canonical one, where the decomposition discussed above is performed

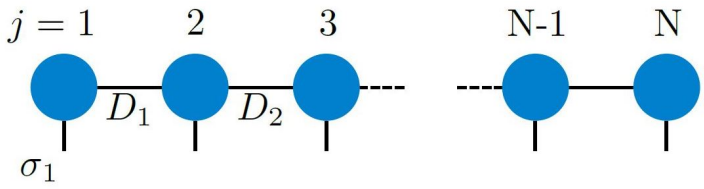

Figure A.1: Graphical representation of a matrix product state.

from the left until the site l and from the right until site $l+1$, obtaining

$$|\psi\rangle = \sum_{\sigma_1\sigma_2\ldots\sigma_N} A^{\sigma_1}\ldots A^{\sigma_l} S B^{\sigma_{l+1}}\ldots B^{\sigma_N} |\sigma_1\rangle |\sigma_2\rangle \ldots |\sigma_N\rangle . \quad (A.8)$$

The importance of this decomposition lies in the fact that it corresponds to a Schmidt decomposition of the state $|\psi\rangle$ as

$$|\psi\rangle = \sum_{a_l} S_{a_l} |a_l\rangle_A |a_l\rangle_B , \quad (A.9)$$

with the matrix S containing the Schmidt coefficients, which reveal the degree of entanglement between the two sub-systems A and B that the system has been divided into.

The Schmidt decomposition can be used to approximate the state $|\psi\rangle$ with an MPS having matrices of reduced dimensions. If it were indeed possible to really perform the SVD on the full state, one can imagine to progressively truncate the matrices (taking $a_l \leqslant D$ in Eq. (A.9)). In this way one would obtain a truncated MPS

$$|\psi\rangle_{\text{trunc},D} = \sum_{\sigma_1\sigma_2\ldots\sigma_N} C^{\sigma_1} C^{\sigma_2}\ldots C^{\sigma_N} |\sigma_1\rangle |\sigma_2\rangle \ldots |\sigma_N\rangle , \quad (A.10)$$

where the matrices C^{σ_l} have at most dimension $D \times D$. If the truncation error decreases exponentially when D is increased, then the state $|\psi\rangle$ has an efficient MPS approximation. In typical problems the state $|\psi\rangle$ (which can be a ground state, a particular excited state, or a state resulting from time evolution) is unknown. The MPS ansatz consists then of finding the best approximation to the state in the family of MPS denoted by D, where D is limited by the computational power and memory at disposal. While for some problems it has been proven rigorously that the states of interest have an MPS representation

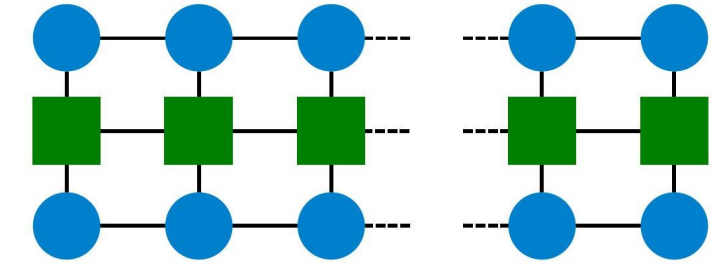

Figure A.2: Graphical representation of the expectation value of an operator in the MPO form on a state in the form of an MPS.

[131], in many other cases the validity of the ansatz has to be justified *a posteriori*, such as by explicitly monitoring the truncation error.

Matrix product states can be represented graphically by associating each site with a box. Each box, except the first one and the last one have three legs, one denoting the physical index σ_i and the other two denoting the virtual (or bond) indices. The contraction over virtual indices, *i.e.* the multiplication between the matrices, is denoted by linking the legs for neighbouring sites, as represented in Fig. A.1. This representation does not distinguish between left- and right-canonical MPS, but this information can be easily included by changing the shapes or the color of the boxes for each tensor according to its normalization.

The concept of matrix product states can be generalized to operators. An operator acting on the N-site system, for instance the Hamiltonian, can be decomposed as

$$H^{\sigma'_1 \ldots \sigma'_N}_{\sigma_1 \ldots \sigma_N} = O^{\sigma'_1}_{\sigma_1} O^{\sigma'_2}_{\sigma_2} \ldots O^{\sigma'_N}_{\sigma_N}, \tag{A.11}$$

where the O's are sets of matrices indexed by the physical indices σ_l and σ'_l, or equivalently tensors of rank four. An operator decomposed in this form is called a matrix product operator (MPO). The graphical representation of an MPO is similar to that of an MPS but with four legs for each tensor corresponding to the two physical indices and the two virtual ones. The graphical representation is quite insightful when it comes to multiplying operators and states in the form of MPO's and MPS's. For instance, in Fig. A.2 we pictorially represent the expectation value of the energy, $\langle \psi | H | \psi \rangle$, as a tensor contraction of the MPS of the state and the MPO of the Hamiltonian. Here,

the vertical lines represent the contractions of the physical indices.

A.2 GROUND STATE SEARCH: MPS-DMRG

A revolution in the study of quantum many-body one-dimensional systems occurred with the invention of the density matrix renormalization group (DMRG) algorithm in 1992 [193, 194]. This algorithm permits one to calculate the ground state of many relevant 1D models with extremely high precision and low computational effort.

About ten years after the introduction of DMRG, it was realized that the algorithm can be reformulated completely in terms of MPS [131]. For finite systems the MPS formulation consists of an optimization problem over a given family of MPS (denoted by the maximum virtual dimension D of its tensors), that means to find $|\psi\rangle = |\psi\rangle^{D}_{MPS}$ which minimizes the Hamiltonian expectation value $\langle\psi|H|\psi\rangle$. The simplest version of the algorithm does the optimization in the following way. First H is expressed as an MPO, and an MPS of the decided dimensions is initialized (randomly or to some educated guess), *i.e.* an object like that of Fig. A.2 is built. All the tensors of the MPS except that one corresponding to the first site A^{σ_1} are fixed and an optimization over the elements of this tensor is performed. A^{σ_1} gets thus updated to $A^{\sigma_1\prime}$ and the expectation value of the energy decreases. In the second step the second tensor A^{σ_2} is updated, by optimizing over it and keeping all the other tensors fixed. This procedure is iterated over all the sites until the last one, and repeated in the opposite direction. When, after a certain number of such "sweeps", the energy has converged, the algorithm stops and the MPS approximation of the ground state is obtained.

In a more refined version of the algorithm two neighbouring tensors are optimized at each step. In particular, in the first step the tensor $C = A^{\sigma_1}A^{\sigma_2}$ is optimized. After the optimization a SVD is performed on C to get the updated tensor for the two sites, $A^{\sigma_1\prime}$ and $A^{\sigma_2\prime}$. The advantage of this two-site algorithm is that after the SVD one can keep a number of singular values which depends on some condition on their magnitude. In this way the bond dimension of the tensors can change dynamically during the algorithm, while in the one-site version it is imposed at the beginning.

BIBLIOGRAPHY

1. Boyd, R. W. *Nonlinear Optics* (Academic Press, 2003).
2. Armstrong, J. A., Bloembergen, N., Ducuing, J. & Pershan, P. S. Interactions between light waves in a nonlinear dielectric. *Phys. Rev.* **127,** 1918–1939 (1962).
3. Chang, D. E., Vuletíc, V. & Lukin, M. D. Quantum nonlinear optics - photon by photon. *Nat. Photon.* **8,** 685–694 (2014).
4. Kimble, H. J. The quantum internet. *Nature* **453,** 1023–1030 (2008).
5. De Vries, P., van Coevorden, D. V. & Lagendijk, A. Point scatterers for classical waves. *Rev. Mod. Phys.* **70,** 447–466 (1998).
6. Darquié, B. *et al.* Controlled single-photon emission from a single trapped two-level atom. *Science* **309,** 454–456 (2005).
7. Tey, M. K. *et al.* Strong interaction between light and a single trapped atom without the need for a cavity. *Nature Phys.* **4,** 924–927 (2008).
8. Hétet, G., Slodička, L., Hennrich, M. & Blatt, R. Single atom as a mirror of an optical cavity. *Phys. Rev. Lett.* **107,** 133002 (2011).
9. Wrigge, G., Gerhardt, I., Hwang, J., Zumofen, G. & Sandoghdar, V. Efficient coupling of photons to a single molecule and the observation of its resonance fluorescence. *Nature Phys.* **4,** 60–66 (2008).
10. Haroche, S. & Raimond, J.-M. *Exploring the Quantum: Atoms, Cavities, and Photons* (Oxford University Press, 2006).
11. Reiserer, A. & Rempe, G. Cavity-based quantum networks with single atoms and optical photons. *Rev. Mod. Phys.* **87,** 1379–1418 (2015).
12. Jaynes, E. T. & Cummings, F. W. Comparison of quantum and semiclassical radiation theories with application to the beam maser. *Proc. IEEE* **51,** 89–109 (1963).
13. Birnbaum, K. M., Boca, A., Miller, R., Boozer, A. D., Northup, T. E. & Kimble, H. J. Photon blockade in an optical cavity with one trapped atom. *Nature* **436,** 87–90 (2005).
14. Meystre, P. & Sargent, M. *Elements of Quantum Optics* (Springer, 2007).

15. Gardiner, C. W. & Collett, M. J. Input and output in damped quantum systems: Quantum stochastic differential equations and the master equation. *Phys. Rev. A* **31,** 3761–3774 (1985).
16. Goldstein, E. V. & Meystre, P. Dipole-dipole interaction in optical cavities. *Phys. Rev. A* **56,** 5135–5146 (1997).
17. Hammerer, K., Sørensen, A. S. & Polzik, E. S. Quantum interface between light and atomic ensembles. *Rev. Mod. Phys.* **82,** 1041–1093 (2010).
18. Arecchi, F. & Bonifacio, R. Theory of optical maser amplifiers. *IEEE J. Quant. Electron.* **1,** 169–178 (1965).
19. McCall, S. L. & Hahn, E. L. Self-induced transparency by pulsed coherent light. *Phys. Rev. Lett.* **18,** 908–911 (1967).
20. Choi, K. S., Deng, H., Laurat, J. & Kimble, H. J. Mapping photonic entanglement into and out of a quantum memory. *Nature* **452,** 67–71 (2008).
21. Fleischhauer, M. & Lukin, M. D. Dark-state polaritons in electromagnetically induced transparency. *Phys. Rev. Lett.* **84,** 5094–5097 (2000).
22. Julsgaard, B., Sherson, J., Cirac, J. I., Fiurasek, J. & Polzik, E. S. Experimental demonstration of quantum memory for light. *Nature* **432,** 482–486 (2004).
23. Liu, C., Dutton, Z., Behroozi, C. H. & Hau, L. V. Observation of coherent optical information storage in an atomic medium using halted light pulses. *Nature* **409,** 490–493 (2001).
24. Kuzmich, A., Mandel, L. & Bigelow, N. P. Generation of spin squeezing via continuous quantum nondemolition measurement. *Phys. Rev. Lett.* **85,** 1594–1597 (2000).
25. Lukin, M. D. *et al.* Dipole blockade and quantum information processing in mesoscopic atomic ensembles. *Phys. Rev. Lett.* **87,** 037901 (2001).
26. Firstenberg, O., Adams, C. S. & Hofferberth, S. Nonlinear quantum optics mediated by Rydberg interactions. *J. Phys. B* **49,** 152003 (2016).
27. Murray, C. & Pohl, T. in *Advances In Atomic, Molecular, and Optical Physics* 321–372 (Academic Press, 2016).
28. Pritchard, J. D., Weatherill, K. J. & Adams, C. S. in *Annual Review of Cold Atoms and Molecules, Volume 1.* 301–350 (World Scientific Publishing Co, 2013).
29. Fleischhauer, M., Imamoglu, A. & Marangos, J. P. Electromagnetically induced transparency: Optics in coherent media. *Rev. Mod. Phys.* **77,** 633–673 (2005).

30. Dudin, Y. O. & Kuzmich, A. Strongly interacting Rydberg excitations of a cold atomic gas. *Science* **336,** 887–889 (2012).

31. Peyronel, T. *et al.* Quantum nonlinear optics with single photons enabled by strongly interacting atoms. *Nature* **488,** 57–60 (2012).

32. Pritchard, J. D., Maxwell, D., Gauguet, A., Weatherill, K. J., Jones, M. P. A. & Adams, C. S. Cooperative atom-light interaction in a blockaded Rydberg ensemble. *Phys. Rev. Lett.* **105,** 193603 (2010).

33. Firstenberg, O., Peyronel, T., Liang, Q.-Y., Gorshkov, A. V., Lukin, M. D. & Vuletić, V. Attractive photons in a quantum nonlinear medium. *Nature* **502,** 71–75 (2013).

34. Vetsch, E., Reitz, D., Sagué, G., Schmidt, R., Dawkins, S. T. & Rauschenbeutel, A. Optical interface created by laser-cooled atoms trapped in the evanescent field surrounding an optical nanofiber. *Phys. Rev. Lett.* **104,** 203603 (2010).

35. Nayak, K. P., Melentiev, P. N., Morinaga, M., Kien, F. L., Balykin, V. I. & Hakuta, K. Optical nanofiber as an efficient tool for manipulating and probing atomic fluorescence. *Opt. Express* **15,** 5431–5438 (2007).

36. Goban, A. *et al.* Demonstration of a state-insensitive, compensated nanofiber trap. *Phys. Rev. Lett.* **109,** 033603 (2012).

37. Joannopoulos, J. D., Johnson, S. G., Winn, J. N. & Meade, R. D. *Photonic Crystals: Molding the Flow of Light* (Princeton University Press, Princeton, 2008).

38. Goban, A. *et al.* Superradiance for atoms trapped along a photonic crystal waveguide. *Phys. Rev. Lett.* **115,** 063601 (2015).

39. Jackson, J. D. *Classical Electrodynamics* (Wiley, New York, 2008).

40. John, S. & Quang, T. Spontaneous emission near the edge of a photonic band gap. *Phys. Rev. A* **50,** 1764–1769 (1994).

41. Lund-Hansen, T. *et al.* Experimental realization of highly efficient broadband coupling of single quantum dots to a photonic crystal waveguide. *Phys. Rev. Lett.* **101,** 113903 (2008).

42. Goban, A. *et al.* Atom-Light Interactions in Photonic Crystals. *Nat. Commun.* **5,** 3808 (2014).

43. Yu, S.-P. *et al.* Nanowire photonic crystal waveguides for single-atom trapping and strong light-matter interactions. *Appl. Phys. Lett.* **104,** 111103 (2014).

44. Hood, J. D. *et al.* Atom-atom interactions around the band edge of a photonic crystal waveguide. *Proc. Natl. Acad. Sci. U.S.A.* **113,** 10507–10512 (2016).

45. John, S. & Wang, J. Quantum electrodynamics near a photonic band gap: Photon bound states and dressed atoms. *Phys. Rev. Lett.* **64,** 2418–2421 (1990).

46. Douglas, J. S., Habibian, H., Hung, C.-L., Gorshkov, A. V., Kimble, H. J. & Chang, D. E. Quantum many-body models with cold atoms coupled to photonic crystals. *Nat. Photon.* **9,** 326–331 (2015).

47. Kurizki, G. Two-atom resonant radiative coupling in photonic band structures. *Phys. Rev. A* **42,** 2915–2924 (1990).

48. González-Tudela, A., Hung, C.-L., Chang, D. E., Cirac, J. I. & Kimble, H. J. Subwavelength vacuum lattices and atom-atom interactions in two-dimensional photonic crystals. *Nat. Photon.* **9,** 320–325 (2015).

49. Hauke, P. & Tagliacozzo, L. Spread of correlations in long-range interacting quantum systems. *Phys. Rev. Lett.* **111,** 207202 (2013).

50. Jurcevic, P. *et al.* Quasiparticle engineering and entanglement propagation in a quantum many-body system. *Nature* **511,** 202–205 (2014).

51. Richerme, P. *et al.* Non-local propagation of correlations in quantum systems with long-range interactions. *Nature* **511,** 198–201 (July 2014).

52. Sekoguchi, H., Takahashi, Y., Asano, T. & Noda, S. Photonic crystal nanocavity with a Q-factor of 9 million. *Opt. Express* **22,** 916–924 (2014).

53. Hartmann, M. J., Brandao, F. G.S. L. & Plenio, M. B. Strongly interacting polaritons in coupled arrays of cavities. *Nature Phys.* **2,** 849–855 (2006).

54. Greentree, A. D., Tahan, C., Cole, J. H. & Hollenberg, L. C. L. Quantum phase transitions of light. *Nature Phys.* **2,** 856–861 (2006).

55. Angelakis, D. G., Santos, M. F. & Bose, S. Photon-blockade-induced Mott transitions and XY spin models in coupled cavity arrays. *Phys. Rev. A* **76,** 031805 (2007).

56. Chang, D. E., Gritsev, V., Morigi, G., Vuletić, V., Lukin, M. D. & Demler, E. A. Crystallization of strongly interacting photons in a nonlinear optical fibre. *Nature Phys.* **4,** 884–889 (2008).

57. Otterbach, J., Moos, M., Muth, D. & Fleischhauer, M. Wigner crystallization of single photons in cold Rydberg ensembles. *Phys. Rev. Lett.* **111,** 113001 (2013).

58. Field, J. E. Vacuum-Rabi-splitting-induced transparency. *Phys. Rev. A* **47,** 5064–5067 (1993).

59. Tanji-Suzuki, H., Chen, W., Landig, R., Simon, J. & Vuletić, V. Vacuum-induced transparency. *Science* **333,** 1266–1269 (2011).

60. Gong, Z.-X., Foss-Feig, M., Michalakis, S. & Gorshkov, A. V. Persistence of locality in systems with power-law interactions. *Phys. Rev. Lett.* **113,** 030602 (2014).

61. Schachenmayer, J., Lanyon, B. P., Roos, C. F. & Daley, A. J. Entanglement growth in quench dynamics with variable range interactions. *Phys. Rev. X* **3,** 031015 (2013).

62. Chang, D. E., Cirac, J. I. & Kimble, H. J. Self-organization of atoms along a nanophotonic waveguide. *Phys. Rev. Lett.* **110,** 113606 (2013).

63. Baumann, K., Guerlin, C., Brennecke, F. & Esslinger, T. Dicke quantum phase transition with a superfluid gas in an optical cavity. *Nature* **464,** 1301–1306 (2010).

64. Klinder, J., Keßler, H., Bakhtiari, M. R., Thorwart, M. & Hemmerich, A. Observation of a superradiant Mott insulator in the Dicke-Hubbard model. *Phys. Rev. Lett.* **115,** 230403 (2015).

65. Black, A. T., Chan, H. W. & Vuletić, V. Observation of collective friction forces due to spatial self-organization of atoms: From Rayleigh to Bragg scattering. *Phys. Rev. Lett.* **91,** 203001 (2003).

66. Asbóth, J. K., Domokos, P., Ritsch, H. & Vukics, A. Self-organization of atoms in a cavity field: Threshold, bistability, and scaling laws. *Phys. Rev. A* **72,** 053417 (2005).

67. Domokos, P. & Ritsch, H. Collective cooling and self-organization of atoms in a cavity. *Phys. Rev. Lett.* **89,** 253003 (2002).

68. Peierls, R. E. *Quantum Theory of Solids* (Clarendon, 1955).

69. Pytte, E. Peierls instability in Heisenberg chains. *Phys. Rev. B* **10,** 4637–4642 (1974).

70. Cross, M. C. & Fisher, D. S. A new theory of the spin-Peierls transition with special relevance to the experiments on TTFCuBDT. *Phys. Rev. B* **19,** 402–419 (1979).

71. Bursill, R. J., McKenzie, R. H. & Hamer, C. J. Phase diagram of a Heisenberg spin-Peierls model with quantum phonons. *Phys. Rev. Lett.* **83,** 408–411 (1999).

72. Castro Neto, A. H., Guinea, F., Peres, N. M. R., Novoselov, K. S. & Geim, A. K. The electronic properties of graphene. *Rev. Mod. Phys.* **81,** 109–162 (2009).

73. Koppens, F. H. L., Chang, D. E. & García de Abajo, F. J. Graphene plasmonics: A platform for strong light-matter interactions. *Nano Lett.* **11,** 3370–3377 (2011).

74. Hwang, E. H. & Das Sarma, S. Dielectric function, screening, and plasmons in two-dimensional graphene. *Phys. Rev. B* **75,** 205418 (2007).

75. Wunsch, B., Stauber, T., Sols, F. & Guinea, F. Dynamical polarization of graphene at finite doping. *New J. Phys.* **8,** 318 (2006).

76. Chen, J. *et al.* Optical nano-imaging of gate-tunable graphene plasmons. *Nature* **487,** 77–81 (2012).

77. Fang, Z. *et al.* Gated tunability and hybridization of localized plasmons in nanostructured graphene. *ACS Nano* **7,** 2388–2395 (2013).

78. Sangouard, N., Sanguinetti, B., Curtz, N., Gisin, N., Thew, R. & Zbinden, H. Faithful entanglement swapping based on sum-frequency generation. *Phys. Rev. Lett.* **106,** 120403 (2011).

79. Fleischhauer, M. & Lukin, M. D. Quantum memory for photons: Dark-state polaritons. *Phys. Rev. A* **65,** 022314 (2002).

80. Hétet, G., Longdell, J. J., Alexander, A. L., Lam, P. K. & Sellars, M. J. Electro-optic quantum memory for light using two-level atoms. *Phys. Rev. Lett.* **100,** 023601 (2008).

81. Kozhekin, A. E., Mølmer, K. & Polzik, E. Quantum memory for light. *Phys. Rev. A* **62,** 033809 (2000).

82. Moiseev, S. A. & Kröll, S. Complete reconstruction of the quantum state of a single-photon wave packet absorbed by a Doppler-broadened transition. *Phys. Rev. Lett.* **87,** 173601 (2001).

83. Gorshkov, A. V., André, A., Fleischhauer, M., Sørensen, A. S. & Lukin, M. D. Universal approach to optimal photon storage in atomic media. *Phys. Rev. Lett.* **98,** 123601 (2007).

84. Barredo, D., de Léséleuc, S., Lienhard, V., Lahaye, T. & Browaeys, A. An atom-by-atom assembler of defect-free arbitrary two-dimensional atomic arrays. *Science* **354,** 1021–1023 (2016).

85. Endres, M. *et al.* Atom-by-atom assembly of defect-free one-dimensional cold atom arrays. *Science* **354,** 1024–1027 (2016).

86. Asenjo-Garcia, A., Moreno-Cardoner, M., Albrecht, A., Kimble, H. J. & Chang, D. E. Exponential improvement in photon storage fidelities using subradiance and "selective radiance" in atomic arrays. *preprint at arXiv:1703.03382* (2017).

87. Deutsch, I. H., Spreeuw, R. J. C., Rolston, S. L. & Phillips, W. D. Photonic band gaps in optical lattices. *Phys. Rev. A* **52,** 1394–1410 (1995).

88. Chang, D. E., Jiang, L., Gorshkov, A. V. & Kimble, H. J. Cavity QED with atomic mirrors. *New J. Phys.* **14,** 063003 (2012).

89. Shi, T. & Sun, C. P. Lehmann-Symanzik-Zimmermann reduction approach to multiphoton scattering in coupled-resonator arrays. *Phys. Rev. B* **79,** 205111 (2009).

90. Fan, S., Kocabaş, Ş. E. & Shen, J.-T. Input-output formalism for few-photon transport in one-dimensional nanophotonic waveguides coupled to a qubit. *Phys. Rev. A* **82,** 063821 (2010).

91. Zheng, H., Gauthier, D. J. & Baranger, H. U. Waveguide QED: Many-body bound-state effects in coherent and Fock-state scattering from a two-level system. *Phys. Rev. A* **82,** 063816 (2010).

92. Baragiola, B. Q., Cook, R. L., Brańczyk, A. M. & Combes, J. N-photon wave packets interacting with an arbitrary quantum system. *Phys. Rev. A* **86,** 013811 (2012).

93. Pletyukhov, M. & Gritsev, V. Quantum theory of light scattering in a one-dimensional channel: Interaction effect on photon statistics and entanglement entropy. *Phys. Rev. A* **91,** 063841 (2015).

94. Zheng, H., Gauthier, D. J. & Baranger, H. U. Cavity-free photon blockade induced by many-body bound states. *Phys. Rev. Lett.* **107,** 223601 (2011).

95. Roy, D. Two-photon scattering by a driven three-level emitter in a one-dimensional waveguide and electromagnetically induced transparency. *Phys. Rev. Lett.* **106,** 053601 (2011).

96. Shi, T., Fan, S. & Sun, C. P. Two-photon transport in a waveguide coupled to a cavity in a two-level system. *Phys. Rev. A* **84,** 063803 (2011).

97. Laakso, M. & Pletyukhov, M. Scattering of two photons from two distant qubits: Exact solution. *Phys. Rev. Lett.* **113,** 183601 (2014).

98. Redchenko, E. S. & Yudson, V. I. Decay of metastable excited states of two qubits in a waveguide. *Phys. Rev. A* **90,** 063829 (2014).

99. Pletyukhov, M. & Gritsev, V. Scattering of massless particles in one-dimensional chiral channel. *New J. Phys.* **14,** 095028 (2012).

100. Shen, J.-T. & Fan, S. Strongly correlated two-photon transport in a one-dimensional waveguide coupled to a two-level system. *Phys. Rev. Lett.* **98,** 153003 (2007).

101. Lalumière, K., Sanders, B. C., van Loo, A. F., Fedorov, A., Wallraff, A. & Blais, A. Input-output theory for waveguide QED with an ensemble of inhomogeneous atoms. *Phys. Rev. A* **88,** 043806 (2013).

102. Arcari, M. *et al.* Near-unity coupling efficiency of a quantum emitter to a photonic crystal waveguide. *Phys. Rev. Lett.* **113,** 093603 (2014).

103. Lang, C. *et al.* Observation of resonant photon blockade at microwave frequencies using correlation function measurements. *Phys. Rev. Lett.* **106,** 243601 (2011).

104. Hoi, I.-C., Wilson, C. M., Johansson, G., Palomaki, T., Peropadre, B. & Delsing, P. Demonstration of a single-photon router in the microwave regime. *Phys. Rev. Lett.* **107,** 073601 (2011).

105. Liu, Y. & Houck, A. A. Quantum electrodynamics near a photonic bandgap. *Nature Phys.* **13,** 48–52 (2017).

106. Molisch, A. F. & Oehry, B. P. *Radiation Trapping in Atomic Vapours* (Oxford Science Publications, 1999).

107. Pellegrino, J. *et al.* Observation of suppression of light scattering induced by dipole-dipole interactions in a cold-atom ensemble. *Phys. Rev. Lett.* **113,** 133602 (2014).

108. Schilder, N. J. *et al.* Polaritonic modes in a dense cloud of cold atoms. *Phys. Rev. A* **93,** 063835 (2016).

109. Guerin, W., Araújo, M. O. & Kaiser, R. Subradiance in a large cloud of cold atoms. *Phys. Rev. Lett.* **116,** 083601 (2016).

110. Moos, M., Höning, M., Unanyan, R. & Fleischhauer, M. Many-body physics of Rydberg dark-state polaritons in the strongly interacting regime. *Phys. Rev. A* **92,** 053846 (2015).

111. Bienias, P. *et al.* Scattering resonances and bound states for strongly interacting Rydberg polaritons. *Phys. Rev. A* **90,** 053804 (2014).

112. Maghrebi, M. F. *et al.* Coulomb bound states of strongly interacting photons. *Phys. Rev. Lett.* **115,** 123601 (2015).

113. Gullans, M. J. *et al.* Effective field theory for Rydberg polaritons. *Phys. Rev. Lett.* **117,** 113601 (2016).

114. Zeuthen, E., Gullans, M. J., Maghrebi, M. F. & Gorshkov, A. V. Correlated photon dynamics in dissipative Rydberg media. *preprint at arXiv:1608.06068* (2016).

115. Roy, D., Wilson, C. M. & Firstenberg, O. Colloquium. *Rev. Mod. Phys.* **89,** 021001 (2017).

116. Gorshkov, A. V., André, A., Lukin, M. D. & Sørensen, A. S. Photon storage in Λ-type optically dense atomic media. II. Free-space model. *Phys. Rev. A* **76,** 033805 (2007).

117. Zeuthen, E., Grodecka-Grad, A. & Sørensen, A. S. Three-dimensional theory of quantum memories based on Λ-type atomic ensembles. *Phys. Rev. A* **84,** 043838 (2011).

118. Sørensen, M. W. & Sørensen, A. S. Three-dimensional theory for light-matter interaction. *Phys. Rev. A* **77,** 013826 (2008).

119. Chang, D. E., Sörensen, A. S., Demler, E. A. & Lukin, M. D. A single-photon transistor using nanoscale surface plasmons. *Nature Phys.* **3,** 807–812 (2007).

120. Shen, J. T. & Fan, S. Coherent photon transport from spontaneous emission in one-dimensional waveguides. *Opt. Lett.* **30,** 2001–2003 (2005).

121. Corzo, N. V. *et al.* Large Bragg reflection from one-dimensional chains of trapped atoms near a nanoscale waveguide. *Phys. Rev. Lett.* **117,** 133603 (2016).

122. Sørensen, H. L. *et al.* Coherent backscattering of light off one-dimensional atomic strings. *Phys. Rev. Lett.* **117,** 133604 (2016).

123. Birkl, G., Gatzke, M., Deutsch, I. H., Rolston, S. L. & Phillips, W. D. Bragg scattering from atoms in optical lattices. *Phys. Rev. Lett.* **75,** 2823–2826 (1995).

124. Bajcsy, M., Zibrov, A. S. & Lukin, M. D. Stationary pulses of light in an atomic medium. *Nature* **426,** 638–641 (2003).

125. Douglas, J. S., Caneva, T. & Chang, D. E. Photon molecules in atomic gases trapped near photonic crystal waveguides. *Phys. Rev. X* **6,** 031017 (2016).

126. Xu, S. & Fan, S. Input-output formalism for few-photon transport: A systematic treatment beyond two photons. *Phys. Rev. A* **91,** 043845 (2015).

127. Baur, S., Tiarks, D., Rempe, G. & Dürr, S. Single-photon switch based on Rydberg blockade. *Phys. Rev. Lett.* **112,** 073901 (2014).

128. Gorshkov, A. V., Otterbach, J., Fleischhauer, M., Pohl, T. & Lukin, M. D. Photon-photon interactions via Rydberg blockade. *Phys. Rev. Lett.* **107,** 133602 (2011).

129. Mollow, B. R. Pure-state analysis of resonant light scattering: Radiative damping, saturation, and multiphoton effects. *Phys. Rev. A* **12,** 1919–1943 (Nov. 1975).

130. Verstraete, F., Murg, V. & Cirac, J. Matrix product states, projected entangled pair states, and variational renormalization group methods for quantum spin systems. *Adv. Phys.* **57,** 143–224 (2008).

131. Schollwöck, U. The density-matrix renormalization group in the age of matrix product states. *Ann. Phys.* **326,** 96–192 (2011).

132. Verstraete, F. & Cirac, J. I. Matrix product states represent ground states faithfully. *Phys. Rev. B* **73,** 094423 (2006).

133. Mølmer, K., Castin, Y. & Dalibard, J. Monte Carlo wavefunction method in quantum optics. *J. Opt. Soc. Am. B* **10,** 524–538 (1993).

134. Daley, A. J., Taylor, J. M., Diehl, S., Baranov, M. & Zoller, P. Atomic three-body loss as a dynamical three-body interaction. *Phys. Rev. Lett.* **102,** 040402 (2009).

135. Daley, A. J. Quantum trajectories and open many-body quantum systems. *Adv. Phys.* **63,** 77–149 (2014).

136. Zwolak, M. & Vidal, G. Mixed-state dynamics in one-dimensional quantum lattice systems: A time-dependent superoperator renormalization algorithm. *Phys. Rev. Lett.* **93,** 207205 (2004).

137. Verstraete, F., García-Ripoll, J. J. & Cirac, J. I. Matrix product density operators: Simulation of finite-temperature and dissipative systems. *Phys. Rev. Lett.* **93,** 207204 (2004).

138. Cui, J., Cirac, J. I. & Bañuls, M. C. Variational matrix product operators for the steady state of dissipative quantum systems. *Phys. Rev. Lett.* **114,** 220601 (2015).

139. Mascarenhas, E., Flayac, H. & Savona, V. Matrix-product-operator approach to the nonequilibrium steady state of driven-dissipative quantum arrays. *Phys. Rev. A* **92,** 022116 (2015).

140. Rice, P. & Brecha, R. Cavity induced transparency. *Opt. Commun.* **126,** 230 –235 (1996).

141. Nikoghosyan, G. & Fleischhauer, M. Photon-number selective group delay in cavity induced transparency. *Phys. Rev. Lett.* **105,** 013601 (2010).

142. Lauk, N. & Fleischhauer, M. Number-state filter for pulses of light. *Phys. Rev. A* **93,** 063818 (2016).

143. Shahmoon, E., Grišins, P., Stimming, H. P., Mazets, I. & Kurizki, G. Highly nonlocal optical nonlinearities in atoms trapped near a waveguide. *Optica* **3,** 725–733 (2016).

144. Maghrebi, M. F., Yao, N. Y., Hafezi, M., Pohl, T., Firstenberg, O. & Gorshkov, A. V. Fractional quantum Hall states of Rydberg polaritons. *Phys. Rev. A* **91,** 033838 (2015).

145. Ni, K.-K. *et al.* A high phase-space-density gas of polar molecules. *Science* **322,** 231–235 (2008).

146. Jin, D. & Ye, J. in *Many-Body Physics with Ultracold Gases: Lecture Notes of the Les Houches Summer School* (2010).

147. Micheli, A., Brennen, G. K. & Zoller, P. A toolbox for lattice-spin models with polar molecules. *Nature Phys.* **2,** 341–347 (May 2006).

148. Saffman, M., Walker, T. G. & Mølmer, K. Quantum information with Rydberg atoms. *Rev. Mod. Phys.* **82,** 2313–2363 (2010).

149. Porras, D. & Cirac, J. I. Effective quantum spin systems with trapped ions. *Phys. Rev. Lett.* **92,** 207901 (2004).

150. Norcia, M. A., Winchester, M. N., Cline, J. R. K. & Thompson, J. K. Superradiance on the millihertz linewidth strontium clock transition. *Sci. Adv.* **2** (2016).

151. Buhmann, S. Y. & Welsch, D.-G. Dispersion forces in macroscopic quantum electrodynamics. *Progr. in Quant. Electron.* **31,** 51 –130 (2007).

152. Dung, H. T., Knöll, L. & Welsch, D.-G. Resonant dipole-dipole interaction in the presence of dispersing and absorbing surroundings. *Phys. Rev. A* **66,** 063810 (2002).

153. Asenjo-Garcia, A., Hood, J. D., Chang, D. E. & Kimble, H. J. Atom-light interactions in quasi-one-dimensional nanostructures: A Green's-function perspective. *Phys. Rev. A* **95,** 033818 (2017).

154. Tiecke, T. G., Thompson, J. D., de Leon, N. P., Liu, L. R., Vuletic, V. & Lukin, M. D. Nanophotonic quantum phase switch with a single atom. *Nature* **508,** 241–244 (2014).

155. Lieb, E., Schultz, T. & Mattis, D. Two soluble models of an antiferromagnetic chain. *Ann. Phys.* **16,** 407–466 (1961).

156. Jordan, P. & Wigner, E. Über das Paulische Äquivalenzverbot. *Zeitschrift für Physik* **47,** 631–651 (1928).

157. Bravyi, S., DiVincenzo, D. P. & Loss, D. Schrieffer-Wolff transformation for quantum many-body systems. *Ann. Phys.* **326,** 2793 –2826 (2011).

158. Giamarchi, T. *Quantum Physics in One Dimension* (Clarendon Press, 2004).

159. Oshikawa, M., Yamanaka, M. & Affleck, I. Magnetization plateaus in spin chains: "Haldane gap" for half-integer spins. *Phys. Rev. Lett.* **78,** 1984–1987 (1997).

160. Kaufman, A. M. *et al.* Two-particle quantum interference in tunnel-coupled optical tweezers. *Science* **345,** 306–309 (2014).

161. Okunishi, K. & Tonegawa, T. Fractional S^z excitation and its bound state around the 1/3 plateau of the $S = 1/2$ Ising-like zigzag XXZ chain. *Phys. Rev. B* **68,** 224422 (2003).

162. Jablan, M., Buljan, H. & Soljačić, M. Plasmonics in graphene at infrared frequencies. *Phys. Rev. B* **80,** 245435 (2009).

163. Fei, Z. *et al.* Gate-tuning of graphene plasmons revealed by infrared nano-imaging. *Nature* **487,** 82–85 (2012).

164. Brar, V. W., Jang, M. S., Sherrott, M., Lopez, J. J. & Atwater, H. A. Highly confined tunable mid-infrared plasmonics in graphene nanoresonators. *Nano Lett.* **13,** 2541–2547 (2013).

165. Mikhailov, S. A. & Ziegler, K. Nonlinear electromagnetic response of graphene: frequency multiplication and the self-consistent-field effects. *J. Phys. Condens. Matter* **20,** 384204 (2008).

166. Hendry, E., Hale, P. J., Moger, J., Savchenko, A. K. & Mikhailov, S. A. Coherent nonlinear optical response of graphene. *Phys. Rev. Lett.* **105,** 097401 (2010).

167. Mikhailov, S. A. Theory of the giant plasmon-enhanced second-harmonic generation in graphene and semiconductor two-dimensional electron systems. *Phys. Rev. B* **84,** 045432 (2011).

168. Constant, T. J., Hornett, S. M., Chang, D. E. & Hendry, E. All-optical generation of surface plasmons in graphene. *Nature Phys.* **12,** 124–127 (2016).

169. Gullans, M., Chang, D. E., Koppens, F. H. L., de Abajo, F. J. G. & Lukin, M. D. Single-photon nonlinear optics with graphene plasmons. *Phys. Rev. Lett.* **111,** 247401 (2013).

170. Ashcroft, N. W. & Mermin, N. D. *Solid State Physics* (New York: Harcourt College Publishers, 1976).

171. Mikhailov, S. A. Non-linear electromagnetic response of graphene. *EPL* **79,** 27002 (2007).

172. Savoia, A., Siano, M., Paparo, D. & Marrucci, L. Nonlocal optical second harmonic generation from centrosymmetric birefringent crystals: the case of muscovite mica. *J. Opt. Soc. Am. B* **28,** 679–688 (2011).

173. Heinz, T. F. Second-order nonlinear optical effects at surfaces and interfaces. *Modern Problems in Condensed Matter Sciences* (1991).

174. Majumdar, A. & Gerace, D. Single-photon blockade in doubly resonant nanocavities with second-order nonlinearity. *Phys. Rev. B* **87,** 235319 (2013).

175. Irvine, W. T. M., Hennessy, K. & Bouwmeester, D. Strong coupling between single photons in semiconductor microcavities. *Phys. Rev. Lett.* **96,** 057405 (2006).

176. Rodriguez, A., Soljačić, M., Joannopoulos, J. D. & Johnson, S. G. $\chi(2)$ and $\chi(3)$ harmonic generation at a critical power in inhomogeneous doubly resonant cavities. *Opt. Express* **15,** 7303–7318 (2007).

177. Thongrattanasiri, S., Manjavacas, A. & García de Abajo, F. J. Quantum finite-size effects in graphene plasmons. *ACS Nano* **6,** 1766–1775 (2012).

178. García de Abajo, F. J. Graphene plasmonics: challenges and opportunities. *ACS Photonics* **1,** 135–152 (2014).

179. Novoselov, K. S. *et al.* Electric field effect in atomically thin carbon films. *Science* **306,** 666–669 (2004).

180. Yan, H. *et al.* Damping pathways of mid-infrared plasmons in graphene nanostructures. *Nat. Photon.* **7,** 394–399 (2013).

181. Guerreiro, T. *et al.* Nonlinear interaction between single photons. *Phys. Rev. Lett.* **113,** 173601 (2014).

182. Thongrattanasiri, S., Koppens, F. H. L. & García de Abajo, F. J. Complete optical absorption in periodically patterned graphene. *Phys. Rev. Lett.* **108,** 047401 (2012).

183. Manzoni, M. T., Silveiro, I., García de Abajo, F. J. & Chang, D. E. Second-order quantum nonlinear optical processes in single graphene nanostructures and arrays. *New J. Phys.* **17,** 083031 (2015).

184. Cox, J. D. & Javier García de Abajo, F. Electrically tunable nonlinear plasmonics in graphene nanoislands. *Nat. Commun.* **5,** 5725 (Dec. 2014).

185. Cox, J. D. & García de Abajo, F. J. Plasmon-enhanced nonlinear wave mixing in manostructured graphene. *ACS Photonics* **2,** 306–312 (2015).

186. Briegel, H.-J., Dür, W., Cirac, J. I. & Zoller, P. Quantum repeaters: The role of imperfect local operations in qantum communication. *Phys. Rev. Lett.* **81,** 5932–5935 (1998).

187. Duan, L.-M., Lukin, M. D., Cirac, J. I. & Zoller, P. Long-distance quantum communication with atomic ensembles and linear optics. *Nature* **414,** 413–418 (Nov. 2001).

188. Chen, Y.-A. *et al.* Memory-built-in quantum teleportation with photonic and atomic qubits. *Nature Phys.* **4,** 103–107 (Feb. 2008).

189. Chen, W. *et al.* All-optical switch and transistor gated by one stored photon. *Science* **341,** 768–770 (2013).

190. Shahmoon, E., Wild, D. S., Lukin, M. D. & Yelin, S. F. Cooperative resonances in light scattering from two-dimensional atomic arrays. *Phys. Rev. Lett.* **118,** 113601 (2017).

191. Chen, C. G., Konkola, P. T., Ferrera, J., Heilmann, R. K. & Schattenburg, M. L. Analyses of vector Gaussian beam propagation and the validity of paraxial and spherical approximations. *J. Opt. Soc. Am. A* **19,** 404–412 (2002).

192. Novotny, L. & Hecht, B. *Principles of Nano-Optics* (Cambridge University Press, 2006).

193. White, S. R. Density matrix formulation for quantum renormalization groups. *Phys. Rev. Lett.* **69,** 2863–2866 (1992).

194. Schollwöck, U. The density-matrix renormalization group. *Rev. Mod. Phys.* **77,** 259–315 (2005).